**FOREIGN
BROADCAST
INFORMATION
SERVICE**

JPRS Report

Science &
Technology

Japan

19980701 052

DTIC QUALITY INSPECTED 1

SCIENCE & TECHNOLOGY

JAPAN

CONTENTS

ADVANCED MATERIALS

SUPERCONDUCTIVITY

New Developments in Applied Superconductivity

Current Status, Outlook for Colloidal (Sol-Gel) Process

43067032 Tokyo THE 20TH INTELLIGENT PROCESSING in Japanese 22 Sep 88
pp 16-25

[Article by Yoshitaka Nomiya, Colloid Research, Ltd.]

[Text] **1. Introduction**

Particles of 10~1,000 Å suspended in liquid or gas, or that state of particle suspension, are called colloid (Table 1). Among the chemical methods for manufacturing glasses and ceramics from a solution, the method that uses the colloidal state uses changes in the sol-gel state and is widely called the sol-gel method. Here we shall focus on the process that can highly enhance the characteristics of ceramics by controlling colloidal particles at the molecular level, and the process is called the colloidal process.

Table 1. Definition of Colloid

Colloid →	Shape:	Particulate, layer, and threadlike
	Number of atoms:	$10^3 \sim 10^9$
	Diameter:	10 ~ 1,000 Å (10,000 Å)
Sol	→	A solution with colloidal particle suspension
Gel	→	A sol that lost fluidity

Table 2. International Meetings on Colloidal Process

International Workshop on Glasses and Glass Ceramics from Gels
            Held in 1981, 1983, 1985, and 1987

International Conference on Ultrastructure Processing of Ceramics, Glasses, and Composites
            Held in 1983, 1985, and 1987

Materials Research Society Symposium on Better Ceramics Through Chemistry
            Held in 1984, 1986, and 1988   .

The colloidal process has a long history, but the event that drew wide attention to the process was the report of Dislich of the Schott Co. of West Germany in 1971 on the low temperature synthesis of multicomponent glasses by hydrolysis of metal alkoxide. Since 1981, several international meetings have been held focusing on this process (Table 2).

Here, I would like to introduce the present status and describe the future tasks and outlook of the colloidal process that applies the hydrolysis of metallic alkoxide which is now drawing attention as a method to make new glasses and fine ceramics.

2. Outline of Colloidal Process

2.1 Raw Materials

Raw materials are inorganic metal salts formed by replacement of active hydrogen of organic solvents such as inorganic acids, organic acids, and alcohols, with metals, and organic metal salts (Table 3).

Table 3. Raw Materials

M: Metal n: Valence	R: Alkyl group
(Inorganic Metal Salts)	
Nitrates	$M(NO_3)_n$
Chlorides	MCl_n
Oxychlorides	$MOCl_{n-2}$
(Organic Metal Salts)	
Alkoxides	$M(OR)_n$
Acetylacetonate	$M(C_5H_7O_2)_n$
Acetates	$M(C_2H_3O_2)_n$
Oxalates	$M(C_2O_4)_{n/2}$

2.2 Hydrolysis and Gel Formation

Among the metal salts listed above, metal alkoxide is particularly widely used for the reasons that it exists mostly with metal, is highly purified, and hydrolyzes readily to form hydroxides, and further, depending on conditions, it forms oxides or oxide-containing gel by dehydration and polycondensation (Figure 1).

$$M(OR)_n + n\ H_2O \rightarrow \underline{M(OH)_n} + n\ ROH$$
$$\longrightarrow (MO_{n/2})_x + X \cdot \sim n\ H_2O$$
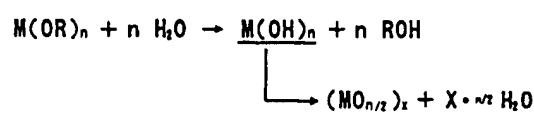
Figure 1. Hydrolysis of Metal Alkoxides

Since metal alkoxide is immiscible with water directly, alcohol solvents such as ethanol are used. Also, to control hydrolysis, an acid such as hydrochloric acid and an alkali such as ammonia are added as a catalyst.

Et : Ethyl group
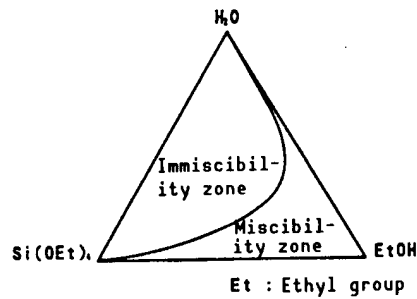
Figure 2. Miscibility Diagram of $Si(OEt)_4$-EtOH-H_2O System

In Figure 3, the process of making a bulk form (lump) is shown. A porous dry gel is formed when liquid such as water and alcohol contained in the gel is removed by drying. Fine glass or ceramics are then formed from this by calcination.
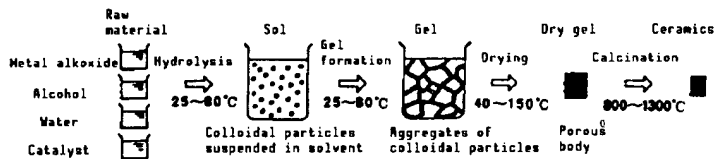
Figure 3. Making of Ceramics in Bulk Form by Colloidal Process

2.3 Kinds of Colloidal Processes

When colloidal processes are classified according to the changed states of solution after hydrolysis of a metallic salt, they are roughly classified into the powder precipitation method that precipitates colloidal particles, the sol-gel powder method, and the sol-gel direct formation method. The latter two uses gel formation (Figure 4).
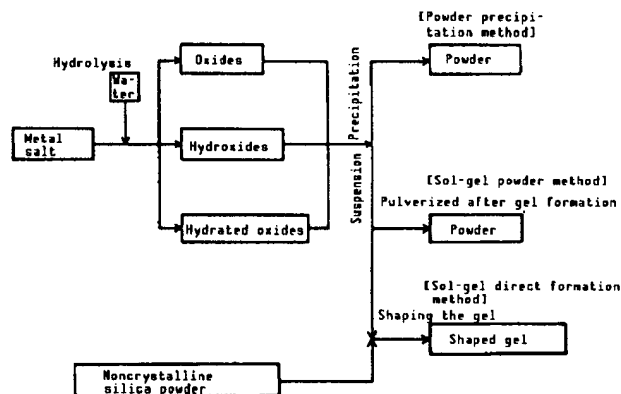
Figure 4. Kinds of Colloidal Processes

3

2.4 Characteristics of Colloidal Process and Technological Meaning

The advantages of using metal alkoxide are shown in Table 4. Furthermore, from the standpoint of manufacturing process, the following advantages can be listed.

Table 4. Advantages in Using Metal Alkoxides

(Alkoxide)
   • High purification by distillation/
       recrystallization
(Hydrolysis)
   • Produce no anions (Cl, S)
   • Produce no alkaline cations (Na, K)
   • Low temperature reaction (about 80°C)
	→ High purity

(Alkoxide)
   • Reaction control possible by selecting
       alkyl group
(Alteration)
   • Reaction control possible by functional
       group
	→ Uniform quality
	   composition

(1) Low temperature synthesis is possible

For example, a temperature of more than 2,000°C is required for the formation of silica glass by the melting method, whereas with the present method, it is possible to use a temperature in the vicinity of 1,200°C.

(2) It is possible to make glass and ceramics with a new composition

For example, when making $SrO-SiO_2$ with the melting method, there are some composition areas that could not be made because of the immiscibility of the materials in melted form.[1]

(3) Can be shaped into a form at will

On the other hand, the following problems exist:

    1) High cost of raw materials
    2) Contraction during the processes of drying and calcination
    3) Residues of carbon, OH group, and fine pores

2.5 Patent Trends

About 800 patents published from 1971 to 1986 were surveyed for ceramics synthesis by colloidal processes.

The number of patent applications has increased since about 1980 (Figure 5). When classified by elements, more than 40 percent were SiO_2 system, and

others were Al$_3$O$_3$, TiO$_2$, and ZrO$_2$ (Figure 6). Classified by form, there are mainly bulk form, powder, and thin film coating (Figure 7). When classified by usage, SiO$_2$ system is mainly used as optic bulk glass materials such as optical fiber main material and photomask, and those ceramics other than SiO$_2$ are used mostly as powder, functional thin membranes, and catalyst carriers.
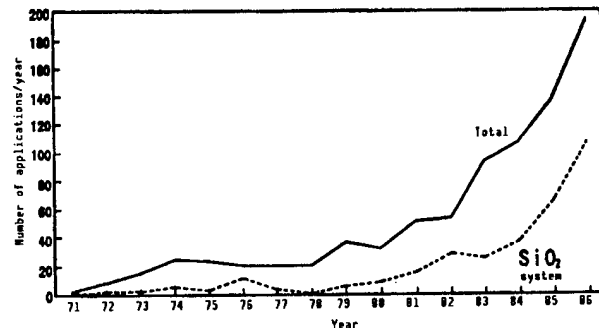
Figure 5. Trend in Numbers of Patent Applications
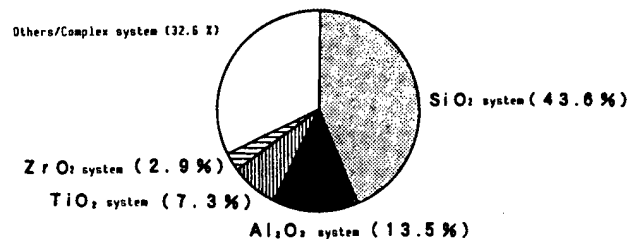
Figure 6. Patent Applications Classified by Element
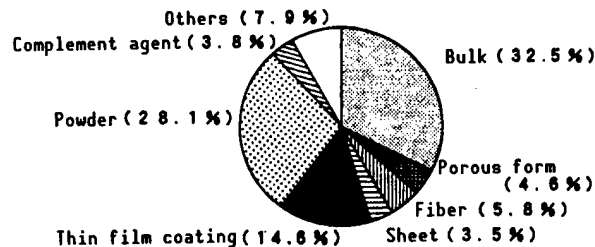
Figure 7. Patent Applications Classified by Form
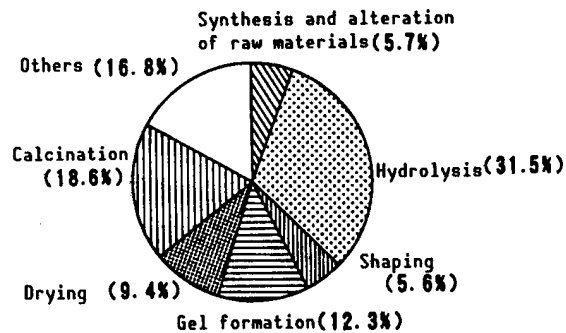
Figure 8. Patent Applications Classified by Fabrication Process

5

When classified by manufacturing process, the most numerous are hydrolysis related, followed by calcination, gel formation, and drying (Figure 8).

3. Synthesis and Properties of Metal Alkoxides[2]

There are many kinds of metal alkoxides depending on the kind of alkyl group, R, they carry, but because of the boiling point of the solvent alcohol, only those up to butoxide are usually used (Table 5). Most metal elements form alkoxides (Figure 9).

Table 5. Metal Alkoxides

$M(OCH_3)_n$	Methoxide	$M(OMe)_n$
$M(OC_2H_5)_n$	Ethoxide	$M(OEt)_n$
$M(OC_3H_7^x)_n$	Propoxide	$M(OPr^x)_n$
	x = n (normal), i (iso)	
$M(OC_4H_9^x)_n$	Butoxide	$M(OBu^x)_n$
x = n (normal), i (iso), s (secondary), t (tertiary)		

Figure 9. Elements That Form Metal Alkoxides[2]

Synthesis is related to the degree of negative electric charges of metal elements, and electrically positive elements react directly with alcohol; others utilize chlorides (Table 6).

Table 6. Synthesis Methods of Alkoxides

(Metal direct reaction method) Li, Na, K, Mg, Ca, Sr, Ba, Al
$$M + n\ ROH \rightarrow M(OR)_n + n/2\ H_2 \uparrow$$
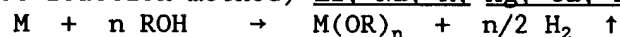
(Chloride)
Reaction with alcohol: B, Si, Ge, Sn, P, As, Se, Te, Ti, Zr, Nb, Ta, Sb, W
$$MCl + n\ ROH \rightarrow M(OR)_n + n\ HCl \uparrow$$
Reaction with sodium alkoxide: V, Mn, Cr, Fe, Co, Ni, Ga, In, V, La, Nd, Bi
$$MCl + n\ NaOR \rightarrow M(OR)_n + nNaCl \downarrow$$
Reaction with lithium alkoxide
$$MCl + n\ LiOR \rightarrow M(OR)_n \downarrow + n\ LiCl$$
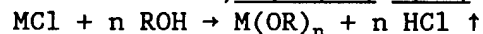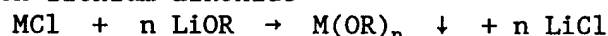
General properties or physicochemical properties of metal alkoxides (Table 7) are greatly affected by their molecular association (Figure 10).

6

Table 7. Properties of Metal Alkoxide

(Solid form) Generally volatile, and low solubility in organic solvent
  Alkali metals and alkali earth metals
  Y and lanthandie metals
  Bivalent Cr, Mn, Co, Ni, Cu,
  Zn, In, and W

(In both solid and liquid form)
  Ti, Nb, Ta, Sb------Only methoxide is solid
  Zr, Hf, Ga, Sn------Solid up to ethoxide
  Fe, Al, Pb----------Solid up to propoxide

(Liquid form) Volatile and highly soluble in organic solvent
  Nonmetal and semimetal (B, Si, Ge, P, As, Se, Te)
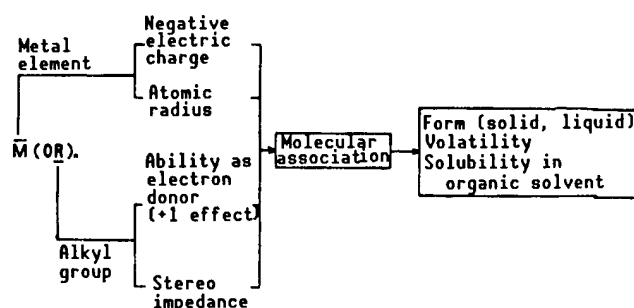
Figure 10. Factors Affecting Forms and Properties of Metal

4. Main Technology of Colloidal Process

4.1 Control of Starting Raw Material in Multicomponent System

In the case of a multicomponent system, if hydrolysis is carried out simply by mixing alkoxides with different metal elements, it is difficult to obtain a sol with uniform composition because of differences in the rate of hydrolysis. Therefore, the following operation is carried out.

(1) Partial hydrolysis[3]

First, partially hydrolyze the slower reacting alkoxide, usually Si-alkoxide (Si-OR), with a little less water than is required for complete hydrolysis, then mix with faster acting alkoxide (M-OR), M-OR is hydrolyzed by Si-OH to form the Si-O-M bond.

(2) Choice of alkyl group

The higher the number of carbons in an alkyl group, the slower the rate of hydrolysis.

(3) Double alkoxide formation

If a double alkoxide such as $Mg[Al(OC_2H_5)_4]_2$ is used, it is possible to form a completely homogeneous stoichiometrical composition.

(4) Stable alteration[2]

The organic compounds listed in Table 8 can suppress hydrolysis by reacting their active hydrogen with the alkoxyl group of alkoxide and replacing it.

Table 8.   Stabilization of Alkoxide Alteration

	<Example>
Glycol:	ethyleneglycol
Carbonic acid:	acetic acid
β-diketone:	acetylacetone
Alcanolamine:	ethanolamine

(5) Hydrolysis by the crystalline water of a hydrated inorganic salt

Figure 11 shows various cordierite synthesis methods as applied examples of the above methods. Method A mixes compounds after complete hydrolysis of each alkoxide individually; method B uses crystalline water for hydrolysis; and method C partially hydrolyzes silicone alkoxide. With the C-1 method or the C-2 method shown in Table 9, the formation of an Si-O-Al bond is expected, and therefore, cordierite is formed at the lowest temperature.[4]

EG : Ethylene glycol
EE : 2-ethoxyethahol
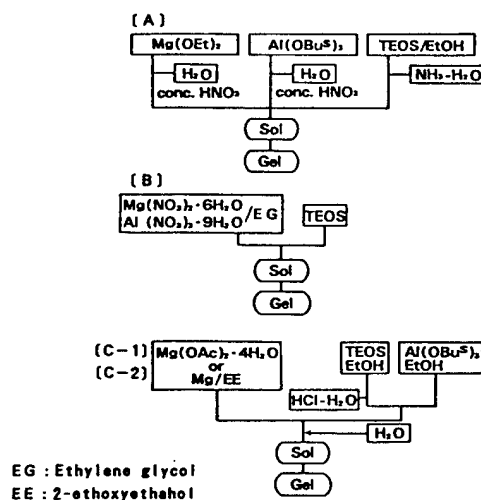
Figure 11.   Cordierite Synthesis Method

8

Table 9. Results of X-Ray Diffraction After 1 Hour Prepyrolysis

Calcination temp. (°C)	A	B	C – 1	C – 2
900	amorphous	amorphous	amorphous	amorphous
1000	amorphous (S, F)	μ	μ	μ
1100	amorphous (S, F)	α, μ	α	α
1200	SAP, Q (S, F) unknown	α	α	α
1300	α, (F, SAP)			
1400	α	α	α	α

S; spinel   Q; β-quartz
F; forsterite   SAP; sapphirine

Also, when introducing byproducts, sometimes chlorides, nitrates, acetates, and acetylacetonates are used because sometimes alkoxides are insoluble in organic solvents or the cost is high in actual application.

4.2 Hydrolysis and Control of Polycondensation

When the alkoxides of Si, Ti, Al, and Zr are hydrolyzed, polycondensation occurs to form a gel.

Especially in the case of Si, because of slow hydrolysis rate, the gel structure can be controlled easily with the changing of the form of the polycondensation product by manipulating the ratio of OH group to OR group in the product during the reaction process depending on the conditions for hydrolysis (Figures 12 and 13).
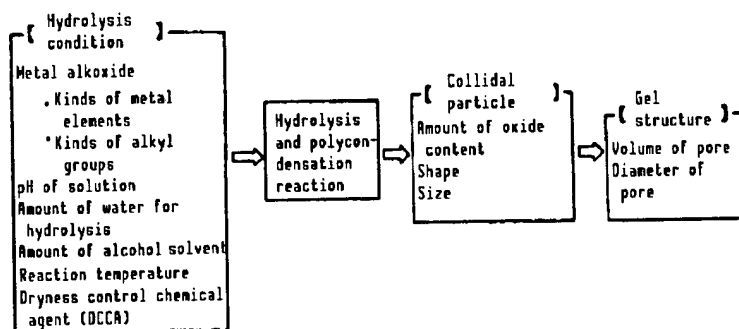
Figure 12. Hydrolysis and Control of Polycondensation

When pH and water are low, partial hydrolysis occurs, and the product polycondenses to form a linear chain-like polymer (Figure 14(a). As a result, the gel pores become few and small. On the other hand, when pH is high and the amount of water is at the standard or a high level, complete hydrolysis occurs, and the product polycondenses to form three-dimensional tightly bound polymers or particles (Figure 14(b),(c)). As a result, the gel pores are numerous with large diameters.

9
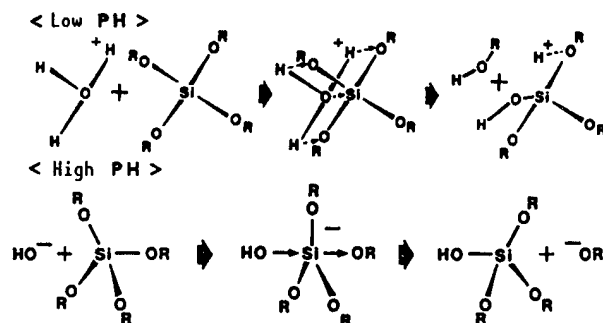
Figure 13. Effect of pH on Hydrolysis Reaction
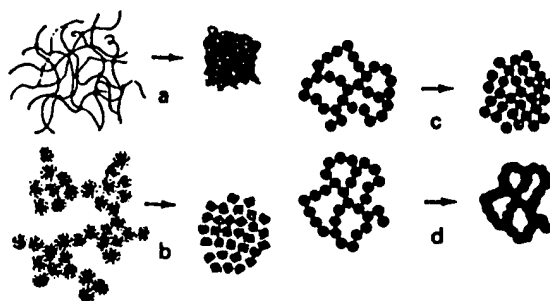
Figure 14. Structure of Gel Before and After Drying
            (a) Low pH and low amount of water
            (b) High pH and standard amount of water
            (c) High pH and high amount of water
            (d) Aging

Since the binding of small polymers continues after the formation of gel, the gel structure changes. It is called aging. It is particularly clear at high pH, and as the neck between particles grows, the pore diameter increases (Figure 14(d)).

A dryness control chemical agent (DCCA) such as formamide[7] contributes to the acceleration of aging.
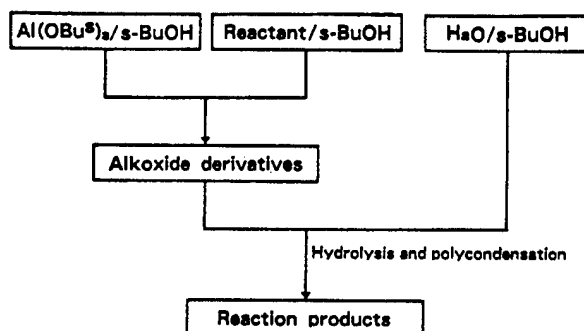
Figure 15. Examination of Effect of Stable Alteration Agent
            in Manufacture of Aluminum Fiber

Table 10. Effect of Stable Alteration Agent

	Alkoxide derivative	Hydrolysis product
—	—	precipitate
CH₃-C(=O)-CH₂-C(=O)-CH₃	clear soln.	precipitate
CH₃-C(=O)-CH₂-C(=O)-O-C₂H₅	clear soln.	(clear soln.)
NH₂CH₂CH₂OH	clear soln.	precipitate
NH(CH₂CH₂OH)₂	clear soln.	precipitate
N(CH₂CH₂OH)₃	clear soln.	(clear soln.)

We describe below examples of the application of stable alteration and control of hydrolysis in the manufacture of aluminum fiber.[8] To make fiber with aluminum alkoxide, stable alteration must be carried out because of rapid hydrolysis. Thus, the effect of stable alteration agents belonging to the β-diketone system and to the alcanolamine system was checked using the method shown in Figure 15. To obtain linear chain polymer, the mol number of stable alteration agent (calculated by the amount of active hydrogen), and hydrolysis water were each equal to the mol number of aluminum alkoxide. As shown in Table 10, there is no precipitation after hydrolysis and a transparent sol developed in the case of ethylacetoacetate and triethanolamine. These sols increased their viscosity with the removal of the solvent by distillation (Figure 16). Furthermore, these sols showed no dependency on the shearing rate of the viscosity (Figure 17), were Newtonian,[9] showing thread tracing, and were able to weave thread.
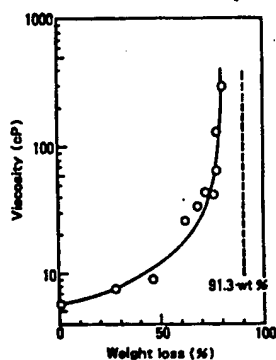
Figure 16. Relationship Between Sol Weight Loss and Viscosity
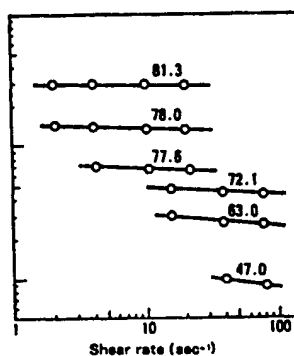
Figure 17. Relationship Between Sol and Shear Rate

11

4.3 Dryness Control

When drying, there is a capillary pressure $P = 2\gamma \cos\theta/r$ working at the meniscus in the pore (Figure 18), and when this force is greater than the strength of gel, a crack is formed. Here, γ is the surface tension, θ is the wet angle, and r is the pore radius.[10] Accordingly, the pore diameter must be large to prevent the formation of cracks. In practice, the pore is enlarged by hydrolysis and aging at high pH and by the addition of a DCCA; at the same time, the gel structure is strengthened. Also, shrinking of gel occurs due to capillary force during drying.
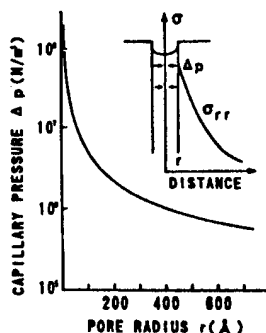
Figure 18. Capillary Force and Distribution of Stress Near the Capillary Wall

The method that eliminates meniscus by supercritical drying to prevent the occurrence of surface tension is also used. Supercritical drying is a method which immerses the gel in an alcohol solvent in a pressurized container and then removes the solvent in the gel using one of the following methods.

(1) Autoclave supercritical drying (Figure 19)

After surpassing critical temperature and critical pressure to reach the supercritical state, the pressure is reduced without going through the liquid phase.
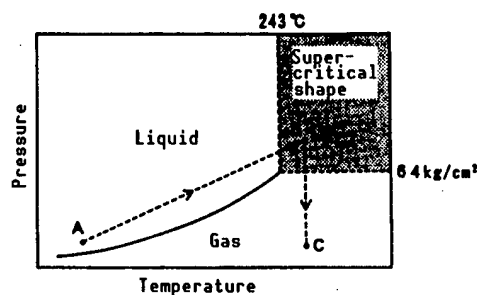
Figure 19. Ethanol Phases

(2) CO_2 extraction supercritical drying (Figures 20, 21)

As carbon dioxide gas is circulated, dilution is carried out at the supercritical state that is beyond the critical temperature and critical pressure of the alcohol-carbon dioxide mixture.
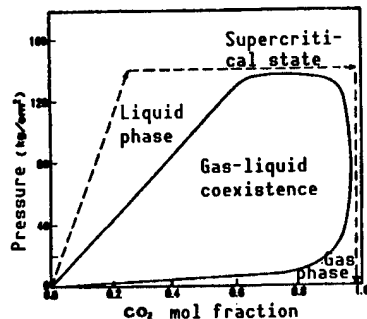
Figure 20. CO_2-Ethanol Gas Equilibrium State
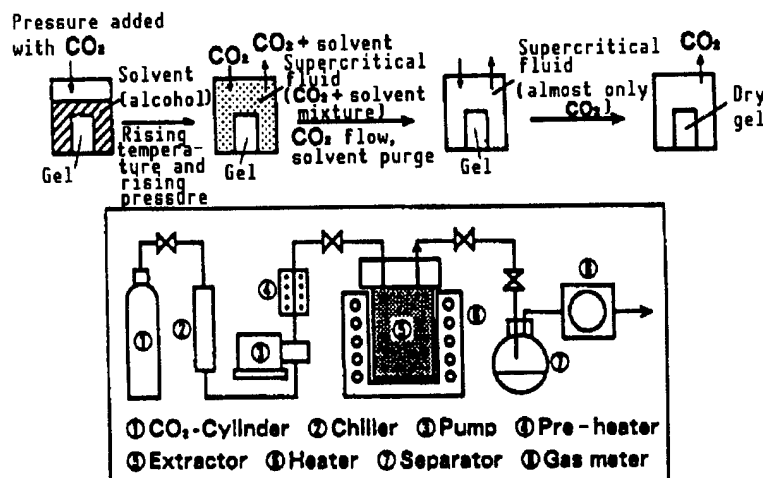
Figure 21. CO_2 Extraction Method

In supercritical drying, there is no shrinking of the gel; therefore, compared to naturally dried gel (called xycello gel), a gel with large ore diameter and low volume density (called aerogel) can be obtained.

As an example of the application of supercritical drying, the examination process for the manufacture of large silica aerogel is shown below.[11] Using the composition shown in Table 11, experiments were carried out according to Figure 22. Water, equal in mol to the OR group of each alkoxide of water, was used. The result of drying at normal pressure is shown in Figure 23: Et/o-2.is the strongest, and Me/o-1 is the weakest. Next, at the composition of Et/o-2, Me/m-1, and Me/0-1, supercritical drying was carried out using the autoclave method and the CO_2 method. The Me/o-1 product supercritically dried with the autoclave method showed crack, but others showed no crack. As seen in Figure 24 and Table 12, there are larger pore

Table 11. Composition Examined

Catalyst	Silicone alkoxide	Ethoxide (TEOS)		Methoxide (TMOS)	
		Monomer	Oligomer	Monomer	Oligomer
Ammonia		--	Et/o-1	Me/m-1	Me/o-1
Cyclo secondary amine		--	Et/o-2	Me/m-2	Me/o-2

Oligomer: average tri-pentamer
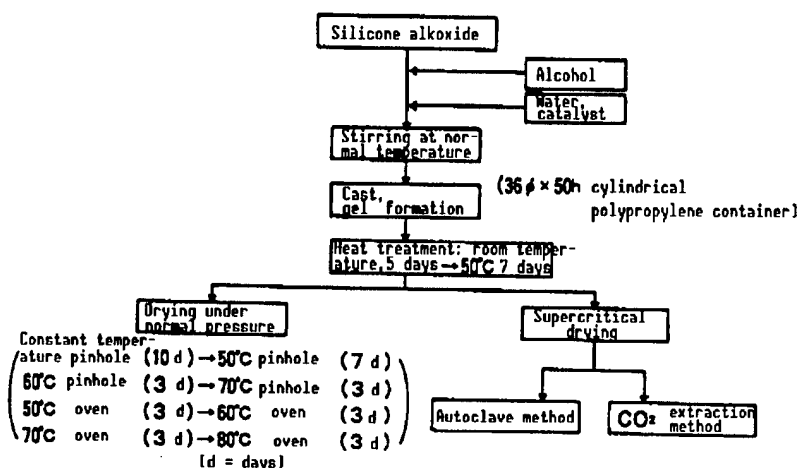
Figure 22. Experiment Flow Sheet

Figure 23. Results of Drying Under Normal Pressure

diameters and more pores in the supercritically dried gel than in the dried gel obtained under normal pressure. As a result, because aerogel maintains open air pores at high temperature, the residual OH group can escape easily, and thus little bubbles are formed during calcination (Figure 25). When Et/o-2, i.e., the oligomer of silicone ethoxide and cyclo-secondary amine,

14

as a catalyst, were used, silica aerogel with a diameter of 80 mm and a height of 220 mm was obtained.
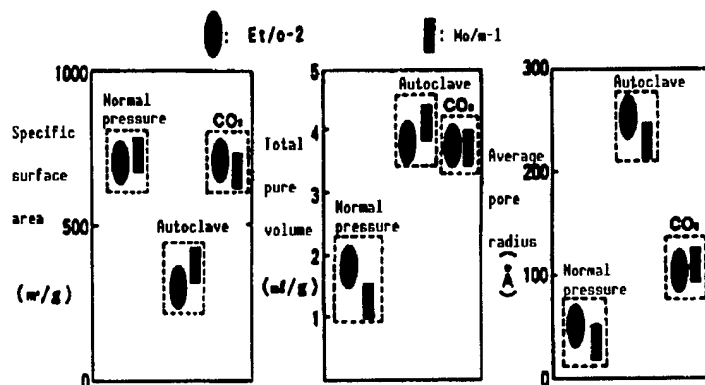
Figure 24. Physical Properties of Dried Gel (1)

Table 12. Physical Properties of Dried Gel (2)

	Specific gravity (g/cc)	Porosity (%)
Drying under normal pressure	0.50	77
Autoclave	0.22	90
CO$_2$ extraction	0.21	90

Sample: Et/o-2

Et/o-2 → Drying under normal pressure
Me/m-1 → Supercritical drying (CO$_2$ extraction)
Et/o-2 → " " (CO$_2$ extraction)
Et/o-2 → " " (autoclave)
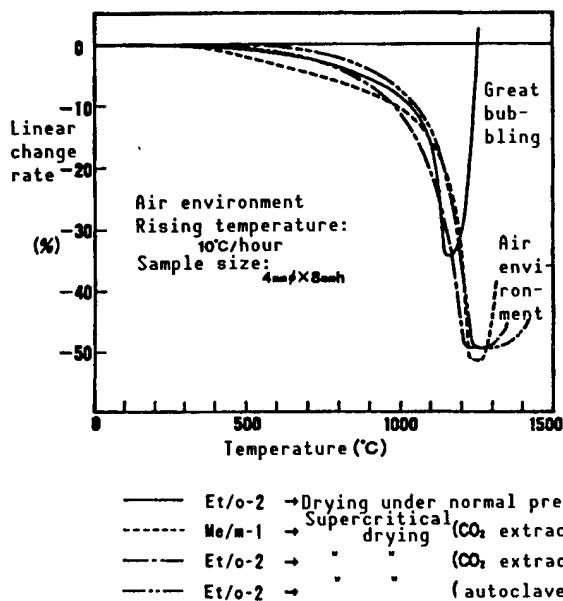
Figure 25. Behavior of Dried Gel During Calcination

15

Such silica aerogel can be considered for use as large silica glass basic material, transparent heat insulation material, acoustic material, and catalyst carrier.

4.4 Control of Sintering

Because of its large specific surface area, dried gel adsorbs large amount of organic such as alcohol, water, and hydroxides. In the case of bulk form, if these are not removed before sintering, they cause a bubbling and cracks. Especially in the case of the basic material for silica glass for optical fiber, the adsorption loss is great; therefore, a heat treatment as shown in Figure 8 becomes necessary.
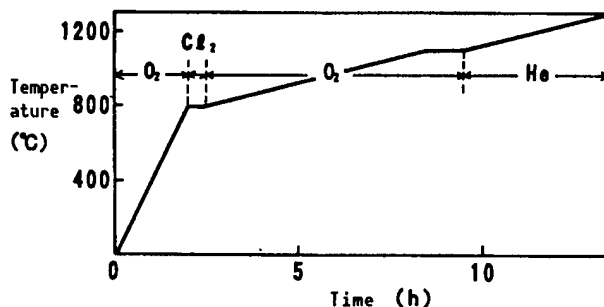
Figure 26. Heat Treatment of Silica Gel for Optical Material Use[12]

Chlorine gas is used to remove hydroxides, but it combines with Si to form Si-Cl, and during the threading engineering process at above 2,000°C, it forms Cl_2 to cause bubbling. Therefore, chlorine is removed.

5. Examples of Application of Each Colloidal Process

5.1 Powder Precipitation Method

By hydrolyzing one or more than two metal alkoxides generally with excess water, single composite or uniform multicomponent composite microparticles with a diameter of about 10-1,000 Å can be obtained as precipitate. Precipitates are oxides, hydroxides, or hydrated oxides; and hydroxides and hydrated oxides are heated to convert them into oxides. More than 100 kinds of ceramics powder have been made.[13] An example is shown in Table 13. Among them, $BaTiO_3$,[14] mullite, and ZrO_2, for example, have already been commercialized. The powder obtained with this method is composed of microparticles with uniform composition, so the temperature for sintering can be lower than for the powder obtained with a conventional method. Furthermore, by controlling the conditions of hydrolysis, forming particles at the same rate, and preventing the aggregation of the particles, a monosuspension of particles with a uniform diameter and shape can be obtained (Table 14). When monosuspension particles are used, a precise sintered ceramic body with uniform crystal particles can be obtained. Also, when the powders of SiO_2 and Al_2O_3 are mixed with carbon powder, and the mixture is heated in nitrogen, a high purity fine powder of Thiaron,[16] nitrogen compounds, and carbon compounds is obtained.

16

Table 13. Application to Powder Manufacture

SiO_2, Si_3N_4, SiC, Si-Al-O-N
Al_2O_3, AlN
MgO, TiO_2, ZrO_2, Ga_2O_3, Ta_3O_5
$3Al_2O_3 \cdot 2SiO_3$
$2MgO \cdot 2Al_2O_3 \cdot 5SiO_2$
$BaTiO_3$, $SrTiO_3$, (Ba,Sr) $(Ti,Zr)O_3$, PZT, PLZT
Y_2O_3-ZrO_2
$YBa_2Cu_3O_{7-x}$

Table 14. Application to Monosuspension
Powder Manufacture[15]

TiO_2
TiO_2 system (BaO, CuO, SrO, Ta_2O_5, Nb_2O_5)
ZrO_2
Y_2O_3-ZrO_2
ZrO_2-Al_2O_3
SiO_2
B_2O_3-SiO_2

5.2 Sol-Gel Powder Method

The 3M Company is manufacturing aluminum polishing agent of several tens to several hundreds μ by pulverizing gel, which is then sintered.[17]

Mitsui Mining Co., Ltd., pulverizes and preheat-treats gel obtained from various metal alkoxides to precipitate fluorphlogopite crystal in a glass matrix, and next, sinters this powder into a form to produce mechanically processible mica crystal glass.[18]

Several companies are making IC sealer from silicone alkoxides.

5.3 Direct Method for Shaping Sol-Gel

(1) Fiber (Table 15)

Table 15. Practical Applications of Fiber
Sol-Gel Direct Forming Method

SiO_2
SiO_2 system (Al_2O_3/TiO_2/ZrO_2/NaO-ZrO_2)
Al_2O_3
Al_2O_3 system (SiO_2/B_2O_3-SiO_2)
TiO_2, TiN
ZrO_2
ZrO_2 system (SiO_2/CaO)
$YBa_2Cu_3O_{7-x}$

Asahi Glass Co., Ltd., is industrially producing SiO_2 fiber by hydrolysis of silicone ethoxide.[19]

The Al_2O_3 line of fibers is being manufactured by Sumitomo Chemical Co., Ltd., which makes it by hydrolysis of alkyl aluminum and aluminum alkoxides, and by the 3 M Company, which industrially produces it from alumina sol.[20]

(2) Sheet manufacturing

Duct blades are used as the manufacturing method. Mitsubishi Mining and Cement Co., Ltd., is industrially producing aluminum sheet of 30-100 μm from aluminum alkoxide.[21]

(3) Manufacturing of coating film (Tables 16 and 17)

Dip-coating is used as the manufacturing method. Generally, after one dip the thickness of the film is below 0.1 μ, but by repeating the process of dip-heating, the film can be thickened. Since the 1950s the Schott Co. of West Germany has been developing mainly the TiO_2-SiO_2 system using metal alkoxides, and has commercialized glass coated with light absorbing film, visible light reflecting film, infrared reflecting film, and reflection proof film.[22]

Table 16. Application to Coating Film (1)

Mechanical protection film:	SiO_2
Chemical protection film:	SiO_2
	SiO_2 system (ZrO_2/B_2O/GeO_2)
	ZrO_2, Al_2O_3
Colored and light absorbing film:	SiO_2 system
	(TiO_2/other transition metal oxides)
	TiO_2
	Cr_2O_3,Fe_2O_3, CoO
Visible light reflecting film:	TiO_2-SiO_2
Infrared reflecting film:	In_2O-SnO_2, TiO_2-SiO_2
Reflection proof film:	TiO_2-SiO_2
	Na_2O-B_2O_3-SiO_2 (before treatment)

Table 17. Application to Coating Film (2)

Strong dielectric film:	$BaTiO_3$, $PbTiO_3$, $KTiO_3$, $KTaO_3$
	$LiNbO_3$, PZT, PLZT
Electron conductive film:	In_2O-SnO_2, CdO-SnO_2, V_2O_5
Ion conductive film:	β-alumina, $LiTaO_3$
Electrochromic film:	WO_3
Optical electrode film:	TiO_2
Catalyst carrier:	TiO_2, Al_2O_3, SiO_3
Superconductor:	$YBa_2Cu_3O_{7-x}$

18

(4) Manufacturing in Bulk Form (Table 18)

Although not yet reaching the stage of industrial production, the manufacture in bulk form is being developed mainly in the SiO_2 system. At Seiko-Epson, a large-scale silica glass has been made by hydrolysis of TEOS and the addition of colloidal silica.[23]

Table 18. Application to Bulk Form

```
SiO₂
SiO₂ system (Na₂O/CaO/SrO/Y₂O₃/TiO₂/ZrO₂
              B₂O₃/Al₂O₃/GeO₂/PbO/P₂O₅/F
                B₂O₃-Al₂O₃-Na₂O-BaO
                PbO-K₂O-B₂O₃)
Al₂O₃,  SiO₃-Al₂O₃
TiO₂
ZrO₂
PbTiO₃
```

At NTT, the glass used as optical fiber that consists of pure SiO_2, GeO_2-SiO_2, and F-SiO_2 is made by growing mature particles after hydrolysis of TEOS with ammonia solution.[24]

6. Future Tasks and Outlook

The problems of colloidal process are the high cost of raw materials and the big shrinkage. However, there is no shrinkage problem for powder and fiber, and the material cost is no problem for a thin film; therefore, some are reaching commercialization.

As to bulk form, it is desirable to develop technology that can make high quality and large-scale silica glass, and to carry out research on oxides other than silica oxides.

In the area of pioneering materials, it appears that by fully utilizing the characteristics of the colloidal process, progress will be made in research as listed in Table 19, such as new composite materials that are difficult to make with conventional manufacturing methods, super uniform materials that fully take advantage of uniformity at the molecular level, and nanocomposite inorganic-organic compounds that focus on the controllability of microstructures.

It is expected, in the future, that each step of the colloidal process will be further elucidated chemically, and the research and development aiming at a high level of quality and function unobtainable with conventional methods will flourish more and more.

19

Table 19.   Future Outlook

---

(1)   Nonoxide and new composition:
          Oxynitride glass[25]
          Carcogenide type glass[26]
          Halide type glass[26]
(2)   Super-uniform body:
          Glass ceramic mullite[27]
          Superconductor
(3)   Molecular level composite: SiC/SiO_2[28]
(4)   Nanocomposite: Zero Heat-expansion body[28]
(5)   Fiber reinforced ceramics (FRC): SiC/SiO_2[28]
(6)   Inorganic-organic complex material:
          Organic modified silicate[29]
          Organic molecular dobsilica gel[30]
          Organic polymer containing silica gel[27]
(7)   Porous body:
          Aerogel
          Porous glass[31]
(8)   Catalyst[32]

References

1.   M. Yamane and T. Kojima, J. NON-CRYSTL. SOLIDS, Vol 44, 1980, pp 182-190.

2.   D.C. Bradley, R.C. Mehrotra, and D.P. Gaur, "Metal Alkoxides," Academic Press, 1978, pp 10-74.

3.   Scherer, Yogyo Kyokaishi, CERAMICS ASSOCIATION JOURNAL, Vol 95, 1987, pp 21-45.

4.   Tashimi Fukui, Chihiro Sakurai, Masahiko Okayama, and Yoshitaka, 1988 Annual Meeting of Japan Ceramics Association, Abstracts, p 75.

5.   K.D. Keefer, "Better Ceramics Through Chemistry," eds. C.J. Brinker, et al., North-Holland, 1984, pp 15-24.

6.   C.J. Brinker and G.W. Scherer, J. NON-CRYST. SOLIDS, Vol 70, 1985, pp 301-322.

7.   S. Wallace and L.L. Hench, MAT. RES. SOC. SYMP. PROC., Vol 32, 1984, pp 47-52.

8.   Hideoyoki Ikoma, Masahiiko Sekine, and Yoshitaka Nomiya, 1988 Annual Meeting of Japan Ceramics Association, Abstracts, p 74.

9.   S. Sakka and H. Kozuka, CHEMISTRY LETTERS, 1987, pp 1763-1766.

10. J. Zarzycki, "Ultrastructure Processing of Ceramics, Glasses, and Composites," eds. L.L. Hench and D.R. Ulrich, John Wiley & Sons, 1984, pp 27-42.

11. Takeshi Fujiyama, Makoto Hori, and Yoshitaka Nomiya, 1988 Annual Meeting of Japan Ceramics Association, Abstracts, p 277.

12. I. Matsuyama, K. Susa, S. Satoh, and T. Suganuma, CERAM. BULL., Vol 63, 1984, pp 1408-1411.

13. Japan Powder Industry Technology Association, ed., "Supermicroparticle Application Technology," Nissan Kogyo Shimbunsha, 1986, pp 76-87.

14. Yoshiharu Ozaki, CERAMICS, Vol 21, 1986, pp 102-110.

15. B. Fegley and E.A. Barringer, MAT. RES. SOC. SYMP. PROC., Vol 32, 1984, pp 187-197.

16. Mamoru Mitomo, Tatsion Shiogai, Hideyoki Yoshimatsu, and Keizo Kitami, YOKYOSHI, Vol 93, 1985, pp 364-369.

17. C.F. Lewis, MATER. ENG., April 1987, p 49.

18. Teijiro Miyake, et al., "Fine Ceramics for Structure," Japan Fine Ceramics Association, 1987, pp 120-124.

19. Hiroki Ohta, NEW GLASS, Vol 8, 1988, pp 25-26.

20. Naozo Horikiri, and Kiyiaki Yasube, "Ceramics Data Book 1980," Industrial Product Technology Association, 1980, pp 332-339.

21. CERAMICS, Vol 21, 1986, pp 162-163.

22. H. Dislich and E. Hussmann, THIN SOLID FILMS, Vol 77, 1981, pp 129-139.

23. M. Toki, S. Miyashita, T. Takeuchi, S. Kanbe, and A. Kochil, J. NON-CRYST. SOLIDS, Vol 100, 1988, pp 479-482.

24. Shozo Shibata, Takeshi Kitagawa, and Masaharu Horiguchi, The 27th Glass Discussion Meeting, 1986, pp 77-79.

25. C.J. Brinker and D.M. Haaland, J. AM. CERAM. SOC., Vol 66, 1983, p 758.

26. NEW GLASS, Vol 8, 1988, pp 27-29.

27. D.R. Ulrich, J. NON-CRYSTL. SOLIDS, Vol 100, 1988, pp 174-193.

28. S.Y. Park and B.I. Lee, Ibid., pp 345-351.

29. H. Schmidt and B. Seiferling, MAT RES. SOC. SYMP. PROC., Vol 73, 1986, pp 739-750.

30. A. Makishima and T. Tani, J. AM. CERAM. SOC., Vol 69, 1986, p C-72.

31. J.D. Mackenzie, "Ultrastructure Processing of Ceramics, Glasses, and Composites," eds. L.L. Hench and D.R. Ulrich, John Wiley & Sons, 1984, pp 15-26.

32. A. Ueno, H. Suzuki, and Y. Kotera, J. CHEM. SOC. FARADAY TRANS., Vol 1, No 79, 1983, pp 127-136.

Research Papers by Ceramic Society Members

CeO_2-TiO_2-SiO_2 Coating Film by Sol-Gel Method

43067612 Tokyo NIPPON SERAMIKKUSU KYOKAI KANTO SHIBU KENKYU HAPPYOKAI in Japanese 4-5 Aug 88 p 1

[Article by Akio Makishima, Mitsuaki Asmai, Akira Mamiya, and Kenji Wada, NIRIM, Tokyo University, and Sasaki Glass]

[Text] 1. Introduction

A CeO_2-TiO_2 coating film made by the sol-gel method with the use of cerium containing titanium-alkoxide assumes a clear yellow color. This film has been reported to improve chemical resistance and abrasion resistance.[1] At this time, in order to improve the acid-proof quality of this material, a coating film composed of the CeO_2-TiO_2-SiO_2 system was manufactured from a CeO_2-TiO_2 coating film by using ethyl silicate. This report discusses any investigation of the manufacturing conditions of this new material and its physical properties.

2. Experiments

The dipping solution was prepared as follows. $Si(OC_2H_5)_4$ was diluted by EtOH, and $CeCl_3 \cdot 7H_2O$ was dissolved. $Ti[OCH(CH_3)_2]_4$ was added to make the mol ratio Ce:Ti:Si become 1:1:1. After this solution was aged for the prescribed time under the specified temperature, the slide glass and aluminum foil were immersed. Then, they were lifted out and dried at room temperature. Subsequently, they were heated for 5 minutes at 500°C at normal pressure. Through these procedures, the coating film was obtained, and its physical properties were evaluated.

3. Results and Conclusion

The coating film obtained just after the manufacturing processes had an unclear emulsive color. After being aged for 4 days at room temperature, it became a homogeneous clear yellow film.

Figure 1 shows the transmittance vs wavelength of the film obtained by one coating on the slide glass. The transmittance of the CeO_2-TiO_2-SiO_2 system is apparently higher than that of the CeO_2-TiO_2 system. When the
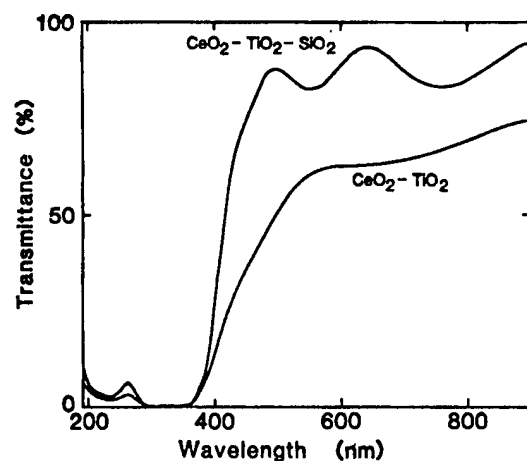
Figure 1. Transmittance of CeO_2-TiO_2-SiO_2 Coating Films
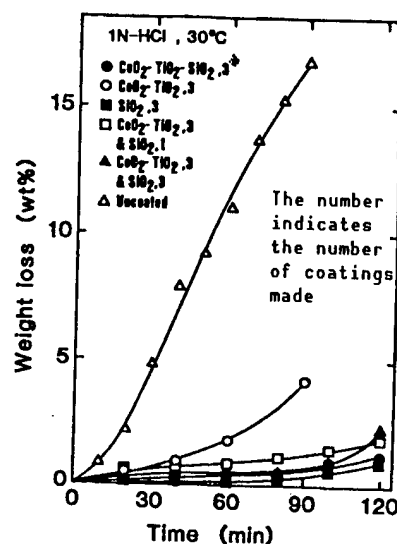
Figure 2. Acid-Proofness of Coating Films

chromaticity of the film was measured, the intensity of the yellow (about 570 nm) became stronger as the number of coatings increased, similar to that of the CeO_2-TiO_2 system. The intensity of the yellow color was stronger for the CeO_2-TiO_2 system after the same number of coatings.

Figure 2 shows the result of acid-proof tests (coating on aluminum foil). It is observed that an improvement in the acid-proofness has certainly made for the CeO_2-TiO_2 coating film, but that of the CeO_2-TiO_2-SiO_2 system is more extensive, and is almost comparable to that of the SiO_2 coating film.

References

1.   A. Makishima, H. Kubo, K. Wada, Y. Kitami, and T. Shimohara, J. AM. CERAM. SOC., Vol 69, 1986, p C-127.

Effect of Solvent on Dried Gel Structure by Sol-Gel Method

[Article by Fusashi Hayashi, Yasukazu Takei, Yoichi Machii, and Toshikatsu Shimazaki, Hitachi Chemical Research Institute and Tsukuba Research Institute]

[Text] 1. Introduction

In recent years, the direct synthesis of bulk-shaped glass by the sol-gel method has been observed, and extensive studies have been conducted. However, sol adjusted solvents are not being studied actively. Therefore, in this report, various solvents under sol adjustment have been investigated, and the effect of the solvents on the dried gel structure is discussed.

2. Experiments

Tetramethoxysilane ($Si(OCH_3)_4$: TMOS), water, the catalyst, and the organic solvent were mixtured at the volume ratio of 1:0.47:1.18 (when methanol was used as the solvent, the mol ratio was 1:4:4.5), and the sol solution was prepared. Hydrochloric acid was used as the catalyst (0.0001 mol/l). After the sol solution was mixed well, about 30 ml of the solution was put into a glass Schale dish with an inside diameter of 65 mm. It was sealed by aluminum foil, and gelation was allowed to take place at room temperature. Then, pin holes were placed in the aluminum foil, and it was dried at 50°C The bulk density of the dried gel was measured in terms of the outer dimensions and weight. The volume of ores was obtained by a nitrogen absorption measurement device--Carlo Erba Corporation's Sorptomatic 1800 Model.

3. Results and Conclusion

Figure 1 shows the bulk density of the dried sol prepared by using various solvents. The uniform sol solutions could not be controlled by a single solvent when some of these solvents were used. The mixed solvent with methanol was used for all solutions. Nevertheless, the boiling point of a single solvent was used in Figure 1 for reasons of convenience. When attention is paid to alcohol, a correlation apparently exists between the bulk density and the boiling point of the solvent. It shows that the bulk density decreases as the boiling point of the solvent increases. However, this tendency was not observed for 1.4 dioxane.

Figure 2 shows the relationship between the bulk density of the dried gel and the average pore radius and volume of the pore. As the bulk density of the dried gel becomes larger, both the average pore radius and the volume of the pore decrease. A close relationship exists between them. From these results, it is clear that the solvent greatly influences the structure of the dried gel. A discussion was made of the reasons for this phenomenon.
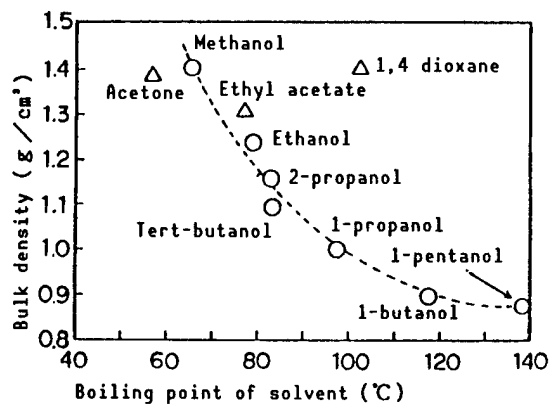
Figure 1. Bulk Density of Dried Gel
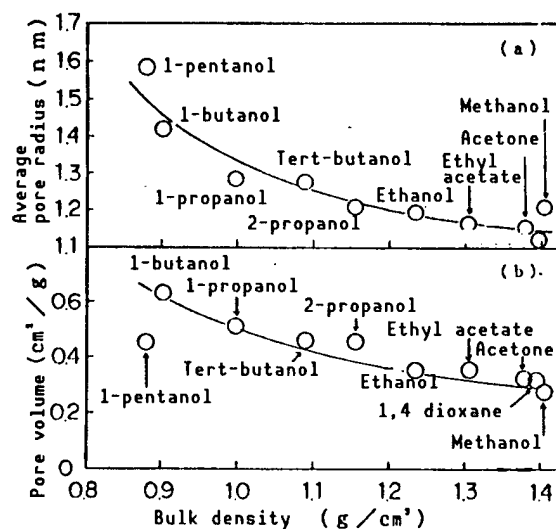
Figure 2. Average Pore Radius and Pore Volume of Dried Gel

ITO Film Manufactured by Sol-Gel Method

[Article by Toshio Tsuchiya, Tadashi Sei, Fumiaki Iiya and Takano Yamauchi, Tokyo University of Science]

[Text] 1. Introduction

ITO film is made by doping indium oxide with tin. This thin film exhibits optically high transmissibility in the visual region and high reflection in the infrared region. It also possesses high electrical conductivity. In the past, it was difficult to form films efficiently on large or complicated

26

shapes by using a vacuum vessel and the conventional methods. In this paper, an immersed application that compensates for the defects of the conventional methods is discussed.

2. Experiments

The solution was prepared by the following procedure. Convection of the indium solution took place at 120°C by adding indium nitrate and acetylacetone. Tin was dissolved by nitric acid and acetylacetone was added to it, providing the tin solution. The application solution was made from the indium solution by adding an appropriate amount of the tin solution and acetone. In making the films, first a quartz glass substrate was immersed into the application solution, and lifted out at a speed of 0.2 cm/s. Then, it was dried at 70~80°C in the air, and thermally processed in an oxygen environment.

3. Results

According to the DTA·TG measurements, oxidation of the ITO film was completed around 400°C, with no weight reduction occurring. It was determined from IR measurement that the solvent vanished at 400~500°C. Through X-ray diffraction analysis, the heat treatment conditions selected were 500°C and 5 hours, according to the state of the crystal. Figure 1 shows temperature dependence of the film's conductivity. The numbers in the figure indicate the mol percentage of tin for each film. In both cases, similar temperature dependence of the conductivity is seen. From these results, it can be assumed that the conductivity mechanism of the films is not drastically affected by the amount of tin added. Figure 2 shows the transmissivity in the visible region for the film exhibiting the highest conductivity in this study. Since photo absorption in the visible region by the ITO film was caused by the density of carrier electrons and lattice defects, transmissivity decreased as the electric conductivity increased. However, as seen from Figure 2, the transmissivity of quartz glass with the film was about 80 percent that of simple quartz glass, but its permeability was very high. It is concluded that the high permeability and electric conductivity in the visible region are satisfactory for use in a transparent electrode.

Figure 1. Temperature Dependence of the Film Conductivity

Figure 2. Transmissivity of ITO Film in Visible Region
o: Quartz glass
•: Quartz glass + ITO

Irradiation Characteristics of Tritium Breeding Materials

43067612 Tokyo NIPPON SERAMIKKUSU KYOKAI KANTO SHIBU KENKYU HAPPYOKAI in Japanese 4-5 Aug 88 p 6

[Article by Kenji Noda and Hitsohi Watanabe, JAERI]

[Text] 1. Introduction

Atomic fusion reactor tritium breeding materials are used to produce tritium for fuel, and also are used to convert nuclear energy into thermal energy. They are mainly composed of Li and Li-chemical compounds. The Japan Atomic Energy Research Institute selected Li_2O as a candidate for tritium breeding materials and has been studying various properties of this material, including the irradiation characteristics. In this paper, irradiation damage of Li_2O and the effect of irradiation on ion conductivity will be discussed.

2. Experiments

After an Li_2O single crystalline sample made through the flotation band fusion method was irradiated by an oxygen ion with energy of 0.5~120 MeV or the thermal neutron reactor (JRR-4), defects caused by the irradiation were investigated by the electron spin resonance (ESR) method. In addition, while the Li_2O single crystalline sample was being irradiated by a 120 MeV oxygen ion, irradiation was occasionally discontinued and the ion conductivity was measured by the alternating current two-terminal method.

3. Results

Figure 1 shows the ESR spectra parallel to the external magnetic field of the ESR spectrometer when the Li_2O single crystalline sample was irradiated by a thermal neutron of 4.5×10^{21} n/m^2 in the crystalline lattice directions of <100>, <110>, and <111>, respectively. These spectra have ultrafine structures comprising more than 20 peaks. Their directional dependence is quite consistent with the ultrafine structure strength ratio calculated

assuming the existence of an F^+ center (an oxygen hole to capture an electron) in Li_2O under each vector. From this fact, these spectra can be identified as the F^+ center. The F^+ center is the principal irradiation defect of Li_2O caused by thermal neutron irradiation and oxygen ion irradiation. It is recovered at 500~670 K.
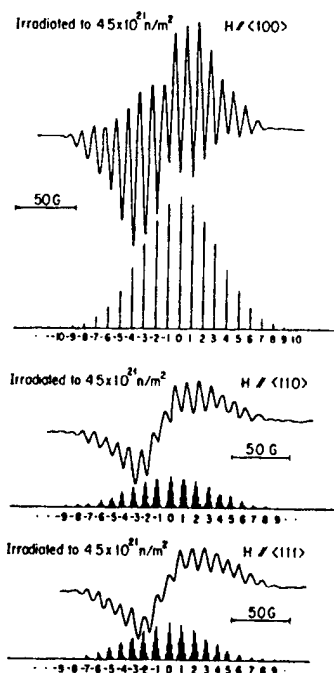
Figure 1. ESR Spectra of Li_2O Irradiated by Thermal Neutron
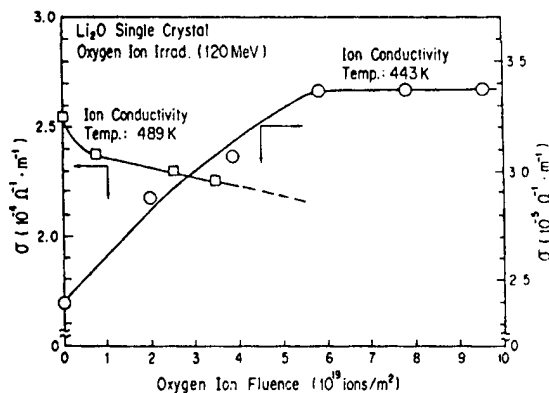
Figure 2. Relationship Between Ion Conductivity and
the Amount of Irradiation

Figure 2 shows the relationship between ion conductivity and the amount of oxygen ion irradiation for the Li_2O irradiated by oxygen ions at 489 and 443 K. Ion conductivity at 489 K decreases as the amount of irradiation

decreases. On the other hand, at 443 K, ion conductivity increases as the amount of irradiation increases, and it becomes saturated at irradiation of more than 6 x 10^{19} ions/m^2. From the results of recovery experiments following irradiation, the decrease and increase of ion conductivity by irradiation at 490 K and 440 K, respectively, are thought to originate from the F^+ center and unidentified irradiation defects generated by irradiation.

Phase Stability of Metastable Tetragonal Zirconia

43067612 Tokyo NIPPON SERAMIKKUSU KYOKAI KANTO SHIBU KENKYU HAPPYOKAI in Japanese 4-5 Aug 88 p 7

[Article by Hideo Ohno, JAERI]

[Text] 1. Introduction

When zirconia is used as a ceramic characterized by high toughness, the phase transformation of ZrO_2 (tetragonal → monoclinic) becomes important. Many studies have been conducted on this subject. In this paper, the thermal effect on phase transformation, such as from a metastable to a stable phase and from a tetragonal to a monoclinic phase, for pure ZrO_2, that could be a basis for future reinforced ceramics, will be discussed.

2. Experiments

$ZrOCl_2 \cdot 8H_2O$ was thermally decomposed in the flow of oxygen gas at 450°C for 12 to 15 hours, and a metastable tetragonal phase (98~100 percent) was produced. The phase transformation of the test specimen was monitored by a wide angle neutron diffraction device in a high flux isotope reactor (HFIR) at Oak Ridge National Laboratory (ORNL), United States, under the certain time (10^0~10^4 min) and temperature (650~950°C) parameters. The same test specimen was also examined by the high temperature X-ray diffraction method.

3. Results

The size of the crystallite of the test specimen used in this study was 15~20 nm at normal temperatures. Time dependence is shown in Figure 1 as an example of the phase transformation measurement results of a stable monoclinic phase from metastable tetragonal ZrO_2 obtained by the neutron diffraction method. A volume ratio for the tetragonal to monoclinic phase was calculated from three peak areas obtained by the least squares method. A volume ratio (Fraction = f(t)) of the monoclinic phase that increased with time was analyzed from the Abrami equation.

$$\text{Fraction} = f(t) = 1 - \exp[-(t/\tau_0)^n]$$

From the analytical results at 650~950°C shown in Figure 2, some kind of thermal activation mechanism seems to be exerted. However, if the idea of a critical particle diameter is introduced, these results could be explained by martensite-type phase transformation.
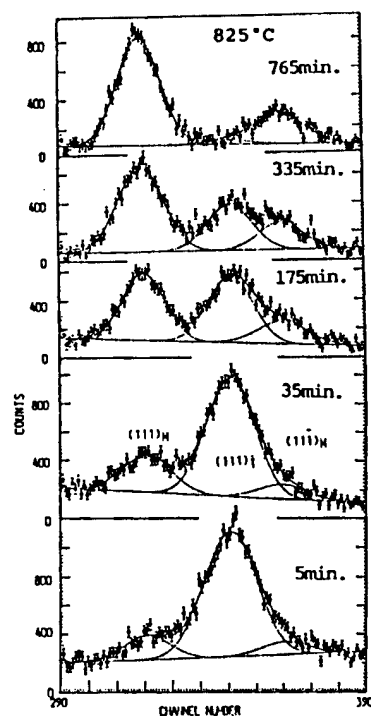
Figure 1.   Deconvolution of Diffraction Patterns of Tetragonal $(111)_T$ and Monoclinic $(111)_M$ $(11\text{-}1)_M$ Phases at Different Times at 825°C
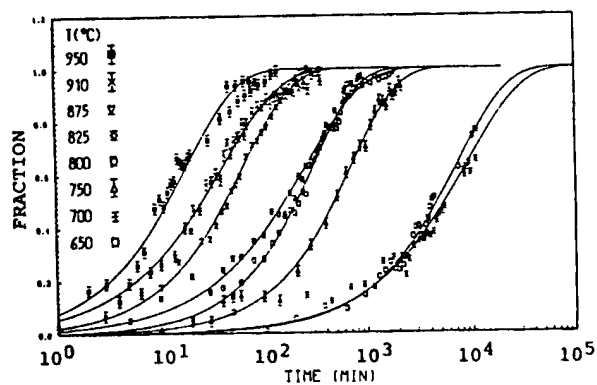
Figure 2.   Time Dependence of Conversion of Metastable Tetragonal ZrO_2 to Monoclinic ZrO_2 at Different Temperatures by Neutron Diffraction

31

Diamond Separation by Microwave Plasma Method

[Article by Matsukazu Kamo, Fumio Takamura, and Yoichiro Sato, NIRIM]

[Text] 1. Introduction

In order to magnify a microwave plasma generation area and to separate a diamond film over a large area, various kinds of electric discharge methods were investigated. Among them, the most suitable method was chosen, and the synthesis of a diamond film on a 40-inch silicon wafer substrate was examined. As a result, separation of the diamond film over the entire area was confirmed.

2. Electric Discharge Experiment

Some kinds of electric discharge methods investigated are shown in Figure 1. For the diamond film synthesis experiment conducted in this study, the method shown in Figure 1(d), i.e., the technique inducing microwaves from two directions relative to a cavity, was adopted. Under this method, plasma is limited in the direction of the microwave propagation, but it covers the entire diameter in the central portion of the cavity. In addition, this method enables the base to be heated until the necessary temperature for diamond separation is obtained, without using other heating methods.
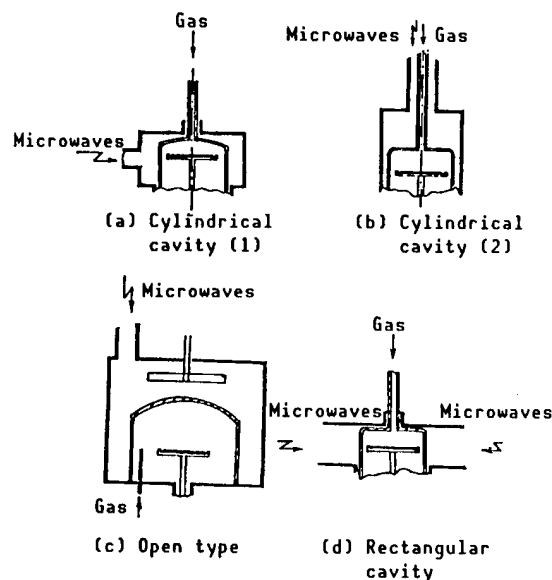
Figure 1. Kinds of Microwave Electric Discharge Methods

3. Diamond Film Synthesis Experiment

Within the limits of the synthesis conditions listed in Table 1, diamond synthesis was carried out by changing the distribution of an electric field in the cavity. The synthesized diamond films were evaluated by SEM observation and Raman spectroscopy in terms of the distribution of film thickness and quality. The distribution of film thickness depends largely upon the distribution of an electric field in the cavity. Due to the addition of argon gas and the use of a low speed rpm for a substrate stand, fluctuations in the film thickness were reduced. The quality of the synthesized diamond became better as the methane concentration decreased and flux increased. On the other hand, however, the addition of argon gas and the reduction of the rotation speed of the substrate stand, although effective in improving the fluctuation in film thickness, resulted in the tendency to deteriorate.

Table 1. Synthesis Conditions

Raw gas	H_2, CH_4
CH_4 concentration (vol%)	0.5, 1.0
Flux (sccm)	100, 250, 500
Pressure (kPa)	2.7, 3.3, 4.0
Number of rotations of substrate stand (rpm)	4, 8, 16
Temperature of substrate at center (°C)	860
Synthesizing time (hours)	20

4. Conclusion

As a result of several kinds of electric discharge experiments, it was possible to magnify an electric discharge field and also to heat the substrate to the necessary temperature for diamond separation without using other heating methods by inducing microwaves into a rectangular-shaped cavity from two directions. Using this method, a diamond film was separated from an entire 40-inch substrate, and diamond with uniform film thickness was obtained in an area with a diameter of about 60 mm. The quality of the diamond separated was better from the circumference of the substrate than from the central portion. This was thought to be caused by the shape and configuration of the plasma and the nonuniformity in the temperature of the substrate.

Diamond Synthesis by Direct Current Plasma Jet

[Article by Seiichiro Matsumoto, Takeshi Chonan*, and Toyohiko Kobayashi**, and Yusuke Moriyoshi, NIRIM, *Sumitomo Metal, and **Tokai Carbon]

[Text] 1. Introduction

In order to synthesize diamond at a high speed, the authors reported the achievement of the high-speed synthesis technique based upon the high-frequency waves plasma method, which is about 100 times faster than the conventional CVD method. As a consistent high-speed synthesis technique, diamond synthesis using direct current arc electric discharge was conducted. The conditions of synthesis and an evaluation of the synthesized diamond will be discussed in this paper.

2. Experimental Methods

Figure 1 shows an outline of the diamond synthesis device using the direct current plasma jet as employed in this study.
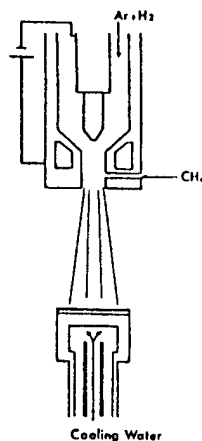
Figure 1. Schematic Diagram of DC Plasma

After a plasma generation chamber was exhausted, becoming about 10^{-2} torr, a mixed Ar and H_2 gas was introduced in the chamber as the plasma generation gas. By maintaining the pressure at 100~760 torr in the plasma generation chamber, plasma was generated by the arc electric discharge between the cathode and the anode. As the carbon resources, CH_4 of 1~40 percent by volume was introduced into the plasma. An experiment to separate diamond on the surface of a Mo plate on a water-cooled substrate holder was conducted.

The analysis of separated materials was carried out by XRD, Raman spectroscopy, and SEM.

3. Experimental Results

Photograph 1 [not reproduced] shows typical examples of the surface and cross sectional SEM image of the film produced under a separating chamber pressure of 760 torr and CH_4 concentration of 10 percent by volume. This separated film was confirmed to be diamond by Raman spectroscopic analysis and XRD.

The surface SEM image of the film indicated that there was relatively complete idiomorphic diamond configuration. From the film thickness on the cross sectional SEM image, the growth speed of the film was determined to be about 4 μm/min.

When the concentration of CH_4/H_2 and the substrate temperature were adequate, diamond possessing a fine idiomorphic plane could be separated. Diamond plasma generation gas by CH_4 concentration was similar to that by the high-frequency wave thermal plasma method.

The maximum growth speed of a diamond film obtained by this method was about 4 μm/min at normal pressure, and about 9 μm/min at decompression (140 torr). It was confirmed that diamond synthesis is possible at high speed and high CH_4 concentration.

Diamond Sintering Body With Low Metal Content

43067612 Tokyo NIPPON SERAMIKKUSU KYOKAI KANTO SHIBU KENKYU HAPPYOKAI in Japanese 4-5 Aug 88 p 14

[Article by Hiroshi Akashi, Toshikazu Osawa, and Nobuo Yamaoka, NIRIM, and Osamu Fukunaga, Tokyo Institute of Technology]

[Text] 1. Introduction

In order to synthesize a diamond sintering body with high hardness and electrical insulation, the synthesis of a diamond sintering body containing a small amount of metals has been studied for the past several years. The influence of the amount and kind of metal added on the heat-resistant properties of a diamond sintering body containing a small amount of metal was specifically investigated here. This paper discusses the results.

2. Experimental Procedures

Table 1 shows the composition of starting materials. These starting materials were sintered under the conditions of 8 GPa, 2,000°C, and 1 hour in a belt-type high pressure device. After the sintered materials were polished, they were thermally processed at 1,100°C and 0.7~1.4 x 10^{-5} torr for 30 minutes by a high-frequency wave induction reactor. The heat-resistance of the sintered materials was evaluated by X-ray diffraction after heat treatment, SEM observation of the surface of the sintered materials was made, and the change in weight of the materials before and after heat treatment was measured.

Table 1. Starting Materials and Heat Resistant Properties

Sample number	Starting materials		Heat resistant properties	
	Diamond	Additive	Graphitization	Cracks
DN-5	2~4 μm	5 vol% Ni Mechanical mixing	Small amount	Microcracks
DNSpu	2~4 μm	1 vol% Ni Magnetron sputtering	Small amount	No
DC-5	2~4 μm	5 vol% Co Mechanical mixing	No	Many cracks
DCoSpu	2~4 μm	1.5 vol% Co Magnetron sputtering	No	Two cracks
DInSpu	2~4 μm	1.2 vol% Invar Magnetron sputtering	No	No

Invar: Super Invar; Ni 31%, Co 4~6%, Mn 0.3~0.4%, C 0.07%,
     Remainder Fe.

3. Experimental Results and Discussion

All five kinds of sintered materials shown in Table 1 are homogeneous sintered materials (Figure 1 [not reproduced]) composed of fine particles with diameters of several microns. Table 1 summarizes the extent of graphitization of each diamond sintering body and the crack generation after heat treatment. For the case of the diamond sintering body to which Co or Invar was added, no type of graphitization was observed. On the other hand, when Ni was the added sintering body, graphitization was seen due to heat treatment regardless of the amount of metal added. SEM observation of the surface of the sintered materials after heat treatment indicated that globular-shaped metals were separated in the grain boundary of the diamond (Figure 2 [not reproduced]). The number of cracks caused by heat treatment strongly depended upon the amount of metal added and its coefficient of thermal expansion. For DNSpu and DInSpu, to which small amounts of metal had been added and which had small coefficients of thermal expansion, no cracks were observed.

The results of this study indicated that the diamond sintering body to which a small amount of Invar had been added had excellent heat resistance.

Effect of Neutron Irradiation on Fine-Grained Isotropic Graphite

[Article by Tatsuo Oku, Motokuni Eto and Shintaro Ishiyama, JAERI, Tokai Plant]

[Text] 1. Introduction

A large amount of graphite materials is used for the core of a high temperature gas cooling reactor.   There is a plan to use fine-grained isotropic high strength graphite in the core of the high temperature testing reactor (HTTR) that is presently under research and development by the Japan Atomic Energy Research Institute.   In order to evaluate the stresses generated inside the core with a graphite structure, the effects of neutron irradiation on strength, Young's modulus, and the irradiation creep characteristics of fine-grained isotropic graphite have been studied, and the results will be discussed in this paper.

2. Method

The test specimen was fine-grained isotrophic graphite IG-110 (made by Toyo Carbon Corp.) scheduled for use in the HTTR. Irradiation creep test pieces, with a total length of 80 mm, were prepared for the tensile test. The cross section at a parallel portion had a square shape, with three different side lengths appearing--3.6, 4.0, and 4.4 mm. The dimensions of an unloaded testpiece were $4 \times 4 \times 39$ mm^3. The Young's modulus and bending strength were also measured by the above testpiece. The Young's modulus was obtained from an ultrasonic wave propagation speed (v) and bulk density (ρ), i.e., the Young's modulus $E = \rho v^2$. Irradiation took place until 1.8×10^{25} n/m^2 (E > 29 fJ) at 756~984°C was reached by the JMTR. Stress of 9~14 MPa was added to creep testpieces.

3. Results

Irradiation creep strain depends upon the irradiation conditions and stress. Under the conditions adopted in this experiment, it was 0.5~1.3 percent. As shown in Figure 1, if irradiation creep strain ϵ_c is written as

$$\epsilon_c = (\sigma/E_0)\{1 - \exp(-b\Phi)\} + K\sigma\Phi = \sigma/E_0 + K\sigma\Phi$$

and an irradiation creep coefficient K is obtained, the average of five testpieces became $K = 4.20 \times 10^{-29}$ (MPa/m^2)$^{-1}$. The Young's modulus was increased by a maximum of 48 percent from 9.42 GPa before irradiation, as shown in Figure 2. Bending strength was increased by 24~32 percent from 34.7 MPa before irradiation. As seen in Figure 3, the relationship between the Young's modulus and bending strength seems to be dependent upon the irradiation temperature (Figure 3).
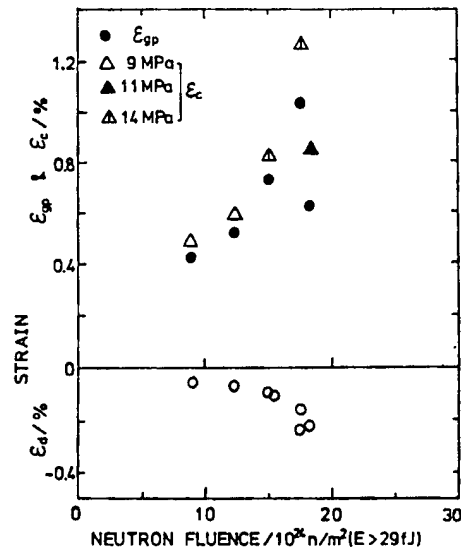
Figure 1. Irradiation Dependence on Creep Strain of IG-110 Graphite
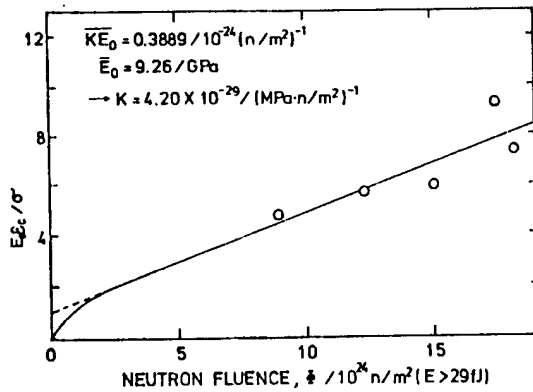
Figure 2. Irradiation Dependence
on Irradiated Creep Strain
Normalized by Initial Strain
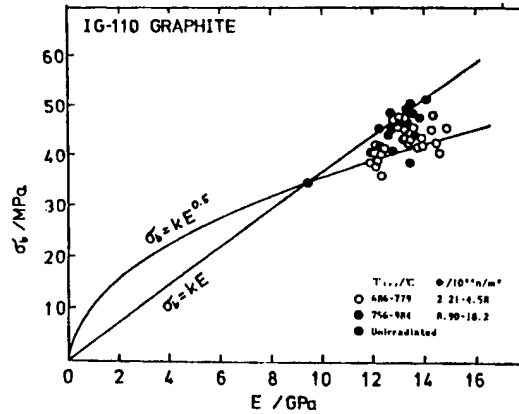
Figure 3. Young's Modulus and
Bending Strength of
IG-110 Graphite

Characteristics of AlN Powder by Alumina Reduction Method

[Article by Ippei Yamamoto and Hitofumi Taniguchi, Tokuyama Soda]

[Text] 1. Introduction

In 1984, sintered AlN exhibiting optical permeability was developed first in the world by using AlN powder and the Al_2O_3 reduction method.[1] Because of this development, many studies of AlN powder for use as high thermal conductivity sinters have been conducted. However, there have been few studies about the relationship between the physical properties of raw material Al_2O_3 and those of AlN powder. In this study, AlN powder was synthesized by using different kinds of Al_2O_3 as raw materials, and its physical properties were examined from the viewpoint of raw materials to be used for sinters.

2. Experimental Procedures

Raw Al_2O_3 was mainly classified into three types based upon primary particle size (SEM observation) and cohesive particle size (sedimentation method) (Table 1). The procedure used to synthesize AlN powder was as follows. First, Al_2O_3 and carbon were mixed by a ball mill at the ratio of 1:1. Then, the mixture was baked at 1,600°C for 6 hours under the flow of N_2 gas. After that, surplus carbon was combusted and eliminated in an oxidation environment. Examination by X-ray diffraction indicated that the synthesized powder was single phase AlN. The specific surface, particle size, forming density, and sintering of the AlN powder were examined.

Table 1. Three Types of Al_2O_3

Types of Al_2O_3	I	II	III
Primary particle size (SEM observation)	$\leq 0.5\ \mu m$	$\leq 0.5\ \mu m$	$\geq 1.0\ \mu m$
Cohesive particle-size (Sedimentation method)	$\leq 1.0\ \mu m$	$\geq 1.0\ \mu m$	$\geq 1.0\ \mu m$
AlN symbol corresponding to Al_2O_3	□ ■	Δ ▲	o ●

3. Results and Conclusion

Figure 1 shows the relationship between the primary particle size (D_1 diameter) of raw Al_2O_3 and the D_1 diameter and specific surface of the AlN powder. As the particle size of the Al_2O_3 decreased, the specific surface of the AlN powder increased. It became very large in the case of $D_1(Al_2O_3)$ $\leq 0.5\ \mu m$. On the other hand, the D_1 diameter of the AlN powder was not

influenced by the D_1 diameter of the factory automation. However, in the case of $D_1(Al_2O_3) \geq 1$ μm, a ring-shaped cohesive AlN powder was obtained, although its formation process was not understood.
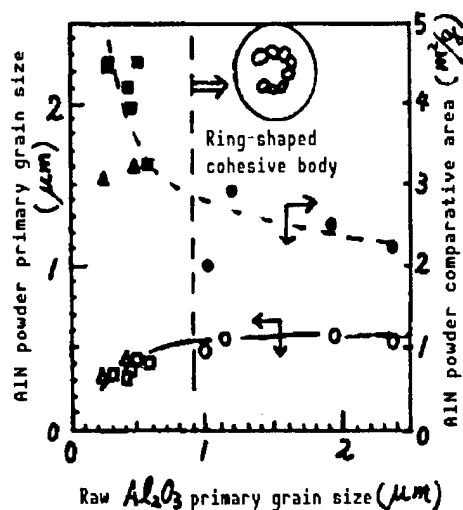
Figure 1. Relationship Among Primary Grain Size of Al_2O_3, D_1 Diameter and Comparative Surface Area
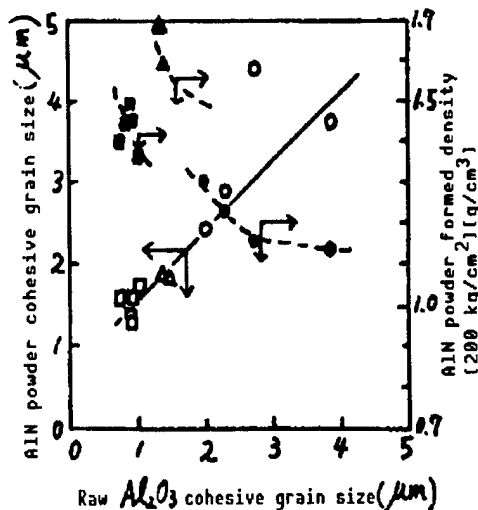
Figure 2. Relationship Among Cohesive Particle Size of Al_2O_3, D_2 Diameter and Forming Density of AlN Powder

Figure 2 shows the relationship between the cohesive particle size of the Al_2O_3 and the D_2 diameter and forming density of the AlN powder. A positive correlation between the D_2 diameter of Al_2O_3 and that of AlN. Slightly cohesive AlN powder exhibited high forming density. The forming density of Type II raw Al_2O_3 was particularly high. This could have been caused by the very fine cohesion of primary particles. For such a powder, voids which have migrated in a cohesive body do not escape easily during the sintering process. As a result, a low density sintering body is obtained. Ring-shaped cohesive AlN powder (raw Al_2O_3 of Type III) exhibited very low forming density, and the density of the sintering body was also low.

Figure 3 shows the effect of the specific surface and forming density of the AlN powder on its sintering properties. It can be seen that in order to obtain a sintered body with high density, a powder possessing both high specific surface and high forming density is required. In addition, it was found that in order to produce this AlN powder by the Al_2O_3 reduction method, slightly cohesive raw Al_2O_3 with D_1 of less than 0.5 μm was more suitable.
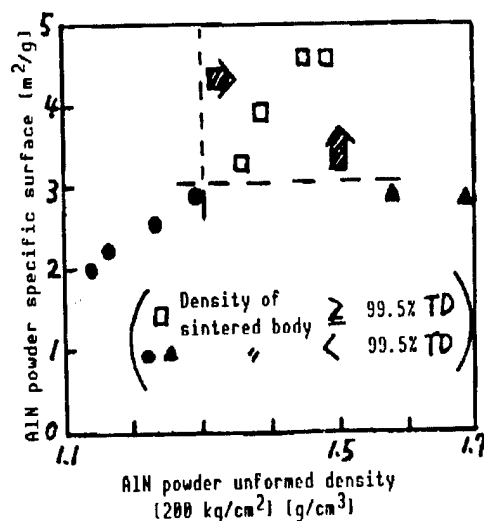
Figure 3. Effect of the Specific Surface and Forming Density
of AlN Powder on Sintering Properties

References

1.   N. Kuramoto and H. Taniguchi, J. MATERIAL SCIENCE LETT., Vol 3, 1984,
      p 471.

Dispersion Characteristics of AlN Powder

[Article by Kiyoaki Hirokawa, Sadakazu Fujimoto, and Hitofumi Taniguchi,
Takuyama Soda]

[Text] 1.   Introduction

When forming ceramics, an improvement in slurry dispersion not only makes
forming easy, but also improves the physical properties of a formed body.
Slurry dispersion is governed by the surface properties of the ceramic
powder. In order to improve wetting between a powder and a solvent, a
surface activator matching a slurry system is usually used. In this study,
different kinds of surface activates were added to AlN powder, and the
slurry dispersion and physical properties of the green sheet formed by the
doctor blade method were investigated.

2.   Experiment

Surface activators A~F, all available on the market, were added to AlN
powder (Tokuyama Sotatsu-F grade). It was mixed by a ball mill in a
toluene-ethanol mixture solvent, and the dispersion characteristics of the
slurry obtained were studied. In addition, after a binder was added and
remixed, sheet formation was attempted and the sheet formation
characteristics were investigated.

3. Results

Figure 1 shows the relationship between the HLB value of the surface activator and the viscosity of slurry. With the HLB value of 7 referred to as a standard, the viscosity of the slurry of a lipophilic surface activator became 2,000~4,000 cps, and the slurry exhibited a low dispersion state. On the other hand, the viscosity of the slurry of a hydrophilic surface activator was in the range of 20~30 cps, indicating a high dispersion state. The hydrophilic surface activator exhibited a substantial absorption force on the AlN surfaces. Figure 2 shows the relationship between the HLB value of a surface activator and the tensile strength and density of a sheet. The strength of the sheet employing a lipophilic surface activator with a small HLB value was high, with that of sheet A reaching 25 kg/cm². When a hydrophilic surface activator was used, the sheet strength decreased monotonously, with that of sheet F being 5 kg/cm². This fact might be explained by the difference in the hydrophilic property of a surface activator relative to a binder. It is thought that a lipophilic surface activator shows larger affinity. However, cracks occurred in sheets A and B, and the dispersion state of a slurry influenced the sheet forming property. Sheet density tended to become the highest when the HLB value became 7. It was thought that the vicinity of the HLB value of 7 was the balanced point of affinity between the AlN surface activator and a binder. Accordingly, AlN particle package became the densest. Obtaining a highly dense sheet is very important in improving the properties of a sintered body. Through this study, it was found that the HLB value of the surface activator was an important index of the sheet forming property.
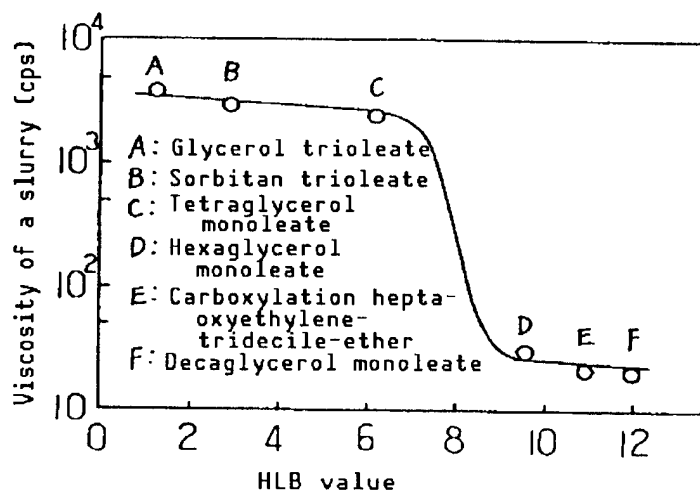
Figure 1. Relationship Between the HLB Value of a Surface
Activator and the Viscosity of a Slurry

$$d_g = \frac{\text{raw density of formed body}}{\text{} } \times \frac{\text{[AlN weight in a slurry]}}{\text{[weight of slurry]} - \text{[weight of solvent]}}$$
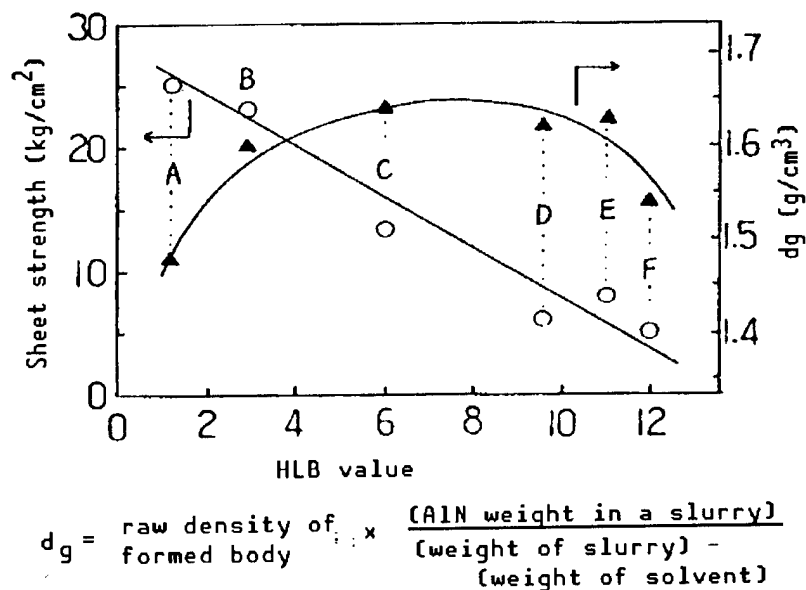
Figure 2. Relationship Between HLB Value of Surface Activators
and Tensile Strength and Density of Sheets

TiC Single Crystal Grown From Self-Combustion Sintered Bar

[Article by Shigeki Otani, Takazumi Tanaka, and Yosho Ishizawa, NIRIM]

[Text] 1. Introduction

A TiC single crystal has been observed as a field emitter material enabling an extremely stable current to be discharged.[1]. This material requires a highly pure single crystal. However, W impurities contained in the raw material powder cannot be removed, even by the FZ method, under the 2,900°C temperature required for the growing process. This usually causes problems during the growing process. In this study, in order to remove W, TiC was synthesized and a sintered bar was manufactured by the self-combustion method. As a result, several advantages for the growing process were discovered, and the growing process problems were solved.

2. Experiment

After Ti metal powder and degassed carbon powder were mixed under a prescribed ratio (C/Ti = 0.99), they were formed by a rubber press, producing a cylindrical compressed powder body. It was then placed with a graphite susceptor. One end was inserted into a heater in a vacuum at 1,300°C, generating a self-combustion reaction. The sintered bar produced was set in a high-frequency FZ reactor, and a single crystal was grown in the direction of <100>[3] by controlling the crystalline structure to C/Ti = 0.96 by the m-ZL method.[2]

3. Results and Conclusion

The self-combustion sintered bar featured low density (43 percent) and high purity. Due to the low density, the electric power of reheating was reduced by 10 percent. This is a great advantage when growing a single crystal at such high temperatures.[4]

Due to the high purity, the purity of a single crystal was improved more than 10-fold (>99.99 percent). Accordingly, the self-generation nucleus became larger and single crystallization easier, as shown in Figure 1 [not reproduced]. In addition, crystalline grains located at the center grew toward the surface of the crystalline bar. As a result, single crystallization took place in the entire crystalline bar.[3]

Furthermore, because of high purity, the problems occurring during growing were solved, and growing under a wide range of conditions became possible. Therefore, the influence of the growing conditions on crystallization could be investigated, and the growing of a better quality crystal became possible. Figure 2 [not reproduced] shows a large single crystal that was grown as a result of this study.[5]

References

1.   Y. Ishizawa, et al., J DE PHYS., Vol C6, 1987, p 9.

2.   S. Otani, et al., J. CRYSTAL GROWTH, Vol 61, 1983, p 1.

3.   Ibid., Vol 83, 1987, p 481.

4.   Ibid., Vol 87, 1988, p 175.

5.   Ibid., (in press).

Corrosion of SiC in Potassium Added COM Combustion Gas Plasma

43067612 Tokyo NIPPON SERAMIKKUSU KYOKAI KANTO SHIBU KENKYU HAPPYOKAI in Japanese 4-5 Aug 88 p 20

[Article by Takayasu Okuno, Electrotechnical Laboratory]

[Text] 1. Introduction

For open cycle MHD electric power generation, combustion gas to which potassium has been added in order to accelerate the electrolytic dissociation is mainly used as an operating fluid at 2,500~3,000 K. The combustion gas is mainly generated by the combustion of fine carbon powder with preheated air. It is passed into an electric power generation channel at a high speed, and MHD electric power generation is carried out through the interaction with a strong magnetic field. Insulation walls and electrodes comprising an electric power generation channel are exposed to corrosive environments, such as coal slag, potassium and sulfur, and also to high heat flux and electric current.

The author observed SiC ceramics possessing excellent high thermal conductivity, shock resistance, and the metallizing properties needed for the cooling mechanism equipment, and investigated experimentally the possibility of a high heat flux wall[1] and its corrosion resistance. Tests for the limits of heat flux, corrosion resistance, and thermal impact resistance were carried out. At the same time, evaluations[2] of the characteristics of electric power generation by an electric power generation channel were also conducted, and the compatibility conditions were studied.

Experiment and Results

The cooling structure of the SiC element used in this experiment and its dimensional specifications are shown in Figure 1. The common surface temperatures were limited to within the temperature region where no chemical interaction occurred among products generated by coal combustion upon the addition of potassium, e.g., potassium carbonate, potassium sulfate, and coal slag. There were also limitations in the permissible temperature of a tin contact layer and in the number of thermal impacts. The conditions of the heat flux, corrosion by a potassium thermal water solution, cooling materials, the structure of the cooling waterway, the size of an element, etc., influence the damage and deterioration of an SiC element. In order to grasp the primary causes for such damage and deterioration and also to determine the design factors for a highly reliable element, its fracture mechanism was multilaterally investigated by using the thermal input 1.5 MW COM combustion impact jet flow material experiment device. As a result, under the conditions of combustion gas to which coal (COM) combustion fuel reducing potassium had been added assumed to be the combustion gas plasma conditions of a MHD electric generator, the application limits for a relatively large SiC element 35 mm square and 10 mm thick were experimentally explored as a maximum surface temperature of about 700°C and a maximum heat flux of about 400 W/cm^2. These conditional limits are worthy of attention when compared to those of a conventional MgO insulation wall.[3]
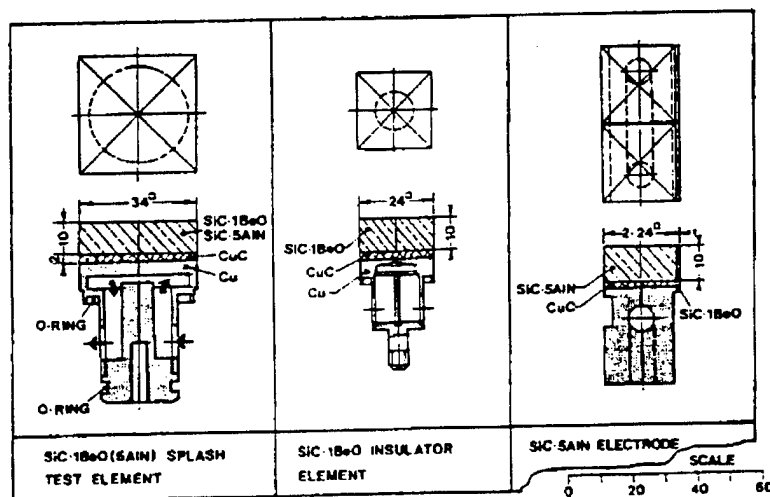
Figure 1. Cooling Structure of SiC Element Used for Evaluation
(Left): Impact jet flow experiment
(Middle): Electric power generation insulation wall
(Right): Element for an electrode

Table 1.   Conditions of Elements After Impact Jet Flow Experiment
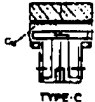
RUN & DURATION	FUEL	ELEMENT	TEST	T_w (°C)	Φ (W/cm²)	EYE	MICROSCOPIC & SEM	EPMA	NOTE
H©60 385MIN	OIL	34x34 D-TYPE SiC-BeO	POTASSIUM ATTACK	980	270	▲1	▲2	▲3	OIL=DIESEL OIL. COM=15=15 HORONAI COAL+OIL. COM-S=COM+C₂H₄S₂.
H©66 395MIN	COM	34x34 B-TYPE SiC-BeO	SLAG ATTACK	735	207	○	○	○	○=STABLE. △=ELEMENT MIGRATION. ▲=DRASTIC DAMAGE.
H©67 340MIN	OIL	34x34 B-TYPE SiC-BeO	POTASSIUM ATTACK	750	218	○	○	△4	ELEMENT DESIGN
H©119 108MIN	COM-S	34x34 C-TYPE SiC-BeO	SULPHUR ATTACK	400	300	○	○	△5	
H©120 108MIN	COM-S	34x34 C-TYPE SiC-BeO	SULPHUR ATTACK	680	180	○	○	△6	
H©126 120MIN	COM	34x34 C-TYPE SiC-AlN	CATHODE ELECTRODE	230	170	○	○	○	

COMMENTS : 1) DRASTIC DAMAGE BY EROSION. CRACKING AND ABLATION.
2) CHANGE OF CRYSTAL STRUCTURE.
3) EXISTENCE OF CARBON-RICH LAYER(~5µm)IN SURFACE REGION.
4) CARBON LOSS AND SiO₂ FORMATION IN SURFACE REGION
5. 6) EXISTENCE OF CARBON-RICH LAYER(10~15µm)AND PENETRATION OF POTASSIUM & SULPHUR.

Table 2.   Conditions of Elements After Durability Experiment by Electric Power Generation Channel

RUN & DURATION	FUEL	ELEMENT (STATION)	T_w (°C)	Φ (W/cm²)	EYE	MICROSCOPIC & SEM	EPMA	NOTE
RUN 75 70.5 HR	COM	INSULATOR (UA-17) 24x24 SiC-BeO	300	130	○	○	△	COM=30wt% HORONAI COAL+OIL
		INSULATOR (BA-17) 24x24 SiC-BeO	300	130	○	○	○	○=STABLE. △=EXISTENCE OF CARBON-RICH LAYER(10~15µm) IN SURFACE REGION & PENETRATION OF POTASSIUM.
		INTERELECTRODE OF ANODE(W-4) 24x24 SiC-BeO	300	130	○	○	○	
		CATHODE (CE-3) 24x24 SiC-AlN	>300	>130	○	○	△	ELEMENT DESIGN SEE-FIG.1
		CATHODE (CE-10) 24x24 SiC-AlN	<300	<130	○	○	○	

Tables 1 and 2 summarize the visual, SEM, mineral microscopic and EPMA observations of the insulation walls and SiC elements used for electrodes. There is no change in the crystalline structure of SiC (SC101) under a high heat flux. However, in the case of potassium and sulfur, penetration and dispersion occur even at low temperatures. When the reduction temperature exceeds 700°C, a reaction with potassium becomes dominant, and the SiC weight loss increases drastically.

46

References

1. T. Okuno, et al., HIGH TEMPERATURE TECH., Vol 11 No 5, 1985.

2. Ibid., Vol 12, No 5, 1986.

3. Ibid., Vol 3, No 2, 1985.

Measuring Young's Modulus of CVD-SiD Thin Film

[Article by Yotaro Matsuo, Atsushi Kimura, Kyoshi Satoh, Koichi Yasuda, and Shushichi Kimura, Tokyo Institute of Technology]

[Text] 1. Introduction

The vibration lead method is one used to investigate the elastic properties of a ceramic thin film. These methods involve problems, e.g., a thin film should be extracted as a single film. In this study, however, the Young's modulus of a thin film has been measured with an ultrasonic microscope. The validity of this method was studied using test specimens of different SiC thin films fabricated by the heat CVD method.

2. Experimental Procedures

Using raw gas composed of CH_4 + $SiCl_4$ + H_2, a SiC thin film was manufactured on a graphite base board by the heat CVD method. Its separating conditions are shown in Table 1. The reaction temperature selected was 1,300~1,450°C, and the pressure in a reactor was 20 torr. Mirror polishing using a diamond paste was applied to the thin film manufactured, and a test specimen was prepared. The film thickness of the test specimen was about 20 μm. A surface elastic wave velocity was measured by the Hitachi ultrasonic microscope (HSAM-1000S Model), and then the Young's modulus was obtained. For purposes of comparison, the Young's modulus was also measured by the vibration lead method.

Table 1. CVD Conditions

Graphite base	
Reaction temperature	1,300~1,450°C
Pressure of reactor	20 torr
Reaction time	120 minutes
The amount of flowing reaction gas	
H_2	170, 420 sccm
Ch_4, $SiCl_4$	40 sccm

3. Results and Conclusion

Figure 1 [not reproduced] shows a photograph taken by SEM of the surface of the film separated under a reaction temperature of 1,350°C, 40 sccm of flowing CH_4 and $SiCl_4$, and 170 sccm of flowing H_2. A cone structure was observed in the film at the low temperature side, but a change in the structure of the square-shaped grains occurred at the high temperature side. From X-ray diffraction, it was confirmed that no peaks occurred except for SiC, and the primary spectrum was β-SiC. The apparent density was in the range of 3.14~3.18 g/cm^3. Pores were observed in the film manufactured at 1,450°C. The Young's modulus of these films is shown in Figure 2. The values measured by the ultrasonic microscope were 450~460 GPa for test specimens with H_2 of 170 sccm. A difference in the reaction temperature was not observed. The Young's modulus measured by the vibration lead methods varied widely, and the measurement of a 20 μm-thick film was difficult under this method. On the other hand, measurement errors by the ultrasonic microscope were only ±7 GPa, and these errors remained when the reaction conditions changed. As seen from the above, it can be concluded that the ultrasonic microscope method is effective for the relative evaluation of the Young's modulus, but not for the absolute evaluation.
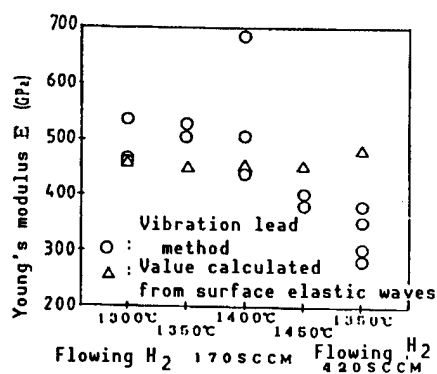
Figure 2. Young's Modulus and Separation Conditions

Application of Random Crack Model to Multiaxial Fracture

[Article by Akira Okada, Central Engineering Laboratories, Nissan Motor Co., Ltd.]

[Text] 1. Introduction

Under multiaxial stress with a dominant tensile stress, the fracture behavior of ceramics can reflect the criteria of mixed mode fracture and the

crack distribution. In this study, the calculation of fracture strength was pursued by studying how the effect of compression stress to a K_{II} mode fracture could be related to the decrease of local K_{II} through the friction force between crack surfaces.

2. Mixed Mode Fracture Criteria

The recent data involving the introduction of sharp cracks into ceramics by mixed mode fracture exhibits a generally higher ratio of K_{IIC}/K_{IC} than that estimated by the conventional criteria based upon stress and energy at the crack tips. It seems to be essentially difficult for the conventional criteria to estimate the effect of compression stress for $K_I < 0$. In the region of $K_I < 0$, local K_{IIC} is the fracture condition. If a negative K_I reduces the effective K_{II} through the friction force between crack surfaces, the criteria can be expressed as

$$K_{II} + \mu K_I > K_{IIC} \tag{1}$$

In addition, the appropriate criteria, including those for the region of $K_I > 0$, were assumed to be expressed by Equation (2), and they were examined.

$$K_I/K_{IC} + (K_{II}/K_{IIC})^2 = 1 \tag{2}$$

3. Calculation of Multiaxial Stresses

If the probability density function of cracks is $f(a)$, the probability of fracture P_F that includes N cracks can be written as

$$P_F = 1 - (1 - F)^N \tag{3}$$

$$F = \frac{2}{\pi} \int_0^{\frac{\pi}{2}} \int_{a_c}^{\infty} f(a) \, d\,a\,d\,\theta \tag{4}$$

where a_c is the minimum size of a crack propagating among cracks inclined at an angle of θ from the principal stress, and which is calculated from the loaded stress and the mixed mode fracture criteria. By considering the fact that the fracture strength distribution can be expressed by the Weifull distribution, the calculation of multiaxial stresses was carried out by using the following probability density function $f(a)$.

$$f(a) = (n-1)/B \times (1 + a/B)^{-n} \tag{5}$$

Figure 1 shows the calculation result of multiaxial stresses. For $K_{IIC}/K_{iC} = 1$, due to the compression stress load, tensile strength gradually decreased. When K_{IIC}/K_{IC} became 2, a compression stress of up to three times larger than the tensile strength did not cause a reduction of the tensile strength.

σ₂ (MPa) axis left graph; σ₁ (MPa) axis; labels μ=0, μ=0.5, μ=1.
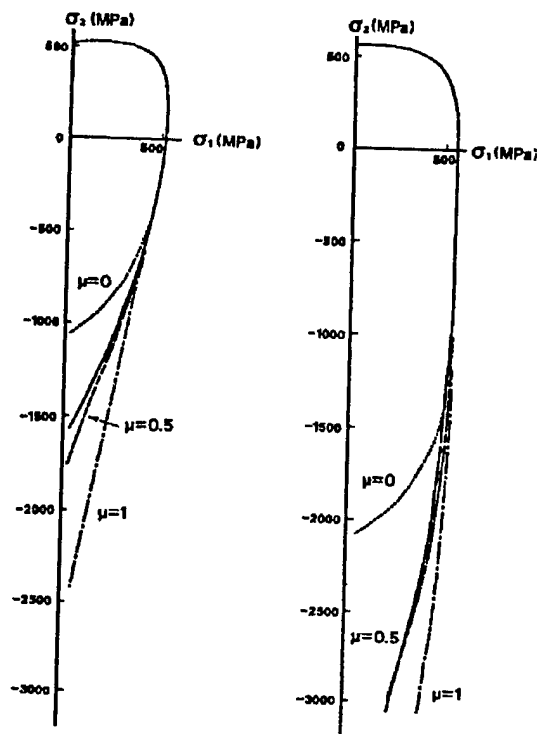
(a) $K_{IIc}/K_{Ic}=1$ (b) $K_{IIc}/K_{Ic}=2$

Figure 1.   Calculation Example of Multiaxial Stress Fracture Strength
         If $K_I > 0$, criteria of Equation (2) is used, in the region of
         $K_I < 0$, Equations (1) and (2) are both used.   ($K_{IC} = 6$ MPa,
         $Y = 1.2$, $n = 20$, $B = 400$ μm).

Development of Structural Analysis Method by Ultrafine Single Crystal

[Article by Kenji Ogitan, Tsukuba University, Kazumasa Osumi, National Laboratory for Energy Physics, and Masaaki Omasa, Tsukuba University]

[Text]   The size of a single crystal currently used for crystalline structural analysis must exceed several tens of microns in diameter. However, test specimens made from materials existing naturally or synthesized are sometimes smaller than this.   The structural analysis of such materials is mostly done by the powder method. Since three-dimensional information is often lost when the powder method is used, the structural analysis of some materials is not carried out.   Therefore, the development of a structural analysis technique for an ultrafine single crystal of less than the several microns is very important.

The size limitations of the test specimen used in the single crystal method is determined by whether or not a signal (diffraction intensity) is

separated from noise (background: BG) with sufficient accuracy. From this, the incident X-ray must be strong in order to assure sufficient diffraction intensity, and should have strong parallelism in order to prevent excessive dispersion that could become BG. As an X-ray resource satisfying the above conditions, a radiation ray was throttled so as to become 50 x 50 μm, and was actually used. When an incident X-ray is throttled extensively, the danger exists of its jumping out of the test specimen from the X-ray flux in the case of a four-axis-type diffractometer that measures a crystal, allowing it to move freely. Therefore, in this study, the Laue method, with only a few movable parts, was employed. It is possible to measure many diffraction intensities simultaneously with this method when an imaging plate (made by Fuji Film) is used in a detector. At the same time, this method is advantageous in terms of saving experimental time. Under the conventional method, a crystal is moved to the diffraction location whenever necessary, and the measurement of diffraction intensity takes place.

The experimental device used in this study enables the vacuum stage of 10^{-7} torr to be obtained in order to eliminate dispersion caused by air. In addition, in order to reduce BG, a collimator has been designed to be as long and slender as possible. There are three axes (ω, X, Φ), aiming at the free fixation of crystalline directions. The Laue image of a molybdenum single crystal of 0.8 μm can currently be obtained by using this device (Figure 1 [not reproduced]).

Observed structural factors with indices are necessary for structural analysis. Accordingly, the index of each Laue spot must be selected, and the diffraction strength of the zones that are overlapped with respect to one Laue spot should be analyzed. The program to select the indices has already been developed, while the program to analyze diffraction intensity is currently under development.

Modulation Structure of Alumina

43067612 Tokyo NIPPON SERAMIKKUSU KYOKAI KANTO SHIBU KENKYU HAPPYOKAI in Japanese 4-5 Aug 88 p 24

[Article by Kenji Ogitani and Masaaki Omasa, Tsukuba University]

[Text] α-alumina has been very widely utilized in the past, and extensive studies have been conducted. The heating and dehydration of α-AlOOH (diaspore) is one method used to produce α-alumina. Lima-de-Faria (1963)[1] found the occurrence of the same phenomenon during the generation of α-Al$_2$O$_3$, possessing a structure similar to that of α-AlOOH, to be analogous to the detection of satellitic reflections upon the X-ray deflection of α-Fe$_2$O$_3$ produced by heating and dehydrating αFeOOH. He inferred this from the density fluctuation of Fe or Al along the c-axis of a product. On the other hand, Watari, et al., (1979)[2] studied an Fe system and, through electron microscopic observation, opposed Lima-de-Faria's hypothesis for the cause of satellite reflection. Instead, they reported that there was no density fluctuation, and satellite reflection was caused by the periodic arrangement of fine voids migrating in a perfect α-alumina crystal. In this study, from the studies of an Al system, it was confirmed that satellitic

reflection is due to periodic density fluctuation, and the amplitude of density fluctuation and average density have been obtained. In addition, the shape of the satellite reflection and the location of the maximum have been found to be dependent upon the heating time. The results will be discussed in this report.

Starting test samples were made from natural materials. The X-ray diffraction method was used for the heating change, and the test sample rapid cooling method and on-the-spot observation method were also applied. As sources of X-rays, an X-ray generation device available on the market and the High Energy Physics Research Laboratory's orbit radiation ray were used. Measurement was done by photographs and a countertube.

The difference in the two hypotheses for satellite reflection originates from the ratio of Al to 0 being 2:3 or less. This difference can be explained by analyzing the average structure for primary reflection only. In this study, the average structure of rapidly cooled test specimens (after being heated for 30 minutes at 500°C, they were suddenly cooled in the air) was analyzed. As a result, the ratio of Al to 0 was found to be 1.5:3. This figure indicates that the density of Al in the test specimen is 25 percent less than that of a perfect crystal. Therefore, the cause of satellitic reflection is the periodic fluctuation of the Al density in a crystal. Subsequently, from the satellite reflection and strength ratio with respect to primary reflection, the configuration and amplitude of fluctuation were obtained. It was found that the density changed almost sinusoidally along the c-axis, and its amplitude was 0.5 (= 25 percent). In the crystalline structure of α-alumina, two-thirds of all octahedral positions is occupied by Al. In other cases, only one-third of the octahedral positions is occupied by Al.

From the rapid cooling and on-the-spot observation methods, it was found that as the heating time increased the satellite reflection became more loosely dispersed, with the maximum location approaching the primary reflection. α-alumina has the densest oxygen package plane perpendicular to the c-axis. It can be recognized as a stratified structure. The analysis of the change of the satellite reflection was then treated in a manner similar to that used for stacking irregularities seen in stratified structures. A general stratified irregularity was studied for uniform chemical composition. As for the test specimens handled by this study, however, as the heating time increased, the satellite reflection was finally absorbed by the principal reflection, and they became perfect α-alumina in terms of composition. The analysis in this study was conducted by taking this fact into consideration.

References

1.   J. Lima-de-Faria, Z. KRISTALLOGR, Vol 199, 1963, p 176.

2.   F. Watari, et al., J. SOLID STATE CHEM., Vol 29, 1979, p 417.

Change in Vickers Indented Area of Partially Stable Zirconia

[Article by Atsushi Saeki, Tadayasu Mizutani, Seki Kato, and Nobuo Ishizawa, Tokyo Institute of Technology]

[Text] 1. Introduction

One mechanism to increase the toughness of partially stable zirconia (PSZ) is stress induction transformation. Defining the extent of a transformation field generated by impressed stress is very important when studying material toughness and the nature of transformation. In this study, the Vickers indentation tip was indented into a Y-PSZ crystal, and the configuration of the change in the structure of the indented area was investigated by SEM.

2. Experimental Procedures

A 2.3 mol percent Y_2O_3-ZrO_2 crystal grown in the [100] direction by the arc image FZ method was used. The test specimen was prepared as follows: The (100) plane perpendicular to the growing direction was cut out, and it was polished by diamond discs Nos 600 and 3000. The Vickers indentation tip was indented into the test specimen with a crosshead velocity of 0.5 mm/min and a load of 50 N, and the tip was held there for 30 seconds. Then, the load was removed. After etching by thermal phosphoric acid, the composition of the indented area was observed by SEM.

3. Results

Figures 1 and 2 [not reproduced] show the separating phase around the indented area. Figure 1 shows the case in which the diagonal line of the indentation corresponds to the [010] direction of the crystal lattice, while Figure 2 shows that when the angle is rotated by 45 degrees. Figure 3 [not reproduced] shows the magnification of the region around the indented area. From this figure, the bright portions observed in Figures 1 and 2 are found to be composed of parallel needles, about 0.17 μm in width and 2~3 μm in length, that appear in the complex-shaped tetragonal separation phase with a width of about 0.6 μm. This needle structure almost disappeared in the test specimen annealed for 24 hours at 1,800°C after indentation. The TEM observation of this area indicated that the structure of the indented area was different from that of the unindented area, and the diffraction images of many monoclinic crystals were recognized. Accordingly, the structure of the indented area is believed to correspond to a monoclinic crystal generated by stress induction transformation. The distribution region of the needle structure changes continuously depending upon the direction of the indenting tip. Although cubic and tetragonal crystals coexist, the slip system does not change very much because the directions of the axes become equal and the axis ratios do not differ from each other. In Figures 1 and 2, a typical slip surface is the <011> direction on the (100) plane parallel to the surface. When the direction in which stress caused by an indentation tip coincides with that of the slip system, the occurrence of the needle

structure is restrained at the center of the indented area since slipping is dominant. The needle structure appears in boundaries in which slipping occurs due to shear force. For the case shown in Figure 2, in which the angle is rotated by 45 degrees, a large number of slips did not occur and dislocation became dominant. Therefore, the appearance of the needle structure is extreme at the center of the indented area.

Fine Structure of Bi System Superconductive Ceramics

43067612 Tokyo NIPPON SERAMIKKUSU KYOKAI KANTO SHIBU KENKYU HAPPYOKAI in Japanese 4-5 Aug 88 p 27

[Article by Yoshio Bando, Tsuyoshi Kijima, Yoshizo Kitami, and Masato Yokoyama, NIRIM]

[Text] It is known that Bi system superconductive ceramics have three different phases corresponding to the critical temperature (Tc) of 105, 75, and 20 K, respectively. The crystalline structure and chemical composition of superconductive phases with critical temperatures of 75 and 20 K were investigated in this study with an analytical electron microscope.

Figure 1 [not reproduced] shows the HREM image of the (110) plane of the 75 K phase. From electron diffraction the crystal is the rhombic system of $a = \sqrt{2Ap} \cong 0.54$, $b = n \times \sqrt{2}$ Ap ($n = 4.8$), and $c = 3.06$ nm. In the direction of the b-axis, a noninteger superlattice of $n = 4.8$ times is formed. According to EDS analysis, its composition is $Bi_{1.9}(Ca_{1.0}Sr_{1.5})Cu_2Oy$. From Figure 1 [not reproduced], it is estimated to be a structure sandwiching five (Ca,Sr)O and CuO_2 layers among Bi_2O_2 layers. Figure 2 [not reproduced] shows the HREM image of the (*100) plane. Bi and Cu ion is deformed in the directions of the b and c axes by the amount of an atom. As a result, a superlattice of a different domain size is formed.

On the other hand, the 20 K phase forms a superlattice of $n = 4.3$ times, and its composition is $Bi_2(Sr_{1.5}La_{0.2})Cu_1Oy$. Similar to Figure 1, the structure has been found to have a laminated structure composed of three layers of (Sr,La)O and CuO_2 layers among the Bi_2O_2 layers. The domain size of this superlattice is different from that of the 75 K phase. However, the HREM image of the superlattice is completely identical to that shown in Figure 2 [not reproduced].

The superlattice period n varies with the ion radius of the Perovskite layer (Table 1). As the ion radius increases, i.e., $Ca^{2+}(0.99$ Å$) \rightarrow Sr_2^+(1.16$ Å$) \rightarrow La^{3+}(1.18$ Å$) \rightarrow Ba_2^+(1.36$ Å$)$, the value of n decreases.

The superlattice image seen in Figure 2 is also observed in the semiconductor phase ($Bi_2Sr_{0.9}La_{0.5}Cu_1Oy$, $Bi_2(La,Ba)_{2-x}Cu_1Oy$). From this fact, it is thought that the origin of the superlattice is not directly related to the nature of superconductivity.

Table 1. Superlattice Period n and Types of Ions

Chemical composition	n
$Bi_2(Ca,Sr)_{3-x}Cu_2Oy$	~ 4.8
$Bi_2(La,Sr)_{2-x}Cu_1Oy$	~ 4.3
$Bi_2(La,Ba)_{2-x}Cu_1Oy$	~ 3.8

Crystalline Chemistry of Bi Superconductive Materials

[Article by Shigeo Sueno, Izumi Nakai, and Noboru Ono, Tsukuba University and NIRIM]

[Text] Recently a superconductive phenomenon was found in Bi-Sr-Ca-Cu-O chemical compounds at temperatures of more than 105 K. The superconductive phenomenon is currently seen in three different materials of the Bi-Sr-Ca-Cu-O system. They are: 1) $Bi_2(Sr,Ca)_2CuO_x$ (abbreviated number: 221); 2) $Bi_2(Sr,Ca)_3Cu_2O_x$ (232); and 3) $Ba_2(Sr,Ca)_4Cu_3O_x$ (243). Although these materials have laminated structures, the configuration of each layer is different from that of the others, and the length of each c-axis is different, i.e., 24A, 30A, and 37A, respectively. The critical temperatures Rc of the pellets containing these materials have been reported to be 8 K, 85 K, and 106 K, respectively. However, the system containing these materials is a multiphase system, and there is no apparent evidence for which of the materials mentioned above is certainly a superconductive material. All these materials have a modulating structure, and their satellite diffraction point is located at 20 Å from the crystalline lattice distance in the direction inclined from the b-axis by 32~39 degrees from the primary diffraction point in the bc plane of a reciprocal lattice.

The authors have studied single crystals with the X-ray diffraction method, and have analyzed the average crystalline structure of the 221 and 232 phase, including anisotropic temperature factors, as the preliminary stage of crystalline structural analysis including the superstructure. The composition and size of the 221 and 232 test samples analyzed are $Bi_2Sr_{1.48}Ca_{0.52}(CuOx$ (0.29 x 0.07 x 0.02 μm) and $Bi_{2.06}Sr_{1.74}Ca_{1.20}Cu_2Ox$ (0.16 x 0.07 x 0.01 μm), respectively. The numbers of the independent diffraction points used for the analysis were 282 and 354, respectively. The results of this study for the 232 phase and those of the past study are compared in Table 1. Namely, the results of diffraction intensity data by single crystal diffraction photographs and a four-axis diffractometer in this study indicated that the space group was Bbmb (Cccm, No 66), and this supported the space group of Du Pont's model. From the analysis that had introduced the anisotropic temperature factors, it was known that thermal vibrations in the bc plane of Bi were large, and a correlation with the modulating structure was also suggested. In addition, along with a crystalline chemical investigation, the coordinate configuration of Bi and oxygen was concluded

Table 1. Specifications of Various Models

	This study	AT&T Bell	Du Pont	Bellcore
Space groups	Bmmb (Cccm)	Fmmm	Amaa (Cccm)	14/mmm
a	5.395(1)	5.414(2)	5.399(2)	3.814(3)
b	5.390(1)	5.418(2)	5.414(1)	(a)
c	30.65(1)	30.89(1)	30.904(16)	30.52(3)
R	0.70	0.173	0.099	0.099
Rw	0.065	0.094	0.088	0.088
Coordination of Bi	6-Coordi.	6 Coordi.	8-Coordi.	6-Coordi.

to be a six configuration of the octahedral model. This supports the Bellcore and AT&T models.

In order to study the annealing effect on the 243 phase, fine single crystals were selected from a test specimen that was heated for 24 hours at 870°C and then identified by X-ray single crystal diffraction photographs. After that, the Meissner effect was measured by the Squid method. The Tc of the quenched 243 phase was found to be 85 K, and the Tc of the annealed test specimen was 106 K (Figure 1). Annealing at relatively low temperatures influenced the Tc. The volume ratio of the portion in the 243-phase single crystal that showed superconductivity at 105 K was 57 percent. A comparison between the single crystal of the quenched test specimen and that of the annealed test specimen was made by single crystal X-ray photograph observation. However, no differences between them were observed.
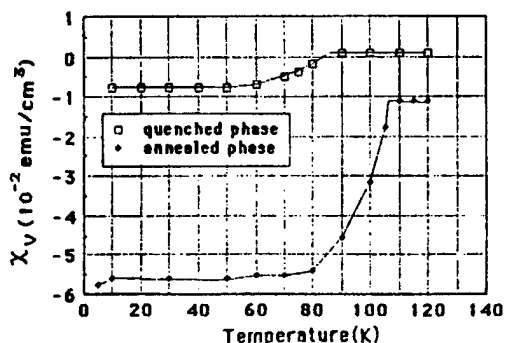
Figure 1. Critical Temperature of Quenched and Annealed Phases

This fact indicates that the increase in the 243-phase Tc may be related to the diffusion or order-disorder of oxygen, and the lamination order may not have an effect. The single crystal X-ray diffraction photographs of the 243 phase are different from those of 221 and 232. Loose dispersion along the c-axis originating from severe lamination defects, and a twin plane containing a loose dispersion on one side and the (110) plane on the other along the c-axis originating from severe lamination defects is always observed. The observation of those dispersion rays indicates the presence

of diffraction density at the position of a reciprocal lattice that corresponds to 232. This could confirm the existence of a similar lamination layer of 232 in 243. However, there is no diffraction density at the position corresponding to 221.

High Resolution Electron Microscope Study of Ceramic Structures

43067612 Tokyo NIPPON SERAMIKKUSU KYOKAI KANTO SHIBU KENKYU HAPPYOKAI in Japanese 4-5 Aug 88 pp 32-36

[Article by Yoichi Ishida, Tokyo University]

[Text] 1. Introduction

Recent studies have pointed to ceramics boundaries as being attractive subjects for a high resolution electron microscope. This is not associated with this instrument's observational technique, such as its relative ease of observation with high resolution due to the large unit structure of ceramics as chemical compounds. Instead, it is because various compositional polytypes exist as the result of the periodic structure disorder, and they exhibit different structures in the ceramics boundaries. For this reason, knowledge of the regular structure proves to be very useful in assuring the interpretation of an image. The ceramics boundaries are providing new theoretical problems. The corresponding lattice theory being developed, which is subject to the crystal boundaries of relatively simple and isotropic structures, is too poor to use to describe the boundary structure of anisotropic crystals. Instead, the nonperiodic low energy boundary theory, to which the subcrystal and the boundary structure theories, combined with an approximate corresponding lattice, are applied, is required. In this report, three examples are selected as representative of the recent study, and the role of the high resolution electron microscope in characterizing ceramics boundaries will be introduced.

2. Observation of Sheet Defect Compound Body of Aluminum Nitride[1,2]

Aluminum nitride is thought to be a promising semiconductor circuit board possessing good heat radiation characteristics. Actually, however, less thermal conductivity than the theoretical value has only been obtained since various lattice defects have migrated in a crystal function as the diffusion center of a phonon. Although a crystalline grain boundary is problematical, only the results of the transcrystalline plane defects analysis conducted by a high resolution electron microscope are discussed in this report.

The test specimen was hot press AlN provided by Toshiba Corp. It was sintered for 1 hour at 1,973 K under pressure of 22 MPa, and resulted in a black polycrystal. Machine polishing using a diamond grindstone was employed, and a thin plate was made. Then, ion polishing with 4.5 KeV[+] was applied.

Photograph 1(a) [not reproduced] is an example of the lattice defect structure observed inside the 2H-AlN crystal. At first glance it calls to mind a mixture of a sailboat and a UFO (unidentified flying object). This

57

picture received a prize in the photography contest sponsored by the Metal Society of Japan last year (1987). The sailboat-like appearance seems to be complicated, but it is composed of lamination defect boundaries parallel to the bottom plane (0001) of 2H-AlN and the hemisphere-shaped curved surfaces. This means that when sailboat-like shape was small, it had the UFO shape. As it grew, it became a plane defect complex, which then united. Relative to the internal and external crystal directions of this defect structure, no matter how the test specimen was inclined and diffraction conditions were altered, the conditions for the diffraction solely of the interior were not found. Deviation only occurred in the position of the crystal lattice points at the simplest boundaries of both sides, while the directional relationship of the boundary remained the same. This boundary is generally called a lamination effect. The analysis of this boundary is discussed first.

Photograph 1(b) [not reproduced] shows high resolution observation of a plane defect complex. It magnifies the lower right joining portion of the UFO-shape in Photograph 1(a). Among the defects, the cross section of the one parallel to the base is seen. On the other hand, since the hemisphere-shaped boundaries are curved surfaces, their images overlap. Accordingly, lattice images are observed that are curved or distorted.

The study of boundaries parallel to the base has been conducted sufficiently in the past as part of the subject of compositional lamination irregularities. In this system, lamination irregularities caused by the main impurities, such as oxygen, are well known. In either case, alumina of a sphalerite structure lines up every several layers by comprising one atom layer in the direction parallel to the AlN base (Figure 1). On the other hand, in the case of the boundary in which a specific plane does not have a low energy state, a cross section cannot be observed. However, since a curved surface is a special case, it is possible to attain a rough estimate. Figure 2 shows such a case. A lamination difference in every two atomic planes (ABAB ••• ACAC), that is peculiar to other 2H-wurtzite structure, is the true nature of this boundary, and it does not have a strain field over a wide area. On the boundary, an atomic site is estimated to occupy a vacant space. Accordingly, this plane defect complex can be interpreted so that separating a supersaturated atomic vacant space under decreasing temperatures becomes an isotropic large shape due to the 2H-wurtzite structure of the AlN. From the effect of impure atoms on the growth of the plane defect complex, it can be concluded that impurities such as oxygen, silicon, and iron are segregated, and they participate in the formation of a nucleus. For the dispersion center of a phonon, how strong the plane lattice defect is, including these impure elements, and how it decreases thermal conductivity are the problems to be solved in the future. Nevertheless, even the low density plane defect may provide a great influence.

3. Observation of Polytype Twin Crystal Boundary of Silicon Carbide[3,4]

Both silicon carbide and silicon nitride are highly regarded as the materials of honing. However, a sintering assistant agent added during sintering remains in a crystal boundary as a thick crystal grain boundary
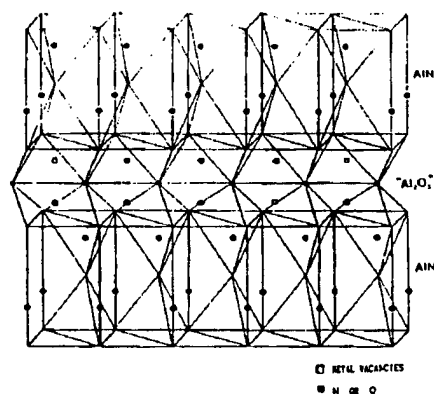
Figure 1. Structural Model of Lamination Irregular
Boundary Parallel to the Base
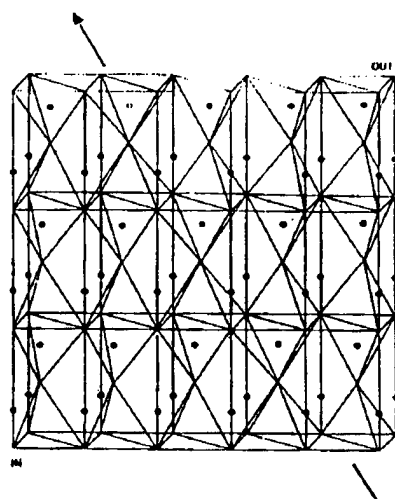
Figure 2. Structural Model of a Curved Surface

layer. This reduces the strength at high temperatures. In this study, the possibility of generating the crystal boundary of highly pure silicon carbide without employing a sintering assistant agent was investigated. At the same time, an investigation was also made of the structural characteristics of the crystal grain boundary of silicon carbide.

The test specimen used was SiC of high purity made by the sublimation vaporization method in the Inorganic Material Laboratory. When this material was gradually cooled from 2,800°C, it became a sheet-shaped crystal with a length of 2~3 mm and a thickness of 200 μm. A large portion of the crystals created with single crystals, but twin crystals were also created. The twin crystals were selected by cutting them out in the direction perpendicular to the grain boundaries, and were polished by a machine. As a result, a thin plate was obtained. Ion polishing by Ar$^+$ with an intensity of 3 KeV was applied, and observations were made.

Photograph 2 [not reproduced] is an example of the high resolution observation of twin crystal grain boundaries. Although the crystals in both sides show a layer structure, one is a folding-back structure with twin crystals at every third atomic plane, and the other structure has twin crystals in every atomic plane and second atomic lane (Figure 3). There is almost no difference between the two boundary phases. However, the kind of polytype is different, i.e., the right is 6H and the left is 15R. In the strict sense of the word, it is a heterogeneous boundary. In this boundary, the roof-shaped single crystal of three atomic layers on the right and two atomic layers on the left is piled up alternately, and two sheets of single crystals composed of three atomic layers are also stacked. Two sheets of single crystals have an arrangement corresponding to the unit structure of the Σ9 corresponding grain boundary.
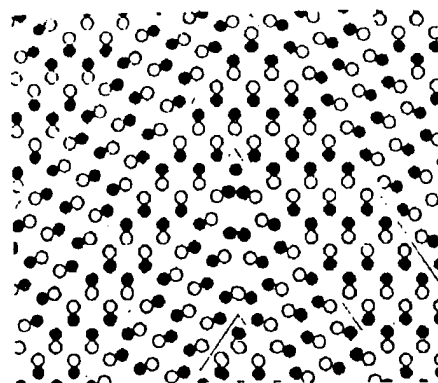
Figure 3. Polytype-Structured 6H/15R Boundary

The lattice image shown in Photograph 3 [not reproduced] can be interpreted as the center position, or bright point, of a six-ring basic diamond structure. Since no difference is seen between the silicon and carbon atoms that constitute a six-ring, the atomic arrangement of the Σ9 corresponding lattice unit structure cannot be determined. In Figure 3, in order to distinguish a difference in height in the [1100] direction, a six-ring is indicated by black and white circles. For the corresponding lattice made by the user position of both 6H and 15R translation lattices, its unit lattice becomes huge. However, it performs the primary duties as a corresponding lattice in the sense of prescribing the periodic structure of the twin crystal grain boundary. However, the lamination layer described above indicates that the selection of the polytype itself is closely related to the direction of the grain boundary. There is a demand for the corresponding lattice theory, including the polytype, to be constructed. Photograph 3 [not reproduced] shows an example of an asymmetrical inclined grain boundary. Both sides of the boundary are of the 6H type, and the roof-shaped single crystal does not cross the grain boundary at every three atomic planes. The twin crystal in which every three atomic planes is the basis for the 6H structure is shown to be an arrangement involving lower energy than that of a matrix. Therefore, this grain boundary consists of three-atom units, and the three-atom unit of the twin crystal and that of the Σ9 corresponding grain boundary are alternately repeated. Figure 4, showing the superposition of 6H translation lattices, indicates that this

60

grain boundary is the plane with the highest corresponding lattice density. the wide application of the corresponding lattice theory can be impressed. A high resolution electron microscope is suitable for analyzing the structure of the boundary in which an atomic arrangement is restricted by
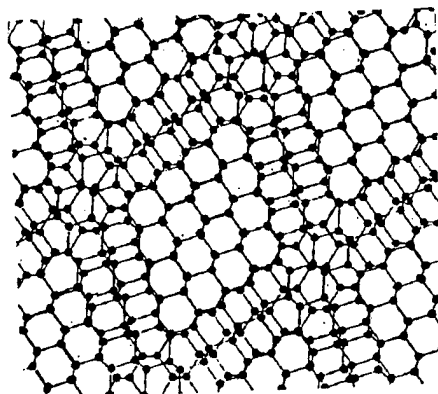
Figure 4. Structure of Epi-Grain Boundary

the surrounding adjusted twin crystals. However, due to the difficulties encountered in preparing the test specimens, the expected results have not yet been obtained.

4. Observation of Perovskite-Type Superconductive Sintered Crystal Boundary[5,6]

In Perovskite high thermal conductive oxides, such as yttrium and bismuth systems, a crystal grain boundary grows in the direction parallel to the base (c-plane) of a crystal due to the effect of its layer structure. The average coherence length of Cooper pairs strongly related to superconductivity is on the order of several nm. Its length is particularly short in the direction of the c-axis. Therefore, it is presumed that the structure and conductivity of the grain boundary in the c-plane are closely related to other electric properties of this material.

The test specimen was made from a mixture of the oxide or carbonate of the yttrium system $YBA_2Cu_3O_{7-x}$ (YBCO) and bismuth system Bi-Sr-Ca-Cu-O (BSCCO) by using the solid-phase reaction method. A bulk test specimen was processed by machine and ion polishing, and a thin film was obtained. Then, observation employing electron microscope was carried out.

Photograph 4 [not reproduced] observes the c-plane grain boundary of YBCO. If is known that YBCO is corroded by the moisture or carbonic acid gas contained in the air. This is believed to be the cause of an amorphous layer that is sometimes observed in the c-plane grain boundary. This deterioration problem can be avoided by observing the thin film test specimen immediately. In Photograph 4, since a periodic interval occurs in the direction of the c-axis, the disorder of an arrangement by 1 nm is naturally anticipated in the neighborhood of the grain boundary.

When compared to YBCO, BSCCO is more stable and does not corrode when exposed to the atmosphere. It is suitable for electron microscopic

observation. The modulation structure of bismuth, in which intervals of growing in the direction of the b-axis occur about five times, is unique as the structure of a low temperature phase. There is the tendency for a crystal grain boundary to be parallel to the dense direction (Photograph 5(a) [not reproduced]). Specifically, the Bi_2O_2 layer tended to become the grain boundary plane in the c-plane grain boundary of BSCCO (Photograph 5(b) [not reproduced]). This kind of structure of the grain boundary plane observed in sintered materials may indicate that the corresponding lattice theory developed after the model of cubic metals is not sufficient as the grain boundary structure theory for a crystal that has a layer structure, making it necessary to prepare an epi-boundary structure theory that would include the anisotropy of a crystal. Regarding individual atom arrangements, the crystal theory should be applied instead, and the consideration of the distribution of nonperiodic low energy arrangement units seems to be effective.

The c-plane of these materials is also a cleavage plane. Accordingly, the c-plane grain boundary can break inside the test specimen due to thermal stress. The broken crystal grain boundary is thought to restrict the conductive path and to reduce Jc. This may explain the difference in Jc between a single crystal and a polycrystal. The role of the crystal grain boundary in ceramic superconductive materials is very complicated.

5. Conclusion

1) The lamination effect, that is the simplest of the ceramic boundary structures; 2) a special polytype crystal grain boundary that has a matched twin crystal as its composition element; and 3) the boundary structure of a pyrogenetic superconductor that has been observed as the crystal grain boundary of general sintered ceramic materials, are presented as examples in this report. High resolution electron microscopic analysis enables high level information to be obtained when the regular structure of the boundary is simple and when information regarding the atomic arrangement level is qualitatively and quantitatively sufficient. The first two examples involve this case. Since the unit structure of ceramics is large, it is suitable for lattice image analysis. However, in either case, the identification of an atomic arrangement has not been accomplished. There are consideration drawbacks when comparing this task to the interpretation of a matrix image. One of the reasons for this involves the segregation of a small amount of impurities in the boundary. That is a difficult aspect in regard to boundary structure analysis. The study of a high purity silicon carbide twin crystal is very much expected.

The characteristics of ceramic boundary structures involve a high degree of anisotropy reflecting the layer structure. Therefore, the corresponding lattice grain boundary theory developed, which stresses cubic metals, should be modified substantially. The grain boundary of ceramics constitutes a challenging subject among the grain boundary theories. High resolution electron microscopic observation plays an important role in this subject.

Acknowledgement

Three examples of boundary research presented in this paper were the results of a recent study by S. Ishino, S. Hagege, and H. Takahashi of graduate school. The author would like to express his appreciation to them for the providing the photographs presented in this study. The study shown here involves joint research with another research group. The author also expresses his gratitude to Y. Inomata and Y. Bando of the Inorganic Material Laboratory, T. Tanaka of Toshiba Corp., and K. Naeki, Y. Kitazawa, and K. Kishio of Tokyo Institute of Technology for their help and cooperation.

References

1. S. Hagege, T. Tanaka, and Y. Ishida, 1988 Spring Conference, Ceramics Association.

2. Ibid., in press.

3. H. Ichinose, Y. Inomata, and Y. Ishida, J. OF JAPAN CERAMICS ASSOCIATION, Vol 94 No 4, 1986.

4. Ibid., Proc. California Conference, 1988.

5. Y. Ishida, Y. Takahashi, M. Mori, K. Kishio, K. Kitazawa, K. Fueki, and M. Kawasaki, J. ELECTRON MICROSC., Vol 36 No 4, 1987, p 251.

6. Y. Takahashi and Y. Ishida, Proc. MRS, Ikebukuro, 1988, in press.

Mechanical Properties of Glass Fiber Composites for Biomaterials

[Article by Masahiro Kobayashi, Kenji Date, Hideo Tagai, Masataro Morishita, Masahiro Seyama, and Yoshikatsu Kuroki, Chiba Institute of Technology, and Mikiya Ono and Hiroyasu Takeuchi, Mitsubishi Mining and Cement]

[Text] **1. Purpose**

The mechanical properties of biomaterials for use as artificial bones should have higher mechanical strength and the same modulus of elasticity than those of human bones. Biomaterials of a metal system for supporting organisms presently in use have advantages in strength, toughness, and processibility. However, they also have several drawbacks, e.g., they cannot directly join with organic systems, and the elution of ions, fractures due to fatigue, and an excessive modulus of elasticity and density occur. In this study, glass fibers of the $CaO-Pu_2O_5-SiO_2-Al_2O_3$ system (CPSA fibers), possessing an affinity with organs, were spun, and by using these glass fibers, a glass fiber composite material (CPSA composite material) formed by the polymethyl methacrylate (PMMA) of thermoplastic resin was developed. Then, the biological and mechanical properties of this material were investigated. Although this was a preliminary study, it was confirmed

that this material's properties are preferable to those of conventional materials used for artificial bones. Its mechanical properties will be discussed.

2. Method

The CPSA composite material was formed as follows. CPSA fibers were immersed into a PMMA acetone solution, and after they were dried, they were pulled out through a glass die from a forming reactor to form a one-directional composite material. The measurement of the mechanical properties confirmed with JIS K 6911. Bending, tensile, and compression tests were conducted with the Shimazu Autograph SD-500 C model, and the strength and modulus of elasticity were obtained.

3. Results

The properties of the CPS composite material are as follows:

(1) Cells multiplied in the cell cultivation test, and there was no indication of toxicity. Under the bone structure reaction, a new bone was formed around the material 2 weeks after the beginning of the test. The affinity with organs was good.

(2) Toughness was observed from the bending fracture behavior.

(3) The bending, tensile, and compression strength of the one-directional composite material was approximately three to eight times stronger than that of a human cortex bone.

(4) The modulus of elasticity of the one-directional composite material was almost the same as that of a human cortex bone.

(5) The apparent density of the one-directional composite material was almost the same as that of a human cortex bone.

(6) It is possible to design materials possessing certain mechanical properties by varying the volume ratio of glass fibers, the diameter of the fiber, and the reinforcement configuration.

(7) Secondary processing, such as cutting, is applicable.

From the results shown above, the preliminary biological and mechanical properties of the CPS composite material are thought to be superior to those of the existing biomaterials. However, more studies involving the long-term reaction with the bone structure, joining strength with a bone, the deterioration of strength occurring in an organ, the reinforcement configuration of fibers, designing, etc., are necessary in the future.

Reheating Behavior of Glass Fiber Composites for Biomaterials

[Article by Masahiro Kobayashi and Kenji Date, Chiba Institute of Technology]

[Text] 1. **Purpose**

The material for use in artificial bones formed by a thermoplastic resin-polymethyl methacrylate (PMMA) with glass fibers of the $CaO-P_2O_5-SiO_2-Al_2O_3$ system (CPSA glass fiber) has been developed, and various studies of this material have been conducted. This CPSA composite material has a good affinity for organs. Its modulus of elasticity is similar to that of human cortex bone, and its fracture strength is greater than that of a human cortex bone. Accordingly, it has been reported that this material has desirable mechanical properties as a substitute for organs.

At this time, in order to investigate the material processing method, including the dimensional stability of the CPSA composite material under thermal history after formation, the reheating expansion behavior of a reheating and slow-cooling process and its effect on mechanical properties have been investigated, and the results are discussed.

2. Method

Regarding its reheating expansion behavior, a CPSA glass fiber bundle (fiber diameter to be selected) was immersed into a PMMA acetone solution, and then dried. A bar-shaped unidirectional composite material formed by the drawing method was cut into pieces 20 mm long. They were measured by the TMA apparatus made by Rigaku Denki Corp. at temperatures ranging from room temperature to 180°C. The coefficient of linear expansion was repeatedly measured in the temperature range from room temperature to 100°C. In addition, similar measurements were carried out for a composite material that was reheated at 85°C for 3 hours and then cooled gradually.

The measurement of the mechanical properties of the composite material conformed to JIS K 6911. Bending, compression, and tensile tests were done by the Shimazu Autograph SD-500C model, and the strength and modulus of elasticity were obtained.

3. Results and Conclusion

(1) The heating expansion curve of the CPSA glass expanded almost linearly from room temperature to 700°C, with a Tg of about 780°C, while that of PMMA expanded almost linearly from room temperature to 90°C, with a Tg of about 120°C.

(2) When the heating expansion curve measurement of the CPSA composite material was repeated using the same test specimen, its curve changed from a moderately curved line to a straight line. This could be due to the

relaxation occurring during reheating since the test specimen of the bar-shaped composite material was formed by the drawing method, and residual strains migrated in the PMMA matrix. The coefficient of linear expansion measured at that time was approximately that of the test specimen after reheating and slow-cooling took place.

(3) The relationship between the coefficient of linear expansion and Vf was that as Vf became larger, the coefficient of linear expansion decreased. This value was approximately that of the calculated value of Turner's equation. It was found that the coefficient of linear expansion of a two-layered string material was higher than that of one-directional material.

(4) The compression strength and modulus of elasticity increased slightly when reheating and slow-cooling took place.

From the above results, in order to improve the strength and dimensional stability of the CPSA composite material under thermal history and a secular change, reheating and slow-cooling is thought to be effective to relax the strains generated during forming.

Physical Properties, Fine Structure of Transparent Zirconia Sintered Body

[Article by Yuichi Nagasaki, Koji Tsukuma, and Hiroshi Yamamura, Tosoh]

[Text] 1. Introduction

A sintered body with high optical transparency can be manufactured by adding yttrium and titania to zirconia.[1] The purpose of this study is to investigate the effect of the fine structure of a sintered body on its optical transmissivity and mechanical properties.

2. Experimental Method

Powder composed of $ZrO_2:Y_2O_3:TiO_2 = 82.8:7.2:10$ (mol) was first formed, and was baked at 1,400~1,670°C for 2 hours in the presence of oxygen. HIP processing (150 MPa, 1,500°C, 1 hour, Air) was applied to the sintered body. Then, the sintered body, deoxidized by this processing, was oxidized again by baking at 1,000°C for 2 hours. As a result, an optically transparent zirconia sintered body was obtained. The optical transmissivity of this material was measured and its fine structure was observed.

3. Results and Conclusion

Figure 1 shows the optical transmissivity of the sintered body used in this study in the region of visible rays. The optical transmissivity varied considerably depending upon the baking temperature. When the baking temperature exceeded 1,400°C, the optical transmissivity decreased. It increased again at temperatures over 1,600°C. The sintered body baked at 1,670°C (50~68 percent, thickness: 1.0 mm) showed the highest

transmissivity. On the other hand, the sintered body baked at 1,550°C (3~24 percent) exhibited the lowest figure.
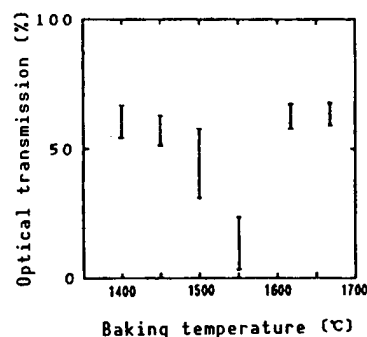
Figure 1. Relationship Between Baking Temperature and Optical Transmission Rate in the Optically Transmittance Zirconia Sintered Body

From X-ray diffraction of the sintered body before the HIP processing, two phases, i.e., a cubic crystal and tetragonal crystal, were found to exist in the sintered body processed under 1,600°C. X-ray diffraction of the sintered body after the HIP processing indicated that no independent peak of the tetragonal crystal occurred in all cases. However, the broad peak of the cubic crystal was observed.

When the sintered body baked at 1,670°C was annealed at 1,400°C, the sintered body disappeared. TEM observation of this sintered body showed the existence of a lens-shaped separating material. Analysis, such as X-ray diffraction, indicated that the separating material was a tetragonal crystal.

According to SEM observation on each sintered body, the grain size increased as the baking temperature increased (Table 1). Not only large grains of 20~60 μm, but also small ones of several μm were observed only in the sintered body baked at 1,550°C. The small grains are thought to be tetragonal crystal.

Table 1. Mechanical Properties and Grain Size of Optically Transparent Zirconia Sintered Body

Baking temper- ature (°C)	HIP temper- ature (°C)	Density (g/cm^2)	3-point bending test (MPa)	Vickers hardness (GPa)	Fracture tough- ness (MPa/m)	Grain size (μm)
1,400	1,500	5.87	230(200-260)	13.1	2.3	10-40
1,450	1,500	5.87	250(200-300)	13.4	2.7	10-40
1,500	1,500	5.87	260(220-290)	13.8	2.5	10-40
1,550	1,500	5.87	210(180-230)	13.3	2.5	20-60
1,620	1,500	5.87	180(170-200)	13.4	2.2	30-130
1,670	1,500	5.87	160(145-190)	12.3	1.9	60-180

The preceding indicates that the existence of a tetragonal crystal seems to greatly influence the optical transmissivity of optically transparent zirconia sintered bodies.

References

1.   J. OF MAT. SCI. LETTERS, Vol 5, 1986, pp 1143-1144.

Thermal, Mechanical Properties of Ceramics With High Thermal Expansion

[Article by Akira Tanaka and Tadahiko Miyoshi, Hitachi, Ltd.]

[Text] 1. Introduction

For a composite structural material composed of ceramics and metallic materials, a problem associated with internal strains and fracture caused by the difference in thermal expansion between these materials will occur. In this study, in order to develop ceramics possessing a coefficient of thermal expansion ($\geq 15 \times 10^{-6}/°C$) equivalent to that of stainless steel and bending strength (≥ 300 MPa) similar to that of alumina, metallic oxide/metallic fluoride composite ceramics have been investigated.

2. Experimental Method

Under a combination of volume ratios between ZrO_2 (Y_2O_3 3 mol percent contained) and CaF_2, fine powder was used to manufacture a sintered body by a hot press with pressure of 30 MPa at 1,300°C. From X-ray diffraction analysis, the composition of powder and a sintered body was investigated. SEM was used to observe the surfaces and fracture. The coefficient of thermal expansion was measured by a differential thermal expansion meter in the temperature range from room temperature to 700°C. Bending strength was measured by the four-point bending method, and the modulus of elasticity and Poisson's ratio were measured by the supersonic pulse method.

3. Experimental Results

Figure 1 shows the relationship between the volume percent ratio and the coefficient of thermal expansion. As the CaF_2 content increases, the coefficient of thermal expansion increases. These experimental results coincide well with the ones calculated theoretically using Turner's equation. X-ray diffraction indicated that there was no secondary product, and composite ceramics were composed of the simple mixture of ZrO_2 and CaF_2. Figure 2 shows the relationship between the volume percent ratio and bending strength observed in composite ceramics. As CaF_2 content increases, bending strength decreases. From Figures 1 and 2, when a volume percent ratio of ZrO_2 (Y_2O_3 3 mol% contained) -CaF_2 composite material becomes 1:1, a composite material possessing a coefficient of thermal expansion ($\geq 15 \times 10^{-6}/°C$) equivalent to that of stainless steel and bending strength (≥ 300 MPa)
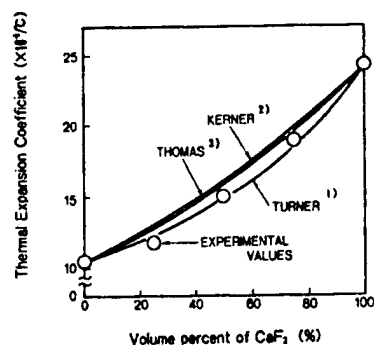
Figure 1. Experimental Results of Thermal Expansion Coefficient
(R.T.~700°C) of ZrO_2 (with 3 mol% Y_2O_3)-CaF_2 Composites
(The coefficients predicted by various equations are also
shown.)
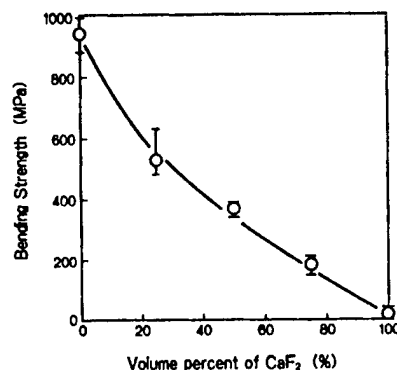
Figure 2. Bending Strength of ZrO_2 (with 3 mol%
Y_2O_3)-CaF_2 Composites

Table 1. Property Data for the Composite ZrO_2 and CaF_2

Materials	Density D (g/cm^2)	Young's modulus E (GPa)	Poisson's ratio ν	Thermal expansion coefficient α ($°C^{-1}$)	Bending strength σ (MPa)
ZrO_2 (with 3mol% Y_2O_3)-CaF_2 composite (50 vol%/50vol%)	4.5	142	0.27	15.0	360
ZrO_2 (with 3mol% Y_2O_3)	5.93	210	0.3	10.5	960
CaF_2	3.16	110	0.28	24.2	35

similar to that of alumina can be obtained. Table 1 shows the properties of the composite material obtained in this study.

References

1.   P.S. Turner, J. RES. NBS, Vol 37, 1946, p 239.

2.   E.H. Kerner, PROC. PHYS. SOC., Vol 69B, 1956, p 808.

3.   J.P. Thomas, AD287-826 (General Dynamics, Fort Worth, Texas).

Mechanical Properties of Si_3N_4 Composite Ceramics

43067612 Tokyo NIPPON SERAMIKKUSU KYOKAI KANTO SHIBU KENKYU HAPPYOKAI in Japanese 4-5 Aug 88 p 41

[Article by Atsushi Nakadaira, Katsuaki Suganuma, Kozo Kojima, and Tsuyoshi Hirano, National Defense Academy, and Hiromasa Isaki and Shigemasa Kawakami, Mitsubishi Gas Chemical]

[Text] 1. Introduction

Si_3N_4 ceramics are expected to exhibit superior mechanical properties, such as strength, toughness, and thermal impact resistance, for engineering use. However, in order to put this material to practical use, it is necessary to improve its characteristics. Studies to improve strength and toughness by compounding second-phase particles and SiC whiskers have been conducted. In this study, Si-C-N composite powder obtained by the CVD method was processed by a hot press, and Si_3N_4/SiC composite material, with high strength of more than 1,000 MPa from room temperature to 1,200°C, was manufactured. Then, the influence of SiC on the mechanical properties of this material was investigated.

2. Method

The Si-C-N composite material was synthesized from ammonia and hexamethyldisilazane by a gas-phase reaction. Several different kinds of powder with various C/N ratios were made by varying the amount of ammonia. They were thermally processed and stabilized in a nitrogen gas environment. Sintering assistant agents, such as 6 wt% Al_2O_3, were added to the powder, and then it was processed by a hot press at 1,800°C for 2 hours under the pressure of 34 MPa in a nitrogen gas environment.

Regarding the mechanical properties, hardness was measured by a high temperature hardness tester in the range from room temperature to 1,150°C, and strength was measured by the three-point bending testing method from room temperature to 1,500°C. Fracture toughness was obtained by the IM method. The fine structure was investigated by a scanning electron microscope (SEM), transmission electron microscope (TEM), and high resolution electron microscope (HREM).

3. Results

Hardness increased monotonously as the volume percent ratio of SiC increased (Figure 1). The strength increased until the volume percent ratio of SiC became 10 percent, while above this figure, the strength remained same. On the other hand, fracture toughness increased along with the increase of the volume percent ratio of SiC up to 10 percent, exhibiting a maximum value of about 7.0 MN/m$^{3/2}$. When a volume percent ratio became more than 10 percent, the fracture toughness deceased, approaching the value of Si$_3$N$_4$ itself.
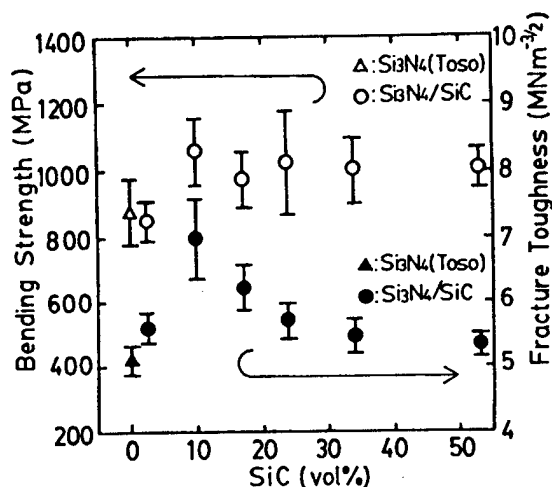
Figure 1.   Effect of SiC Volume Ratio on Strength and
Fracture Toughness

The results of SEM observation indicated that, as the volume percent ratio of SiC increased, the growth of Si$_3$N$_4$ of pillar-shaped particles was accelerated. When this value was around 10 percent, the growth of the pillar-shaped particles reached a maximum. Over 10 percent, the growth of the pillar-shaped particles was restrained while, at the same time, the fine structuralization of the particles started. In addition, it was found from the results of TEM and HREM observations that fine particles of SiC with diameters of several tens of nanometers were dispersed not only in the boundaries of the Si$_3$N$_4$, but also inside the grains. The mechanical properties of the composite material are thought to be related in some way to this fine structure.

Thermal Impact Property of Al_2O_3/Si_3N_4 Composite Material

[Article by Atsushi Nakahira, and Koichi Niihara, National Defense University, and Jun Ogishima and Toshoi Hirai, Tohoku University]

[Text] 1. Introduction

The authors manufactured Al_2O_3 composite materials by adding various kinds of nonoxidized ceramics as the dispersion phase, and confirmed that the addition of nonoxidized ceramics was effective for improving the mechanical properties of Al_2O_3, such as strength and fracture toughness. This paper focuses on the Al_2O_3/Si_3N_4 composite material made from Al_2O_3 compounded with Si_3N_4, and the effect of the addition of Si_3N_4 on the thermal mechanical properties of this material, specifically thermal impact resistance, thermal conductivity, and the coefficient of thermal expansion, will be discussed.

2. Experiment

As the starting material, Al_2O_3 made by the Asahi Kasei Corp. and Si_3N_4 (α coefficient > 95 percent) made by Stark Corp. were used. Si_3N_4 of 0-50 mol% was added to the Al_2O_3, and they were mixed by a ball mill with ethanol. After they were dried and smashed, they were processed by a hot press at 1,500-1,800°C in a nitrogen gas environment. As a result, an Al_2O_3/Si_3N_4 composite material was obtained. Its fracture toughness and strength were evaluated by the IM method and three-point bending testing method, respectively. The modulus of elasticity was measured by the resonance method. The thermal impact test was done by the underwater rapid cooling method. Thermal conductivity was measured by the laser flash method from room temperature to 800°C. The coefficient of thermal expansion was measured by a push-bar type expansion tester. The grain size was determined by SEM observation of a test specimen processed by thermal etching. In addition, SEM and TEM observations of fracture surfaces and the fine structure were carried out.

3. Results

The fine structure, such as the formation phase and the grain size, of the Al_2O_3/Si_3N_4 composite material was greatly influenced by the amount of Si_3N_4 added and the temperature of the hot press. The test specimen processed by a hot press at 1,500°C did not have a fine structure. On the other hand, in the case of the test specimen processed by a hot press at temperatures exceeding 1,700°C, considerable grain growth of the Al_2O_3 matrix (depending upon the manufacturing conditions)--this was an Al_2O_3 + Sialon mixture matrix) occurred. On the other hand, the test specimen processed by a hot press at 1,000°C exhibited a structure in which the secondary phase of investigated Si_3N_4 and Sialon was dispersed into the fine Al_2O_3 matrix. Accordingly, hot pressing at 1,600°C was thought to be the optimum manufacturing condition, and the following thermal mechanical properties were measured.

Figure 1 shows the results of the thermal impact test on the $Al_2O_3/30$ mol% Si_3N_4 composite material, which is a typical test specimen. In this figure the test results of an Al_2O_3 single crystal phase test specimen are also shown. As seen from this figure, the critical temperature difference ΔTc improved by 200°C, while a decrease occurred in the strength of the $Al_2O_3/30$ mol% Si_3N_4 composite material, when compared to that f the Al_2O_3 single phase. This is thought to be due to the increase in fracture toughness and strength and the decrease in the coefficient of thermal expansion and the modulus of elasticity accomplishing the addition of Si_3N_4
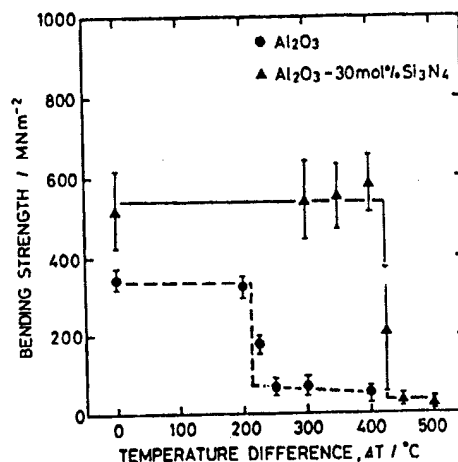
Figure 1. Change in Strength After Quenching in Water

Fatigue Crack Propagation in Silicon Nitride Sintering Body

[Article by Susumu Horibe, NIRIM]

[Text] 1. Introduction

Fatigue damage of ceramic materials under repeated loads has recently become a subject eliciting great concern. Studies associated with this subject have been active. However, due to experimental difficulties related to its brittleness and scattered data, a unified interpretation of this phenomenon has not yet appeared. It seems to be taking a long time to explain the basic mechanism of the phenomenon. In this report, repeated fatigue crack propagation behavior due to an indentation flaw in a silicon nitride sintering body will be discussed.

2. Experimental Method

2.1. Fatigue Test of Silicon Nitride Atmospheric Sintering Body

After a surface crack was introduced to as-sintered material (the second phase of a grain boundary is the glass phase) of a silicon nitride

atmospheric sintering body that used a Y_2O_3-Al_2O_3-MgO assistant and also to the heated material (a part of the grain boundary phase was crystallized) thermally processed at 1,150°C by using the Vickers intrusion tip, they were subjected to a repeated load through the four-point bending test (dimensions of test specimen: 4 x 3 x 40 mm) at room temperature in the air. The crack propagation behavior was examined.

2.2 Simulation Test of Grain Boundary and In-Grain Phases

In order to simulate a grain boundary phase an in-grain phase (pure Si_3N_4), a sintering body (Material A) containing SiO_2 and Si_3N_4 assistants and a silicon nitride reaction sintering body (Material B) without an assistant were manufactured, respectively. Then the same tests as described in section 2.1 were carried out.

3. Conclusion

(1) In the case of the silicon nitride atmospheric sintering body, crack propagation was observed in both the as-sintered material and heated material in accordance with the repeated load (Figure 1).
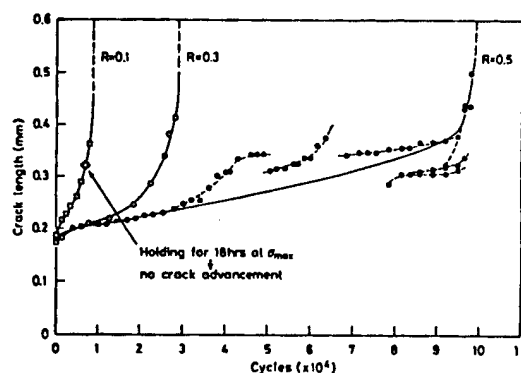
Figure 1. Crack Propagation Behavior of Silicon Nitride Atmospheric Sintered body
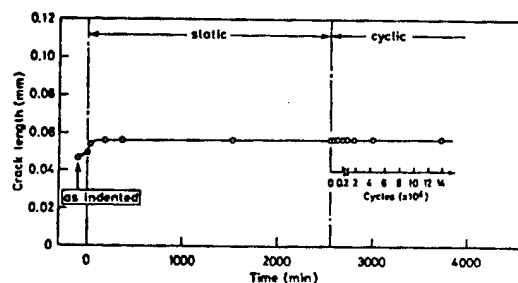
Figure 2. Crack Propagation Behavior of Material A

(2) The crack propagation curve had stress ratio R dependence and exhibited the reverse S letter-shape, reflecting the residual stress distribution due to indentation.

(3) The fatigue crack propagation path was mainly a grain boundary.

(4) According to the simulation described in section 2.2, fatigue damage did not occur in the acid nitride phase (Material A) of a grain boundary (Figure 2). Instead, crack propagation was observed in Material B. This indicated that damage could occur in the silicon nitride itself.

General Rules for Reactions of Silicon Nitride, Oxide

43067612 Tokyo NIPPON SERAMIKKUSU KYOKAI KANTO SHIBU KENKYU HAPPYOKAI in Japanese 4-5 Aug 88 p 44

[Article by Mamoru Mitsutomo, Akio Makishima, Hideo Kadoma, and Takayasu Ikegami, NIRIM]

[Text] 1. Introduction

To aid in the material designing of silicon nitride ceramics, first the general rules for the reaction of silicon nitride and an oxide were investigated. The difference between an effective chemical compound and one ineffective as a sintering assistant was examined from thermodynamic and crystalline chemical data. This study is a part of the research computing chemical composition and structure corresponding to demanded characteristics by utilizing an expert system.

Investigation Procedures

Sintering temperature (T = 2,000 K)

(1) Stability of chemical compound: $\Delta G < 0$ ($T_{diss} > T$), $T_{sub} > T$

(2) Low reactivity with Si_3N_4

Si_3N_4 + oxide = SiO_2 + nitride: $\Delta G_1 > 0$
Si_3N_4 + oxide = SiO + nitride + N_2: $\Delta G_2 > 0$
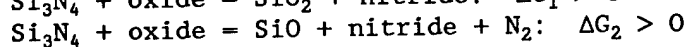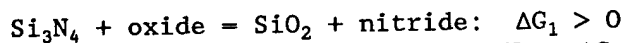
ΔG_1 and ΔG_2 for each oxide are shown in Figure 1. In this figure, the oxides in the upper right are stable. However, in the region of $0 < \Delta G_2 < 31.9$ (value of SiO_2), the partial pressure of SiO cannot be ignored, and the sintering performance and stability are believed to be greatly dependent upon the sintering conditions and kinetics.

(3) Region of liquid phase generation

The region and temperature of the liquid phase generation in the oxide-SiO_2 solid phase are related to the sintering performance and the strength of a sintering body at high temperatures.

(4) After sintering, soluble to β-Si_3N_4 in a solid phase: electronegativity, atomic radius (Figure 2).
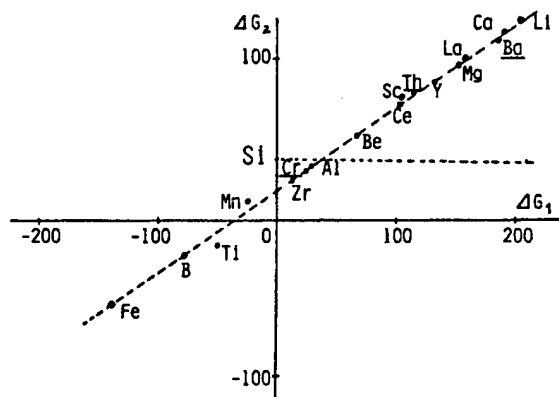
Figure 1. Plot of ΔG_1 and ΔG_2
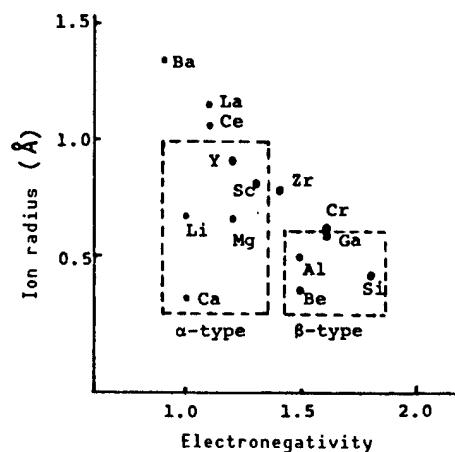
Figure 2. Region of Metal's Solid Solubility

(5) After sintering, soluble to α-Si_3N_4 in a solid phase: electronegativity, ionic radius (Figure 2).

(6) Relationship between boundary energy and boundary phase structure: grain shape.

This study is related to the "Research of Knowledge Base System for Chemical Material Design Support" funded by the Science and Technology Promotion Control Expenditure.

76

Conceptual Design for VLBI Satellite

43062587 Tokyo KEISOKU TO SEIGYO in Japanese Jul 88 pp 26-32

[Article by Toshimitsu Nishimura, Institute of Space and Astronautical Science: "Space VLBI Satellite Concept"]

[Excerpts] 1. Foreword

Very long baseline interferometry (VLBI) is a super-accurate measuring technology that has made remarkable progress over the last 10 years. [Passage omitted]

A baseline between two poles on earth is limited at most to about 8,000 km, if observation time is taken into consideration. However, space-based VLBI would make it possible to extend that baseline distance to several 10^4 km or even to several 10^5 km if one pole is set on the earth while the other is a satellite equipped with a large antenna. Measuring accuracy can also be improved accordingly.

For this reason, a space VLBI Working Group was organized in the Institute of Space and Astronautical Science (ISAS) and the staffs from the Astronautical Observatory's Nobeyama Space Radiowave Observatory, the Communications Research Institute (CRI) and ISAS closely studied the subject. The author was responsible for the preparation of a Working Group report published in the fall of 1987 (see References).

This article briefly describes the space VLBI satellite (Figure 1) Japan intends to develop in the future.

2. Development of VLBI Technology

Thanks to progress in the development of this VLBI technology in Japan, the CRI succeeded in measuring a baseline several thousand km long with an accuracy of about 3 cm, working mainly with an American team utilizing a 26 mϕ antenna located at its Kajima Branch. It is planned to use this technology to measure the movement of the continental plates, which are said to move about 10 cm a year, to verify the famous plate tectonics theory. Further, this technology should make it possible to develop an accurate earthquake prediction model. Recently, researchers have begun a series of joint experiments with China.
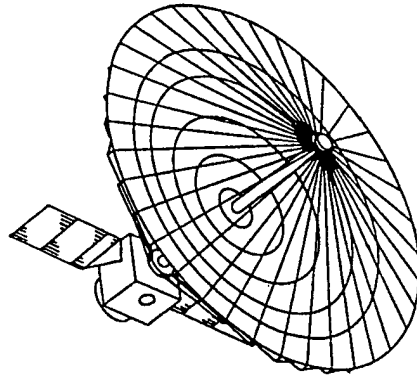
Figure 1. Space VLBI Satellite VSOP

The Kajima Branch is equipped with a super-accurate hydrogen maser atomic clock. It also has correlated equipment, including software and hardware. Its 34 mϕ radio telescope was completed recently, and it is evolving an energetic research program.

If the direction of a radiowave is known, its baseline length can be accurately measured, as mentioned above, by the correlative detection of its arrival time delay. Conversely, if the baseline length is known, the direction of a radiowave can be accurately measured. A group at the National Astronautical Observatory's Nobeyama Radiowave Observatory is trying to probe the internal constitution of quasars with radio astronomy utilizing this technique. It is gradually elucidating the mysteries of space by measuring changes in the internal constitution of quasars, including the popular 3C273. The group has conducted many experiments in conjunction with radiotelescopes in other countries, including the United States. [Passage omitted]

It should be specially mentioned that from 1986 to 1987 the ISAS and CRI jointly participated in the successful space VLBI experiment that used NASA's Tracking and Data Relay Satellite (TDRS).[4] The antenna of the TDRS is used mainly for relaying data, its surface precision is not designed for highly accurate astronomical observation and its diameter is small--a little less than 5 m. However, it proved somewhat unexpectedly that it could be effectively used to draw maps of the radiowave strength of the quasar in the 2 GHz and 15 GHz bands. This success enhanced the confidence of the members of the working group that it would be possible to develop a space VLBI satellite.

It would be very difficult to launch a satellite containing the required hydrogen maser atomic clock, which is both heavy and requires maintenance. However, a clock synchronization equivalent to a space-based atomic clock was achieved by synchronizing the transponder using the two-directional transmission from the earth and reception from the satellite to successfully carry out the correlative detection. This is very significant because it removed one big obstacle in the path of developing a space VLBI satellite.

In addition, the space VLBI satellite should prove useful for large-scale absolute space measurements, such as investigating the size and movement of the galactic system, measuring the distance to the further pulsars or quasars, and determining the size of the universe in ways that could not be envisaged by optical observation using conventional telescopes.

3. Space VLBI Satellite Concept

An outline of the concept for Japan's first space VLBI satellite will be given below, with emphasis on several important points.

3.1 M-V Launch Rocket

The ISAS currently uses the M3S-II three-stage or four-stage solid fuel rockets. The first model launched the "Sakigake" that successfully observed Halley's Comet in 1986, while the second launched the "Suisei" and "Ginga" for X-ray observation in 1987. The "EXOS-D," which will be used for plasma observation, is scheduled to be launched in 1989. This rocket is 1.4 m in diameter and has a gross weight of 64 tons. The Working Group undertook to determine how large a VLBI satellite could be launched using this rocket. It found that a satellite weighing no more than about 250 kg could be launched using this rocket. This meant that adequate observation could not be achieved, and the program was suspended. Also contributing to this decision was the fact that, from the viewpoint of international cooperation, the satellite could not stand comparison with the satellites of other countries. The Working Group then examined the possibility of using the new M-V rocket whose development is currently under consideration by the ISAS. This would be a large rocket about 2.4 m in diameter and about 110 tons gross weight. It was determined that if this rocket were used, a satellite with a 10-m antenna and weighing about 760 kg could be placed into a long elliptical orbit with a perigee of 1,000 km and an apogee of 20,000 km using the launching procedure shown in Figure 2, and the purpose of observation could almost be achieved. Therefore, consideration is being given to modifying the entire design of the VLBI satellite if the development of this rocket is approved.
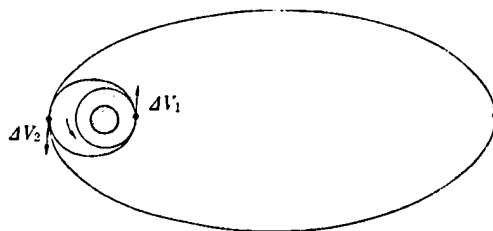
Figure 2. VLBI Satellite Launching Procedure
Perigee: 1,000 km
Apogee: 20,000 km

3.2 Satellite Body and Weight Distribution

Because the satellite is housed in the nose fairing when launched, the antenna and the two solar cell paddles are folded as shown in Figure 3(a). The satellite body is about 1.4 m in diameter and 1.2 m long. When unfolded after launching, the antenna forms a parabolic antenna 10 m in diameter. Each solar cell paddle is about 3 m long and 1.2 m wide. Total weight is 760 kg and power consumption is 330 W. The distribution of power use is indicated in Table 1. Table 1 includes about 840 kg for the injection motor, which can be changed depending on the launching method.
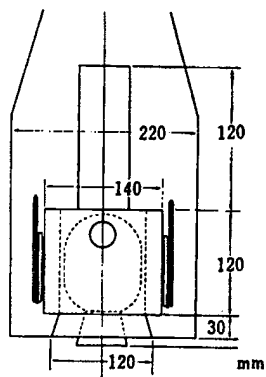
Figure 3(a). Configuration
When Launching
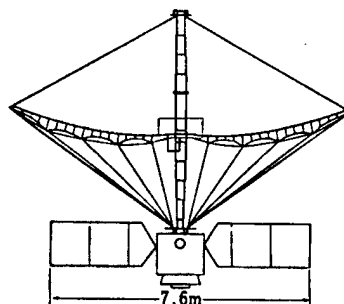
Figure 3(b). Configuration
in Orbit

Table 1. Weight and Power Distribution of VSOP

Subsystem	Weight (kg)	Power (w)
Observation and data transmission system	80	200
Attitude control system	50	70
Power system	95	--
Structure	110	0
Heat control system	40	50
Gas jet system	10	0
Apogee motor	70	0
VLBI antenna system	270	0
Integration system	35	10
Weight in orbit	760	--
Gas jet system propellant weight	20	--
Apogee motor propellant weight	820	--
Launching weight	1,600	--
Total power	--	330

3.3 Observation Antenna

Because 22 GHz, 5 GHz, and 1.6 GHz are widely used as the reception frequency bands for quasar observation, these will probably be used on the satellite. However, since it is difficult to house an observation antenna with a 5-m radius and 10-m diameter in the nose fairing even if it is folded, a hoop/column antenna that uses a telescopic column and a hoop is being considered as an antenna for use on this satellite, and the mirror may consist of a mesh structure. Mirror precision must be as accurate as 0.5 mm, which is an important subject to be studied in the future.

3.4 Observation Receiver and Communication Receiver

As mentioned above, three frequency bands are used for quasar observation. These channels are in the Ku-band (22 GHz), C-band (5 GHz), and L-band (1.6 GHz). Low noise amplifiers (LNA) and conversion circuits to the X-band are required for each channel, as shown in Figure 4, and the right and the left, respectively, are the methods that can be converted for circularly polarized waves by switches.
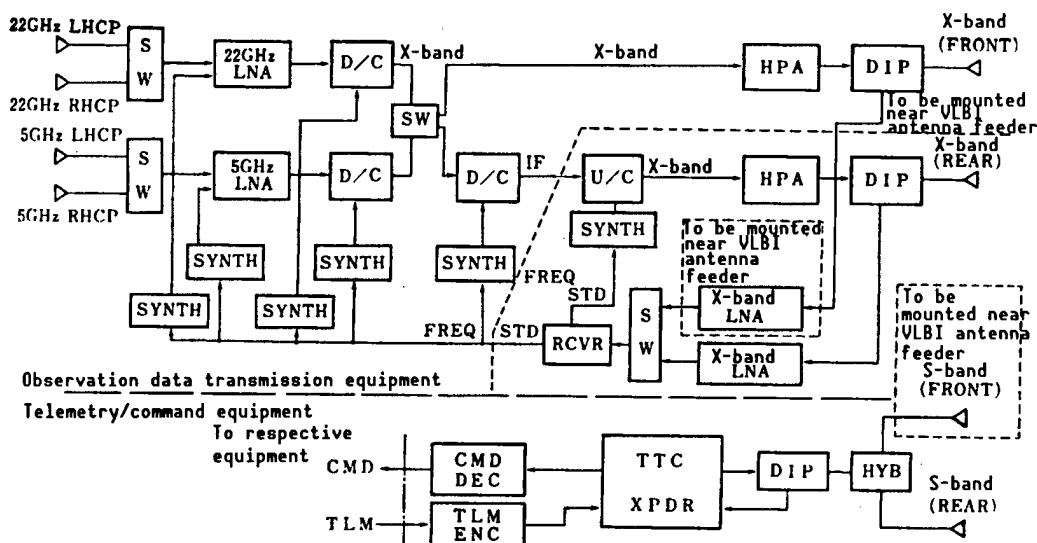
Figure 4.   Observation and Communication Transmitters
and Receivers

The S-band (2~3 GHz) and X-band (8~9 GHz) are used for the links to the earth stations. The X-band in particular is used for the transmission of observation data. Its transmission speed is expected to be 50 Mbps. The S-band is used to transmit commands, telemetry data, etc. It is very important to avoid mounting a heavy atomic clock, as noted in section 2. For this purpose, the information from an atomic clock located at the earth station is transmitted to the satellite, which is transmitting data back to the earth, and the onboard clock is synchronized by comparing them. Therefore, it is also essential to use the S- and X-bands as the links to the earth station from the point of view of ionospheric compensation.

81

3.5 Attitude Control System

The main purpose of the attitude control system is to turn the observation antenna in the direction of the quasar and to maintain a given attitude for a fixed period of time. The accuracy required of this system is about 0.01°. It is planned to mount a solar sensor, a geomagnetic sensor, and a star sensor as components of an attitude sensor system for this purpose. It is also planned to use an inertia model unit (IMU) as a short-time high-accuracy attitude standard. A reaction wheel that uses a three-axis zero momentum method will be adopted as an actuator for attitude maintenance and control. Magnetic torque will be used for unloading it.

It is necessary to rotate the satellite 180° from its launch attitude in order to use the apogee motor. A small active thruster (hydrazine fuel) is mounted for this purpose.

The discussion up to this point has served primarily to provide an outline of the onboard system of the satellite body. To gain a fuller understanding of the satellite it would be necessary to examine its power system, structural system, thermal control system, integration system, etc., but these cannot be discussed here.

4. Engineering Problems To Be Examined

The satellite body system, as presented above, can be described as a large, flexible structure on which to mount a large antenna and large paddles. This is a new concept that leads us into unknown fields. It will be necessary to conduct further examinations and many important problems remain to be solved.

4.1 Antenna

As noted above, the VLBI satellite will be equipped with a large, unfolding, mesh-structure antenna that requires a very high degree of mirror precision. Therefore, it is certain that its development will become a most important subject for future study. Its basic structure has not yet been examined sufficiently, and it may be necessary to devise an adjusting mechanism for the mirror, to say nothing of its unfolding mechanism. These must be examined together with the problem of weight. Since the antenna must be a large, flexible structure, and since the ratio of its weight to the satellite body is high, the effect of its vibration on the attitude control system, which must maintain the required accuracy of 0.01°, needs to be carefully studied by computer simulation and by ground tests.

4.2 Communication and Clock Synchronization

The receiving system and the transponder used for communications with the earth stations do not involve new technologies; more precisely, they are an extension of existing technology. However, LNA has problems in its cooling system and in its configuration. It will be necessary to carefully consider

the data transmission method, for there are two competing methods--analog and digital--each with its merits and drawbacks.

An even more important subject to be examined is that of clock synchronization. The transmission and reception method used for standard clock signals involving two waves is believed to be a realizable method, as demonstrated by the success of the TDRS experiment. However, the internal constitution of the transponder and the compensation at the earth station must be well researched. It is necessary to give further consideration to compensating for the Doppler shift caused by orbit fluctuation by improving the accuracy of orbit decision, to say nothing of compensating for the effects of the ionosphere and the atmosphere.

4.3 Attitude Control System

This is basically a three-axis maintenance and control method using reaction wheels. This system has been in use for some time, and it is believed that it is capable of maintaining the required accuracy of 0.01° in ordinary satellites. The problem is that the satellite is a flexible structure combining a large antenna and large paddles, as shown in Figure 1, and it would be necessary to design an autonomous control function using onboard computers and software to cope with fine vibrations that are hard to anticipate on the ground. It is almost impossible to conduct tests on such a large structure on the ground in conditions close to the zero gravity of space. And even if such tests were conducted, the extent to which they would reflect the real conditions of space remains doubtful. However, it is dangerous to rely too much on onboard computers if their performance and weight must be taken into consideration. As stated in references 6 and 7, it may be wise to try to devise numerical formulas and computer simulations for a dynamic model of the flexible structure to the extent possible, with only the remaining basic section having to rely on the onboard system.
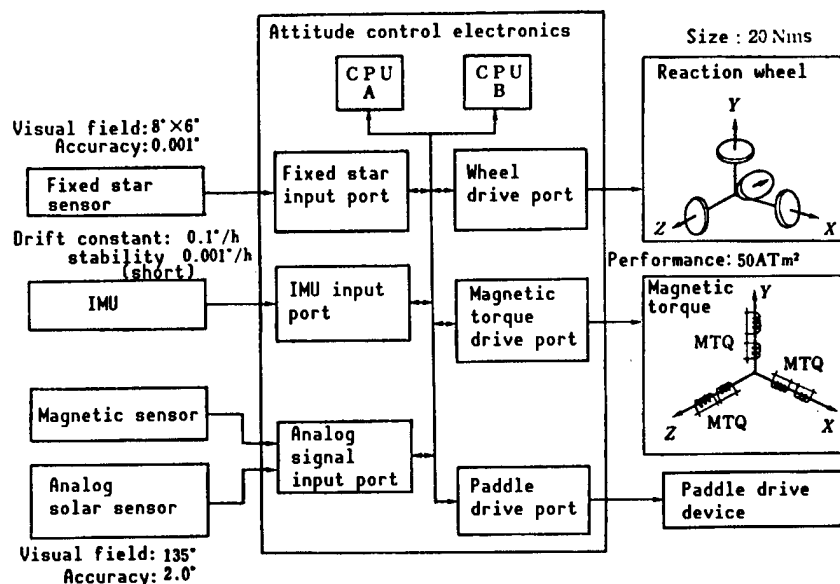
Figure 5. Block Diagram of Attitude Control System

83

4.4 High Gain Antenna and Feed Horn

A directional parabolic antenna may be required for communications with the ground. In this case a gimbal mechanism and a driving mechanism will be necessary, and their weight will become a problem. A control mechanism must also be devised as this is a revolving satellite. It will be necessary to examine methods that can arrange some nondirectional antennas that are electrically switched or to consider a phased array method.

The Cassegrainian or Gregorian methods that use subreflectors are being considered for the observation antenna, but a means to unfold about three legs must be devised in this case. The structure of the feed horn at the center of the mirror will be changed depending on whether the K-band and the C-band are to be received simultaneously or separately. This must be examined in the future in connection with receiving methods.

4.5 Data Processing System

A data processing system as discussed here refers to an overall data processing system consisting of correlated processing of the observation data transmitted from the satellite and the data obtained directly from the quasar at other earth stations. This includes hardware and software, including data compensation, image composition, etc. The number of VLBI satellites will be limited to one for the time being. The ISAS 64 mϕ (Usuda), the National Astronautical Observatory 45 m (Nobeyama), and the CRI 34 m (Kajima) are expected to be the earth stations. Therefore, the correlative processing of nine channels--three baselines and three channels (Ku, C, L), respectively--must be conducted at all times. There is a possibility that the number of processing operations will increase geometrically if cooperation with foreign stations becomes a reality. It would be impossible to cope with such a situation even with a super computer like the vector processor. It will probably become necessary to develop a special computer that can conduct Fourier transformations or reverse Fourier transformations by dividing the channels in the frequency region more finely, like the FX system located at Nobeyama Radiowave Observatory, or by using a system whose hardware can conduct mutual correlative processing.

It is impossible for the number of personnel presently assigned to the respective stations to take care of data compensation and image composition. It will, therefore, be necessary to develop an automated system--including a software system and a hardware system according to circumstances--to take care of these tasks.

5. Future Prospects

It is fresh in our memory that four organizations--ESA, IKI (USSR, East Europe), ISAS, and NASA--launched five probes--Giotto (ESA), Vega I, II (IKI), Sakigake, Suisei (ISAS)--in preparation for the approach of Halley's Comet in 1986 and succeeded in observing the comet by approaching it. An organization called the Interagency Consultative Group (IACG) was organized by these four agencies about 6 years earlier for the purpose of securing international cooperation for this mission. It became a big motivating

force for the successful mission by holding meetings every year. After completing the flyby in March 1986, the IACG met in Padova and Rome, Italy, where it decided to continue its work. Its decision was based on the realization that such an international organization aimed purely at space science was very significant. It took up solar terrestrial physics, that is observation of the interference phenomenon caused by solar wind and the geomagnetic field, space VLBI, planet probing, etc. as its immediate targets.[8]

The IACG met in Kyoto in October 1987, where it discussed the Soviet Radioastron, the ESA's (NASA's) Quasat, and Japan's VSOP (VLBI Space Observatory Programme) regarding the space VLBI. The Radioastron weighs 5 tons and its antenna is 10 m in diameter. The Quasat weighs 1.2 tons and its antenna is also 10 m.[2] As noted above, VSOP weighs 760 kg, its antenna diameter is 10 m, and its target observation frequency band is almost the same as theirs. Although VSOP is a little lighter than the others, its capability would not suffer by comparison, because it is possible to make its communication system lightweight thanks to Japan's electronics technology.

The technical requirements imposed on the quasar observation VLBI satellite are very strict. However, since it is a single-purpose satellite, there should be little trouble in meeting these different requirements by adjusting various pieces of equipment from other science satellites, for example, those developed by ISAS, which contain various pieces of observation equipment.

Ideally, the orbital apogee should come at a point where the baseline is longest. However, there is considerable flexibility in the selection of the shape of the orbit, its inclination, launch timing, etc., and it may be said that it is sufficient simply to launch it as far out as possible. It may be said that it will be much easier to launch the VLBI satellite than it is to launch missions to Halley's Comet, the moon, or the planets (Figure 2).

At the same time, it must be stressed that international cooperation is indispensable for the space VLBI program, because the locus on the U-V plane will be very limited if only the baselines between the Japanese stations and VSOP are used. The U-V plane is the baseline, or the picture drawing the locus of the projection against the vertical plane in the direction of the quasar on the line linking a station and the satellite, and the U, V axis makes a spatial frequency scale (Figure 6). Therefore, spatial resolution is improved if the locus passes everywhere through the plane. This makes it possible to draw a more precise map indicating the internal constitution of the quasar. The locus on the U-V plane can be increasingly varied through cooperation with foreign stations, and observation time could be utilized more effectively if foreign stations would conduct observations for the period of time when the VSOP cannot be observed from Japan. At the same time, however, increased observation geometrically increases the amount of correlative processing, as described in section4. This problem is scheduled to be discussed in meetings of the IACG, which will also examine cooperative relationships, work assignments, etc.
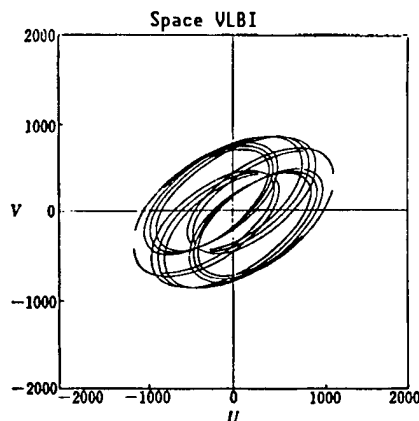
Figure 6. U-V Plane
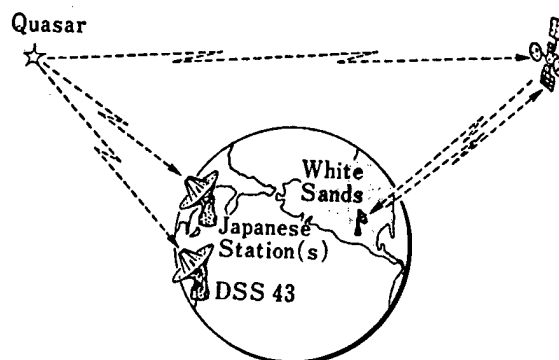
Figure 7. Cooperation With Foreign
Stations in Space VLBI
Program

The Radioastron is scheduled to be launched in 1991, but it is said that its launch may be delayed to about 1994 due to internal problems. The launch of the Quasat may also be delayed a little beyond its original schedule to about 1995. As mentioned above, the launch of the VSOP is scheduled for 1994-1995, although this will depend on the development schedule for the new M-V rocket. It is certain that excellent results could be obtained through cooperation with other countries if their satellites could also be launched about that time. It is desirable that the orbit size be adjusted to cover the U-V plane well by that time. This will also be discussed at future IACG meetings. [Passage omitted]

References

1.   Space VLBI Observation Program
      I. WG Report
      II. Space Observation by Space VLBI-VSOP
      III. Satellite System
      ISAS Space VLBI.WG Report, 1987.

2.   "Quasat: A VLBI Observatory in Space," ESA Report SP-213, Proceedings of workshop held at Gross Enzersdorf, Austria, 1984.

3.   "Radioastron: Ground-Space Radio Interferometer for Astrophysics," Brief note presented by IKI Group at Seventh IACG Meeting, Kyoto, 1987.

4.   G.S. Levy, et al., "Very-Long Baseline Interferometry Observations Using an Orbiting Radio Telescope," SCIENCE, Vol 234, 1986, pp 187-189.

5.   T. Nishimura and H. Hirabayashi, "Space VLBI: Science and Technology," Control-Theory and Advanced Technology, Mita Press, 1986.

6.   Nishimura, "Movement of Flexible Structure in Space," MEASUREMENT AND
      CONTROL, Vol 26, No 10, 1987, pp 829-834.

7.   Tsuchiya and Kashiwase, "Control of Large Space Structures (LSS),"
      Ibid., pp 855-862.

8.   Seventh Meeting Summary of IACG-Inter Agency Consultative Group for
      Space Science, Kyoto, 1987.

Balloon Problems Force Aborting of Mode Shuttle Test

43062019a Tokyo ISASU NYUSU in Japanese Oct 88 p 4

[Article by Koki Matsuo]

[Text] At 0545 hours on 21 September 1988, the large balloon B15-RFT-1 carrying a winged airframe was released from Kagoshima Space Observation Station. The release was delayed for 3 days because of weather, but the day was blessed with good conditions with no wind on the ground, and the upper layer wind conditions appeared to guarantee the firing of the rocket in the predetermined area over the eastern ocean. The balloon continued its ascent smoothly, but at 0650 hours, immediately before it was to begin the horizontal float at an altitude of 18 km, it suddenly started to descend. Therefore, by a radio command from the ground, the gondola carrying the winged airframe was separated from the balloon and after taking necessary measures from the safety standpoint, splashed down with a parachute at 0708 hours in the sea approximately 80 km east of Uchinoura. This meant that, unfortunately, the reentry test of the winged airframe could not attain its goal. For now, it is presumed that the balloon lost its buoyancy for some reason, but the real reason must be found by future study.

Observation of High Energy Particle Beam

43062019c Tokyo ISASU NYUSU in Japanese Oct 88 p 7

[Article by Shuji Orito, Faculty of Science, Tokyo University]

[Excerpt] [Passage omitted] Besides electromagnetic waves, elementary particles and nuclei are falling from space and most of these particles are electrically charged. The energy level, GeV, of these space beams is as high as about 10^9 eV. Thus, it is possible that these particle beams are carrying information particularly on high energy astronomical phenomena or space phenomena involving elementary particles. This paper introduces our Elementary Particle Research Laboratory's plan to observe particles with cooperation of the Institute of Space and Astronautical Science.

Figure 1 shows the outline of the device we are producing. Its outer diameter is 1.5 m, the length is 2.6 m, and total weight is about 900 kg. In its center it has a thin superconducting solenoid which is capable of creating a homogeneously high magnetic field of about 1.2 Tesla. Installed inside the solenoid is a cylindrical drift chamber which continuously and with good precision determines the magnetically bent three-dimensional loci of charged particles and their electrolytic loss, and also measures the charge and momentum. It is a relatively light-weight and compact device, but it can measure momentum of up to 500 GeV/c with an areal stereoangle several tens of times greater than that of the previous balloon-lifted spectrometer.
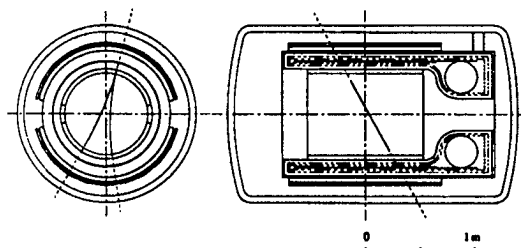
Figure 1.

The device is an all-around type, capable of simultaneous measurements of various kinds, and is designed so that it can be loaded on a space station.

However, for the time being, we want to confirm the device's dependability by balloon experiments over the next several years. We will be aiming at the following goals in physics: 1) search for an ultramicroquantity, 10^{-8} vs helium, of nuclei including antihelium; 2) search for space-originated antiprotons; 3) precise measurement of position energy spectra; 4) spectra of various isotopes; 5) search for unknown elementary particles; and 6) observation of GeV γ-ray.

Although we were quite accustomed to using this type of particle detector, an integrated electronic circuit, and data processing with a portable small-size computer in accelerator experiments of the past, we have never tried to collect data off the ground. Therefore, we manufactured a small-size (though weighing 550 kg) device (photograph in Figure 2 [not reproduced]) containing all the detectors, including the drift chamber, which will be used in the main experiment, and launched it from Sanriku with a balloon in June 1988. It was a successful level flight for 32 km and 10 hours during which the instruments and the computer operated normally, and data collection and signal transmission and receiving were successful as well. Furthermore, we were fortunate to be able to recover the device without incident.

Based on this valuable experience, we have begun the design of the main experiment; we are already manufacturing the key parts.

Table 2. Comparison of Parameters of Research Submersible and "Shinkai 2000"

Item	Parameters of 6,500-m research submersible "Shinkai 6500"	Parameters of 2,000-m research submersible "Shinkai 2000"
Submersible depth	6,500 m	2,000 m
Percentage of sub- mersible sea area	About 98 % of all ocean areas About 96 % of Japan's exclusive 200-mile economic zone	About 30 % of Japan's exclusive 200-mile economic zone
Number of crew members	3 (2 steersmen, 1 researcher)	Same
Size: l x w x h	About 9.5 x 2.7 x 3.2 m	About 9.3 x 3.0 x 2.9 m
Weight in the air	About 25 tons	23.2 tons
Ascending and descending speed	About 43 m per minute (buoyancy adjustment and release system)	About 22 m per minute (buoyancy adjustment and release system)
Time required for submerging operations For:	Total 9 hours	Total 8 hours
lowering into water	0.5 hour	1.0 hour
reaching maximum depth	2.5 hours (6,500 m)	1.5 hours (2,000 m)
research at seabed	3.0 hours	3.0 hours
surfacing	2.5 hours	1.5 hours
lifting onto mother ship	0.5 hour	1.0 hour
Possible hours of oxygen supply, other life support systems (3 crew members)	9 hours + 5 days (129 hours)	8 hours + 3 days (80 hours)
Pressure-tight globe for crew chamber	Inside diameter 2 m, made of titanium alloy	Inside diameter 2.2 m, made of ultrahigh- tensile steel (NS90)
Ship speed	Maximum 2.5 knots (about 4.6 km per hour)	Maximum 3 knots (about 5.6 km per hour)
Power source	Storage battery (silver- zinc battery, 86.4 kwh)	Storage battery (silver- zinc battery, 61.6 kwh)

[continued]

Progress in Developing Research Submersible 'Shinkai 6500'

43067601 Tokyo KAIYO KAIHATSU NYUSU in Japanese May 88 pp 33-40

[Article by Hirotoshi Tokitake, chief of Deep-Sea Technology Development Division, Japan Marine Science and Technology Center: "Research Submersible 'Shinkai 6500'"]

[Text] 1. Introduction

The Japan Marine Science and Technology Center during the last fiscal year conducted a survey of the needs of deep-sea research and observation among learned men and researchers from various circles. This survey clearly showed that research at depths of 6,000 meters--including research on resources, such as submarine minerals; research on disaster prevention and safety, such as earthquake prediction; and scientific research on marine life, etc.--has become an urgent theme.

To cope with these needs, the Japan Marine Science and Technology Center is pushing construction of a research submersible called "Shinkai 6500," which will be capable of descending to a depth of 6,500 m. The "Shinkai 6500" is scheduled for completion in 1989. It can be said that, in creating this deep-diving research submersible, the actual results of the construction and operation of the research submersible "Shinkai 2000," which is producing valuable results, are being fully taken into account.

The Japan Marine Science and Technology Center is pushing the construction of a mother support ship together with the deep-diving research submersible. At the same time, it is planning to construct an unmanned submersible for such purposes as preliminary research in abyssal areas and emergency rescue of research submersibles. it is seeking to develop a multifaceted research system that will incorporate these systems.

2. Design Concept and Principal Characteristics of Research Submersible

That the new vessel will submerge to a depth of 6,500 m alone calls for many technical developments for individual pieces of equipment and the system as a whole, for example with respect to the requirements for water pressure resistance and ascending and descending speed. Also, the vessel must have sufficient maneuverability to enable it to carry out close observation of

93

objects near the seabed. The fundamental performance characteristics that the submersible should have are given below.

--High-speed ascent and descent to ensure sufficient time for research and observation at the seabed.

--Low-speed maneuverability to facilitate close observation.

--Capability to effectively contain and operate research and observation devices.

Based on the results of comprehensive studies, the operating time schedule for this research submersible has been specified as 9 hours (6,500-m depth) for the overall operation as shown in Table 1.

Table 1. Operational Time Schedule of "Shinkai 6500"

Lowering into the water	0.5 hour
Descending	2.5
Research and observation	3.0
Ascending	2.5
Lifting onto the ship	0.5
Overall operation	9.0 hours

With regard to reliability and safety, measures are being taken to introduce such techniques as FTA (fault tree analysis) from the stage of the initial plan study and FMEA (failure mode and effect analysis) in parallel with designing the vessel. It is also planned to evaluate and review reliability and safety, focusing on such matters as design and inspection of subsystems and apparatus and ways to restore them in an emergency.

The technical details (including a comparison with the "Shinkai 2000") of this research submersible are shown in Table 2. Its general configuration is shown in Figure 1, and a conceptual drawing of the completed vessel is shown in Photo 1 [not reproduced].

3. Basic Outline and Applied Technologies for Subsystems

3.1 Type of Ship and Structure

To raise the research efficiency of the deep-diving research submersible, it is necessary to shorten the time required for descending and ascending between the surface and the bottom of the sea to the greatest possible extent. To that end, it is necessary to take such measures as, first, reducing the weight of the research submersible itself so it can be loaded with a large amount of ballast for descending and ascending, and, second, designing a vessel with less resistance to the water it meets while descending and ascending.

Item	Parameters of 6,500-m research submersible "Shinkai 6500"	Parameters of 2,000-m research submersible "Shinkai 2000"
Driving system	Propeller system (propeller for main thrust x 1 unit: capable of shaking head left and right; propeller for vertical movement x 2 units: tunnel built-in type fixed system; propeller for horizontal movement x 1 unit: tunnel built-in type fixed system)	Propeller system (propeller for main thrust x 1 unit: capable of shaking head left and right; propeller for vertical movement, and supplementary forward and backward movement x 2 units; proper use of head shaking, exterior exposing type)
Main research and observation equipment	Manipulator (2 units), underwater TV camera (2 units), underwater still camera, sample container, CTDV (device to measure water temperature, underwater sound velocity, etc.), observation sonar (device to prove the shape, etc., of the objects at a distance from the submersible)	Manipulator, underwater TV camera, underwater still camera, sample container, STU, forward obstacle detecting sonar
Payload (weight taken for replacement research and observation apparatuses and samples)	200 kgf	100 kgf
Power source for payload	AC 100 V, DC 108 V	AC 115 V, DC 28 V
Hydraulic power source for payload	100 kgf/cm^2 (differential pressure), 6.21 ℓ/min	None
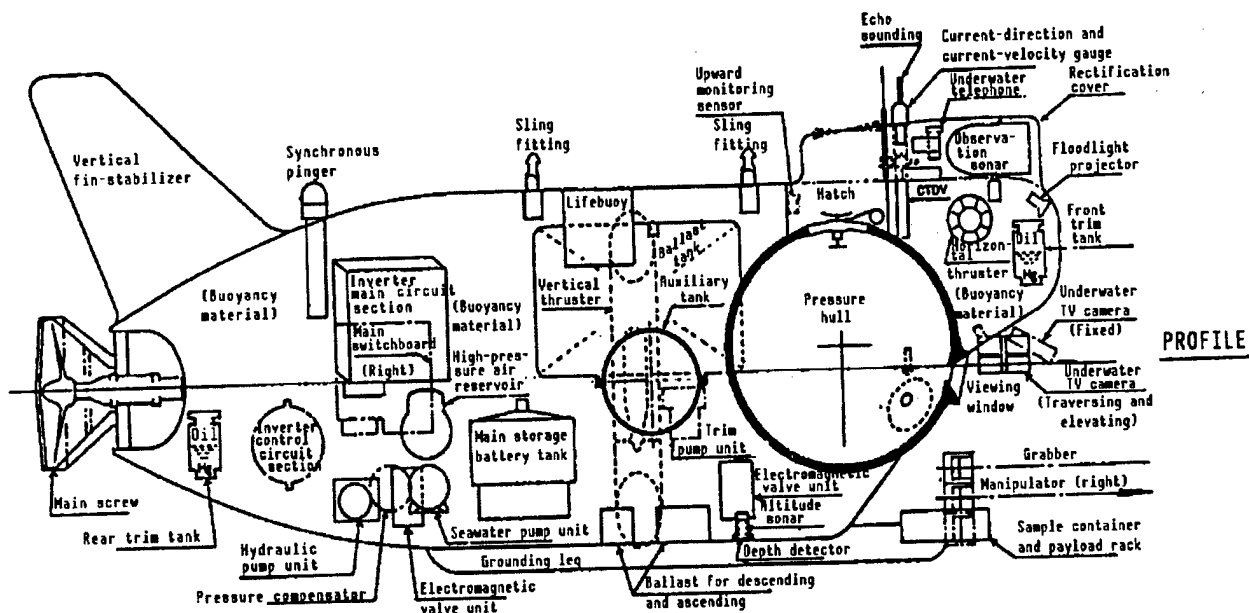
Principal Specifications

Full length	About 9.5 m
Maximum width	About 2.7 m
Height	About 3.2 m
Weight in the air	About 25 t
Maximum submerging depth	6,500 m
Pressure hull internal diameter	ϕ2.0 m
Crew	3 persons

Figure 1.   General Arrangement of 6,500-m Research Submersible (A)
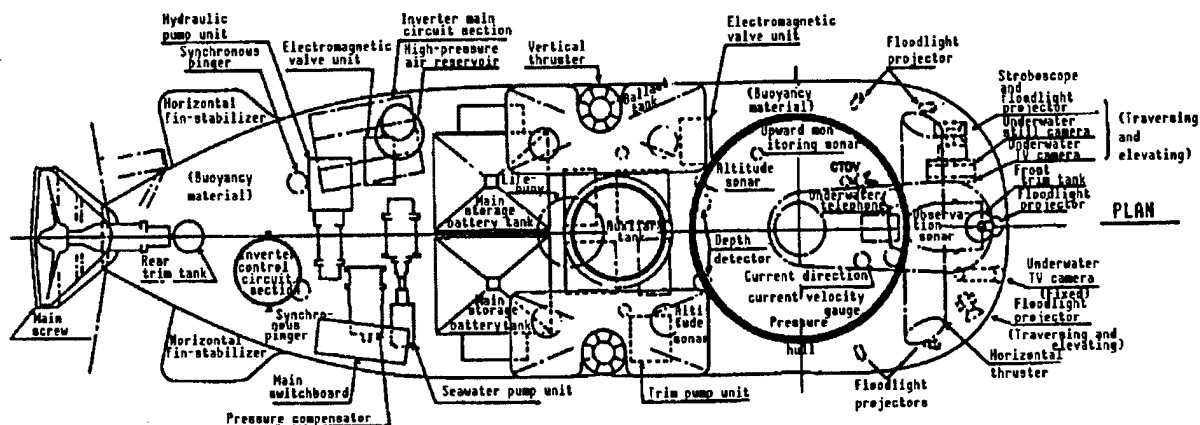
(B)

Table 3.   Structural Materials for "Shinkai 6500"

Structural division		Mechanical properties (kgf/mm^2)				
Material	Relevant standard	0.2% proof stress	Tensile strength	Elastic modulus	Specific gravity	Applied section
Pressure hull						
Titanium alloy Ti-6Al-4V EL1	AMS 4907C	81 or above	88 or above	about 11,500	4.42	Pressure hull general section, hatch viewing window, foaming, cable gland
Methacrylate resin	JIS K6718	Compressive strength 12.6	7.6	about 300	1.19	Viewing windows obser vation window, camera window)
Pressure vessel						
Titanium alloy Ti-6Al-4V EL1	AMS 4907C	81 or above	88 or above	about 11,500	4.42	Auxiliary tank invertor vessel
Framework structure						
Industrial pure titanium ex-truded section	ASTM 348 Grade 3	38.5 or above	45.5 or above	about 10,900	4.5	Frame material
Industrial pure titanium rolled plate	JIS H4600 Grade 3 TM 49 H	35 or above	49 or above	about 10,900	4.5	Bracket
Titanium alloy Ti-6Al-4V EL1	AMS 4930B	77 or above	84 or above	about	4.42	Sling fitting beam for above
Skin, others						
FRP	NDS K 6701 B Grade 2	--	Standard- -- state bending strength 30 or above		1.7	Skin, fin-stabilizer, grounding leg, ballast tank
Stainless steel	JIS G4303 SUS 304	21 or above	53 or above	about 20,400	7.93	Skin-fixing screw

To reduce the weight, titanium alloy with a high specific strength (a ratio of 0.2 percent proof stress to specific gravity) is often used for the main structure and high-strength components of this ship. In like manner, the framework structure of the ship is composed of pure titanium sections and rolled plates. Further, for such structures as the skin and ballast tank for which strength is not required, FRP, etc., are used. Table 3 shows the structural materials used for this ship.

In addition to the selection of appropriate and effective materials, manufacturing technology is also important. In the manufacture of the pressure hull and the three pressure vessels made of titanium alloy, hot forming technology and heat treating technology are used in the material manufacturing process. Other advanced technologies--such as a three-dimensional machine processing method, electron beam welding technology, and nondestructive test technology in the processing, assembling, and manufacturing process--have been organically developed and applied. The combination of materials and manufacturing technology have made it possible to create a high-accuracy, lightweight, and high-strength pressure-tight structure. With regard to the pressure hull, which is to accommodate three crew members, a fatigue collapse test using a scale model (inside diameter 700 mm) was conducted in 1986 to verify the design and manufacture of the real equipment. Figure 2 shows the collapsing pressure of the pressure hull calculated from a series of test results and shape measurements. The manufacturing accuracy (sphericity 1.004) of the pressure hull makes it possible to ensure that the hull has sufficient collapse-resistant strength.
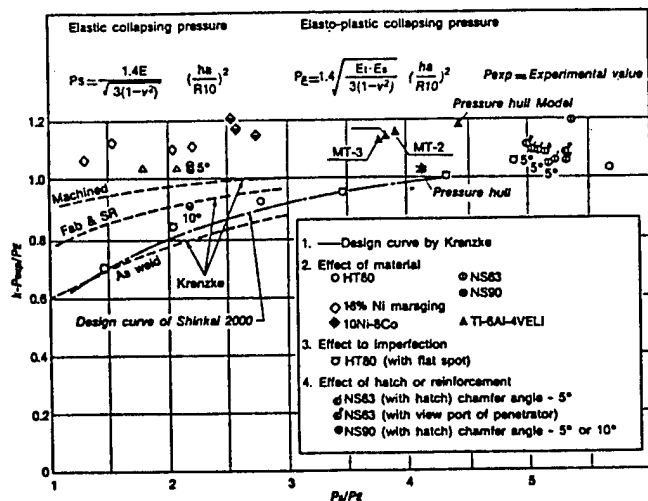
Figure 2.   Comparison of Collapsing Pressure
(Relationship between P_{exp}/P_E and P_s/P_E)

Meanwhile, the development of ways to house electric equipment, etc., in an oiled equalizing structure instead of the traditional heavy pressure-tight structure has also been pushed. Specifically, the main invertor circuit section comprising the power transistor, etc., has been housed in an oiled equalizing vessel, thereby reducing the weight of the vessel.

Because it is essential for the submersible to achieve neutral buoyancy (drifting about in a neutral state) so it will be capable of moving about freely along the seabed using its own thruster and auxiliary tank pumping system, buoyancy materials become very important as hull fittings. Thus, a buoyancy material (specific gravity 0.54 g/cm^3, collapse strength 1,200 kgf/cm^2) that can withstand the pressure at a depth of 6,500 m (680 kgf/cm^2) while at the same time having a low specific gravity has been developed. This new material has a binary structure in which large-diameter and small-diameter hollow glass spheres are combined in a cubic lattice. Additionally, a manufacturing process that fills the openings between the hollow glass spheres with heat-treated epoxy resin by the vacuum impregnation method and then hardens it by specific heat treatment has been developed and applied. A careful inspection of each manufacturing lot of buoyancy material has confirmed an adequate level of performance.

3.2 Power Plant

This vessel carries an electric system and a hydraulic system driven by its power plant.

The electric system comprises two main storage batteries, the main switchboard and the main invertor circuit, and control sections for five motors and communications. Figure 3 shows an outline of the system. The main circuit is a direct-current, two-wire circuit system. Its rated voltage is 108 V, and parallel feed is used to improve its reliability.
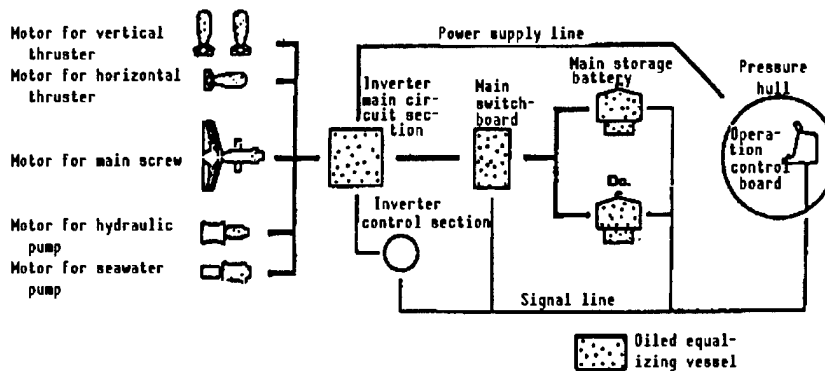
Figure 3. Diagram of Electric System

A silver oxide-zinc battery is used as the main storage battery, as is also the case for the "Shinkai 2000." This silver battery has a high energy density for weight and cubic volume, and it can last as long as 2 years, even when charging and discharging high electric current. This vessel has two groups of storage batteries wherein 72 cells of 400 Ah x 1.5 V each in charging and discharging capacity per cycle are connected in series. Thus, a high-performance secondary battery with a life of 2 years and 35,000 Ah in total discharging volume has been developed. Through charging and discharging and life tests conducted in the initial stage of designing, these performance levels have been confirmed.

99

Alternating current induction motors have been adopted for the main screw, vertical thruster, horizontal thruster, hydraulic pump, and seawater pump driving motors. These motors were chosen because they are easy to maintain and control, and also because they are capable of efficient control and operation in combination with the invertor. The invertor has thus far been structured so that it can be housed in a pressure vessel, as was done in the "Shinkai 2000." But in the new vessel, newly developed pressure-tight high-power transistors, capacitors, etc., have been combined to produce a lightweight, small oiled equalizing main invertor circuit section. This new design is ahead of the rest of the world.

The invertors for the motors all use variable voltage-variable frequency (VVVF) control of the pulse width modulation (PWM) system, taking into consideration such matters as the importance of starting control under the low temperature and high pressure conditions at the deep-sea bottom. Meanwhile, the invertors for communications, such as the nautical communications system and the research and observation system, which call for load-stabilized voltage output, use constant voltage-constant frequency (CVCF) control.

For the hydraulic system, measures have been taken to adopt a high-speed variable discharge-type pump like those used for aircraft, thereby forming a highly reliable system with a capacity of 12 ℓ/min in discharge and 140 kgf/cm^2 in discharge pressure during ordinary use. The oil discharge line for the hydraulic equipment is designed so that it is linked with the pressure compensator. Thus, the pressure in the discharge line is equal to the depth pressure, and the hydraulic pressure is always 140 kgf/cm^2 higher than the depth pressure. As for the hydraulic system, which includes various actuators, operational tests in a high-pressure water tank have been conducted at the unit level, and good results have been obtained.

3.3 Ballast System and Trim System

The most fundamental and important task of any submersible is submerging (descending and ascending). In the new research submersible this has been attained by using gravity and buoyancy, thus conserving energy. In this vessel two blocks each of descending ballast and ascending ballast made of stacked iron plates are placed and kept symmetrically widthwise and lengthwise in the hull center, and the principal weight adjustment is effected by releasing these ballast plates. The vessel goes up and down while carrying out research and observation after reaching neutral buoyancy by releasing the descending ballast near the seabed. Control is effected primarily by pumping seawater in and out of the auxiliary tank (300 kgf capacity) with the seawater pump. The process of these submerging operations is shown in Figure 4.

A block diagram of the auxiliary tank pumping system is shown in Figure 5. This system, which produced satisfactory results in the "Shinkai 2000," is designed so that pumping water in and out of the auxiliary tank can be strictly controlled regardless of the depth. In other words, a pressure balancing valve is provided on the seawater pump discharge side, the driving
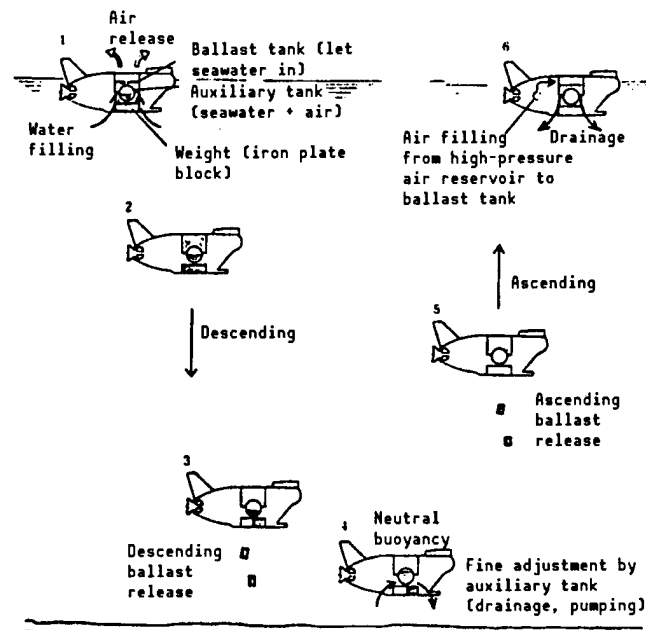
Figure 4. Process of Submerging (Descending-Neutral
Buoyancy-Ascending)
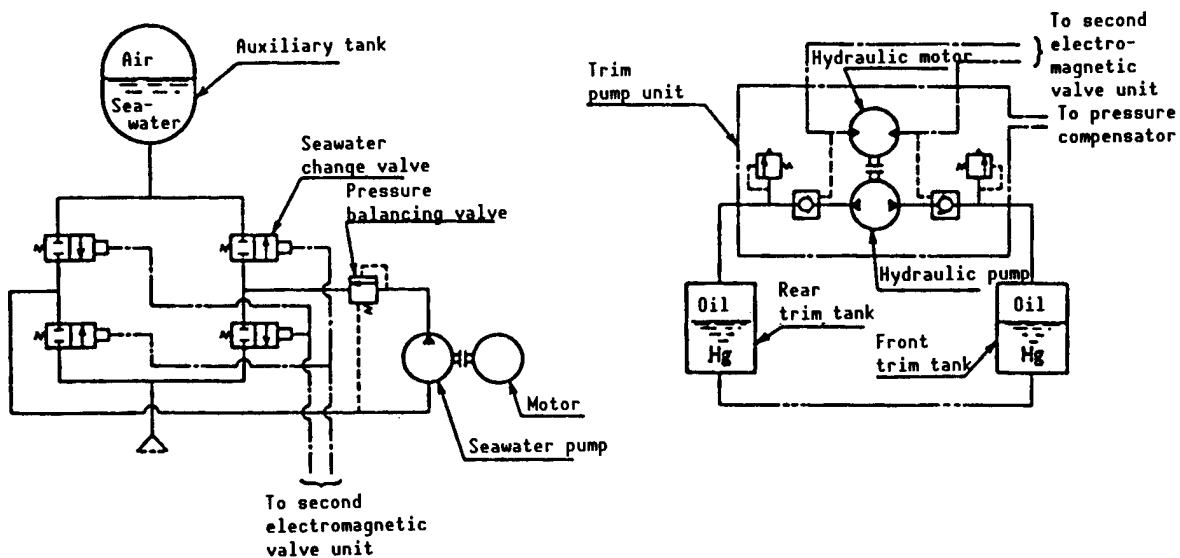
Figure 5. Diagrams of Variable Ballast System and Trim System

source, to keep the pump discharge pressure a little higher than the inlet
pressure for both pumping and drainage, thereby enabling the load to be
fixed and the pumping and drainage to be stabilized. Further, an axial-
plunger high-speed seawater pump (normal discharge pressure 685 kgf/cm^2,
1,700 rpm) that can work at high pressures has been developed. The plunger

exterior and the cylinder interior of the pump have been coated with ceramics to produce a high-accuracy high-durability clearance-type seal.

The trim adjustment is effected by hydraulically moving mercury, which has a high specific gravity, between the trim tanks installed in the bow and the stern. The trim adjustment capacity is in the range of ±10°. It is started when trim adjustment is needed in such cases as the collection of samples from the seabed and storing them on the bow end.

3.4 Driving and Steering System

For its driving and steering system, this vessel uses a main screw capable of shaking head left and right at its stern, a horizontal thruster in the upper section of its bow and vertical thrusters on both sides of its hull center. The horizontal thruster and the vertical thrusters are buried in the skin duct in order to lower fluid resistance and improve the driving property. The specifications of the driving system are listed in Table 4.

Table 4. Specifications for Driving System

	Main screw	Vertical thruster	Horizontal thruster
Diameter	1,210 mm	420 mm	400 mm
Pitch ratio	0.7	0.94	0.95
Expanded area ratio	0.35	0.60	0.60
Boss ratio	0.163	0.170	0.1785
Type of blade	NAU	Kaplan	Kaplan
Number of blades	3	4	4
Bollard thrust (Ordinary use)	About 350 kgf	About 50 kgf x 2	About 30 kgf

The main screw is structured so that it is capable of making an 80-degree turn both to port and to starboard. Thus, in combination with the thrust of the horizontal thruster at the bow, it enables the ship to turn effectively. The ship can turn in any direction in the horizontal plane at low speed. This maneuverability greatly improves the vessel's ability to carry out close observation. Examples of lateral movement and turning motion effected by the combined thrust of these thrusters are shown in Figure 6.

Control of the vertical thruster is independent of the direction of horizontal movement. Vertical movement at about 0.5 kt can be carried out simultaneously with horizontal movement.

The control box for these thrusters, which is installed in the pressure hull, is designed to be portable. This makes it possible to operate the vessel while looking out the viewing window. The control panel features two joysticks, a thruster rotation indicator, etc.

102
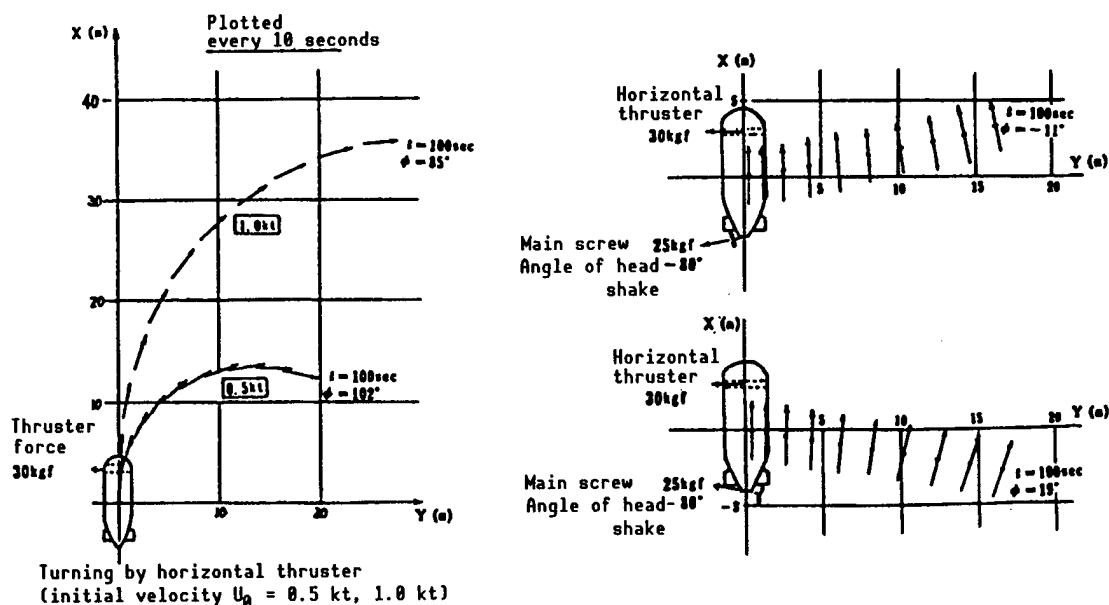
Figure 6. Examples of Lateral Movement

The main screw can achieve a maximum advance speed of 2.5 kt and a normal thrust of about 350 kgf. The vertical thruster and the horizontal thruster can generate a force of about 100 kgf and 30 kgf each in their respective directions.

3.5 Research and Observation System

It is very important for the research submersible to have a complete set of equipment and apparatus for research and observation and to guarantee their independent operation. In this ship, therefore, measures have been taken to design equipment that fully incorporates the experience gained in the operation of the "Shinkai 2000" and that introduces the latest achievements in the rapidly-advancing field of sensor technology. These efforts are summed up in the following points:

• Equipping the vessel with two manipulators that have a degree of freedom of 7 and 5, respectively, while incorporating a master-slave force-sensing control system has improved its maneuverability.

• The placement of the three viewing windows has been improved to provide a wider field of vision. At the same time, two high-resolution television cameras (horizontal resolution about 450 lines) have been installed in front of the observation window.

• The rack used to hold the observation equipment and the apparatus for replacement (for payload) has been enlarged. At the same time, it is planned to use the electric and hydraulic power sources and the signal lines necessary for it.

103

As in the past, the standard observation equipment and apparatus--such as CTDV, current-direction and current-velocity gauges, and the direction finder--are fixed in place.

3.6 Environment Control System

A comfortable living environment is maintained in the pressure hull by the addition of oxygen gas in proportion to the rate of oxygen consumption by the three crew members. Carbon dioxide is removed by lithium hydroxide. The environment maintenance capacity is designed for 9 hours of normal submerged activity and to reach 129 hours, including emergency breathing apparatus, in an emergency. Oxygen partial pressure, carbon dioxide partial pressure, and temperature and humidity are monitored through various measuring instruments. In determining and setting their proper values, the actual results obtained in the "Shinkai 2000" are put to practical use.

3.7 Acoustic Submerging System and Acoustic Observation System

Since the submersible cannot use standard radios while submerged, it must use underwater acoustic apparatus for such purposes as telephonic communication with the mother support ship, depth measurement and forward obstacle detection.

For echo sounding, this ship uses a synchronous pinger as the echo sounder transmitter and an LBL as the echo sounder receiver. Thus the submersible has its own means of position measurement in addition to the existing echo sounding (submersible's position information is provided by underwater telephone) by the mother support ship. In other words, by installing three transponders that respond to synchronous pinger sounds on the seabed as reference points the submersible's LBL detects the directions of their respective sound sources on different frequencies, thereby measuring its own position in real time and providing it on a graphics display on the control console's CRT.

Meanwhile, at the time of descent/ascent the altitude sonar/upward monitoring sonar are used together with the depth gauge to determine the vertical position of the ship. By using the altitude sonar, the altitude of the research submersible from the seabed can always be monitored on the CRT in a range of 1~1,000 meters.

The newly developed observation sonar unites the functions of a forward obstacle detection sonar represented by the existing CTFM system, etc. and of a tomography sonar, which detects the shape and the position of seabed objects at a relatively short distance like a television picture.

This sounder has a cross-linear array structure that combines a 48-ch transmission linear array and 64-ch reception linear array vertically and horizontally, respectively. According to the types of images to be taken, transmission and reception patterns receive scan control.

To acquire a front image (C mode), as shown in Figure 7, a thin fan beam that is wide horizontally and focused vertically is formed by the echo

104
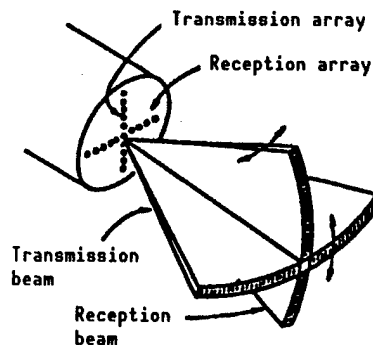
Figure 7. Fan Beam Scan by Cross-Linear Array

sounder transmitter array. The reflected signal from an object on this line is detected and decomposed by the reception fan beam, which focuses on a point in the horizontal direction and which is wide in the vertical direction and thin in the horizontal direction. By combining these transmission and reception beam scans, a front image having 48 x 64 picture pieces can be obtained.

Table 5. Perception Images by Observation Sonar

Item	Mode C mode Front image	B, BZ mode Horizontal section image	BV mode Vertical section image	PPI mode Horizontal section image	Descrip tion
1. Frequency	About 300 kHz	About 300 kHz	About 300 kHz	About 100 kHz	
2. [*1]Detection range	110 m	110 m	110 m	300 m	At TS= 0 dB
3. Angle of (H) visibility (V)	About ±20° About ±15°	About ±20° About ±15°[*4]	About ±20°[*2] About ±15°	About ±20°[*3] --	
4. Resolution (H) (V)	About 1.4° About 1.4°	About 1.4° About 1.4°	About 1.4° About 1.4°	About 10° About 25°	
5. Frame rate	0.4 F/S[*5]	3 F/S[*6]	0.4 F/S		

[*1] Noise level -44 dB or below (at 300 kHz ±10 kHz)
            -60 dB or below (100 kHz ± 5 kHz) ∴ 0 dB = 1 μb./Hz
[*2] Horizontal scan width
[*3] By mechanical scan
[*4] Vertical scan width
[*5] In the shortest distance
[*6] 1 F/S (BZ mode)

105

This same array composition also makes it possible to obtain a distance direction cross-sectional image (B, Ba, BV mode and PPI mode) of direction x distance similar to those produced by radar, medical ultrasonic diagnosis equipment, etc. This is accomplished by sending the fan beam in the designated direction (vertical, horizontal, depression angle, etc.), continuously sampling reflected signals form the object using the overall channels of the echo sounder receiver, and making a hologram (cross-sectional image) covering the designated range of distance from their phase lag and time delay. This sonar has three types of cross-sectional image modes--high resolution (about 300 kHz), low resolution (about 100 kHz) and combined direction. The details of these observation sonar image modes are shown in Table 5.

As described above, the observation sonar was developed to fill the functional gap between the optical system, which can cover only a short distance in the water, and the existing sonar, which is effective at long distances, but is not capable of shape recognition because of loose resolution. It is expected that this sonar will be effectively put to use, for example, in the process of accessing an object.

In order to guarantee the effective operation of the sounding equipment and apparatus, noise control by measuring and evaluating noises from the invertor, electric motor, etc., is being systematically carried out during the stages of design and construction. For each apparatus and unit that acts as a noise source, the noise spectrum level and frequency band are analyzed and measured. Efforts are underway to reduce equipment noise by selecting a piece of equipment only after it has been compared to other types and by improving its method of installation in the vessel.

3.8 Information Display and Data Recording

While submerged, the position and bearing, the operating condition of the main equipment, the standard observation data, etc., of the research submersible are monitored by the integrated information display system CRT located at the center of the console panel, and the principal data are automatically recorded by that system.

The integrated information display system has the following four modes for the display, and the crew can freely select and display them.

- Data display mode (power system, weight trim adjustment system information, etc.)

- Trim execution mode (nautical communication system information, etc.)

- Maneuvering mode (driving and control system, nautical communication system information, etc.)

- Inboard environment recording mode (environment control system information)

The data system of the "Shinkai 6500" consists of a data recording system, a video/photo-image system and data reproduction based on an integrated information display system.

The integrated information display system automatically records the principal data on a bubble cassette at fixed intervals (every 2 seconds). These data then become the attribute data for the observation data. The system will also record the display data upon request for recording from the touch screen.

Video information from the two television cameras and the sound image from the observation sonar of this vessel are recorded by two video units.

The data recorded on the bubble cassette in the integrated information display system are processed and reproduced on the form desired by researchers using the data reproducer arranged aboard the mother support ship. Further, the reproducer is provided with the ability to conduct data format conversion, etc., for linkage with the local area network (LAN) of the mother ship.

4. Reliability and Safety

The Safety Examination Committee evaluates and examines reliability and safety. It has also introduced and has promoted such techniques as FTA and FMEA since the first conceptual designs for the submersible were prepared. These evaluations and examinations are important not only in the stage of designing and construction but also in ensuring operational security. Thus it is planned to continuously push this practice hereafter.

The principal improvements for which measures have been taken in designing this vessel from the standpoint of securing safety and reliability are shown below.

- The main storage battery has been constructed using an independent two-group structure to improve its reliability.

- The release of the ballast weights is effected by a hydraulic actuator. As a backup, emergency abandonment bolt has been prepared. Further, to cope with a malfunction in the power unit, a fail-safe mechanism activated by a falling dead weight has been adopted as the actuator for the electromagnetic valve.

- In addition to ballast release to secure self-surfacing capability, measures have been taken to ensure emergency abandonment of heavy pieces of equipment, such as the manipulator, the sample container, and the payload.

- The emergency storage battery has been installed in the pressure hull. Thus, even in an emergency, environment maintenance and communication with the mother ship can be maintained for more than 129 hours.

- After designing the pressure hull and viewing window, and working out the inspection plan, the effect that material quality and the manufacturing process and capacity, etc., have on the vessel's reliability has been fully evaluated and assessed.

5. Conclusion

The "Shinkai 6500" is a deep-sea research submersible that literally leads the world, even from the simple standpoint of maximum submersible depth. The realization of this research submersible would have been impossible without the development and refinement of deep-sea technology backed by the achievements in the design, construction and operation of the "Shinkai 2000."

In May of this year (1988), the schedule calls for complete pressure leakage testing of the vessel's pressure hull at the U.S. (David Taylor) Research Center and starting the process of installing it on the ship. In 1989, the ship is scheduled to complete real sea trials at the 6,500-meter depth, after which it will be delivered to the Japan Marine Science and Technology Center. This vessel is expected to produce many satisfactory results in ocean research thereafter.

Mutsu's Reactor Vessel Being Overhauled; Sea Voyage in 2 Years

43062031a Tokyo GENSHIRYOKU SANGYO SHIMBUN in Japanese 10 Nov 88 p 1

[Text] On 4 Nov the Japan Atomic Energy Research Institute began an open-lid overhaul of the nuclear reactor vessel aboard the nuclear-powered Mutsu. This is the first overhaul of the reactor since the fuel assembly was charged six-teen years ago, in 1972. By early December all the equipment in the reactor is to be removed, inspected, and serviced, and next year the power is to be increased and the ship is to undergo sea trials, with an experimental year-long voyage planned for two years from now.

The work of opening the reactor's lid began at 10:10 a.m., and it took all morning to remove it and attach it to a dockside crane in preparation for bringing it off the ship.

The work of lifting it out of the ship began at 1:35 p.m. After 2:00 it was loaded onto a trailer, and at 3:50 it was safely brought into a fuel and waste materials handling building about 800 m away.

By early December the fuel assembly, control rods, and fixtures inside the reactor will be removed one by one and transferred to a materials and waste water management building and to inside the fuel and waste materials handling yard.

The various equipment that is removed will be inspected and serviced, includ-ing a leakage inspection using helium gas.

Meanwhile, aboard the Mutsu the steam generator and pressurizer will be over-hauled and serviced, the reactor vessel walls and primary cooling system pipes will be inspected and serviced, and the primary cooling system will be flushed out.

The Mutsu sailed into its new home port of Sekinehama on 26 Jan 1988, and since February 1 the main systems and equipment of its reactor have been undergoing functional testing. This inspection has confirmed that the machin-ery and equipment is in good condition.

New SOR Light Source Developed for Tristan Accelerator

43062031c Tokyo GENSHIRYOKU SANGYO SHIMBUN in Japanese 10 Nov 88 p 2

[Text] The Institute of High-energy Physics of the Ministry of Education announced on 31 October that it has generated circularly polarized x-rays with its newly developed "circularly polarized x-ray wiggler-undulator," which will serve as a new light source for optical radiation (SOR) research.

Since fiscal 1987 the institute has been working on a three-year project to develop an x-ray insertion light source for increased brightness for the Tristan accelerator, which causes electrons and positrons to collide. The plan calls for construction of two insertion-type light sources in the impingement build-up ring. One of these has now been completed, marking the first time in the world that circularly polarized x-rays have been generated.

Circularly polarized light, in which the plane of oscillation of a light wave rotates once for every wavelength, is an important means for investigating the magnetic properties of substances.

With visible light, circular polarization is easy to achieve, but it is difficult to determine the absorption spectrum for substances which light does not pass through. A circularly polarized x-ray source would work with any kind of substance, but until now no satisfactory circularly polarized x-ray source has been available.

To overcome this problem, the institute has developed a wiggler-undulator for generating circularly polarized light. In this device 41 poles are arranged above, below, and to the right and left of each permanent magnet with an 8-cm gap (the period of the magnetic field is 16 cm). Electrons passing through this device at nearly the speed of light generate circularly polarized light describing a helical path when the surrounding magnetic fields are equal; when they are not, what is generated is elliptically polarized light containing both circularly and linearly polarized light describing a distorted helical path.

A feature of this device is that the wavelength and state of polarization of the generated x-rays can be varied by controlling the surrounding magnetic fields. When the magnetic fields above and below are reduced in intensity, the resulting wavelength is in the soft x-ray region, and the generated soft x-rays can, by interference, produce a very high brightness (undulator mode).

When the institute installed this wiggler-undulator in the impingement buildup ring and conducted tests at an electron energy of 6 GeV, it achieved completely circularly polarized light in the soft x-ray range (200-2,000 electron volts) and elliptically polarized light in the x-ray range (2,000-100,000 electron volts). Moreover, the brightness was found to be 100-2,000 times as intense as that of optical radiation produced with polarization electromagnets.

Long-Term Strategy in Group Separation & Extinction Research (Part 2)

43062031d Tokyo GENSHIRYOKU SANGYO SHIMBUN in Japanese 10 Nov 88 p 6

[Text] Continuing from the previous issue, this article presents an overview
of the Long-range Plan for Development of Group Separation and Extinction
Treatment Technology drawn up by the Japan Atomic Energy Commission's special
committee on the disposal of radioactive wastes.

Research and Development in Extinction Using Atomic Reactors

Fast Breeder Reactor Extinction

Phase I (until about 1992): The extinction characteristics of TRU in fast
breeder reactors will be evaluated, and concepts will be clarified concerning
the characteristics of reactor cores using TRU nuclide mixed fuels and large
fast breeder reactor cores suitable for TRU nuclide extinction treatment.

MOX fuel will be the main fuel for TRU nuclide extinction, but other ceramic
and metal fuels will also be studied.

In the Joyo, testing will begin involving the irradiation of fuel samples for
TRU nuclide extinction, and irradiation tests will be carried out on MOX fuels
with which TRU nuclides are mixed. Basic tests will also be conducted con-
cerning the compounding of fuels with TRU nuclides obtained by group separa-
tion. This will be reflected in the compounding of fuels for single fuel
combustion fast reactors.

In addition, uranium-plutonium metal fuels with TRU nuclide as an additive
will be made, and their fundamental worth as fuels will be evaluated by inves-
tigating their basic properties. An extinction analysis system will be devel-
oped for evaluating the reactor core characteristics of metal fuel reactor
core fast breeder reactors and their extinction characteristics by which fuels
are transformed into nuclides having a short halflife.

Phase II (1993-2000): Conceptual design will be done on TRU extinction large-
size reactor cores for fast breeder reactors, and their suitability for the
Joyo, Monju, and others will be evaluated, taking into consideration the
results of the irradiation tests conducted with the Joyo. Ways will be
devised to use MOX fuels in which TRU nuclides are mixed. There will also be
a study of the basic properties of fuels blended with TRU nuclides other than
MOX fuels. For example, irradiation tests and post-irradiation tests will be
done on metal fuels as well, optimum methods for the extinction of TRU

114

nuclides in metal-fuel fast breeder reactors will be studied, and the results of this investigation will be incorporated in design research for single fuel combustion fast reactors.

Charging tests will be conducted in the Joyo based on the results of this testing and research.

Beginning in 2001 testing will be carried out involving the charging of fast breeder reactors with MOX fuels to which TRU nuclides have been added, and their cycle will be studied with a view toward practical application. There will also be verification testing for the recycling of fuels for the extinction treatment of TRU nuclides in the metal fuel cycle.

Single Fuel Combustion Fast Reactors

With a TRU nuclide, at a neutron energy level of 1 MeV or more the nuclear fission cross-sectional area becomes greater than the neutron absorption cross-sectional area, and the probability of fission increases. Thus if it becomes possible to devise a single fuel combustion fast reactor, that is, a fast reactor which consists of only TRU nuclides, then the high-efficiency extinction of TRU nuclides will become possible, and by building a recycling plant integrated with a single fuel combustion fast reactor, transport would no longer be necessary and the TRU nuclides could all be sealed into the same facility.

Fast breeder reactor technology is the groundwork for developing single fuel combustion fast reactors, but what is urgently needed are a better understanding of the nuclear properties based on more complete physical data on reactors, the manufacture of TRU fuels, and the acquisition of data on irradiation properties. The construction of an experimental reactor will also be considered for purposes of the final evaluation.

Phase I (until 1996): This is the phase during which basic testing will be carried out concerning technical feasibility. Design research will be done for the reactor core and plant of single fuel combustion fast reactors, and technical topics will be specified.

Tests involving the irradiation of samples will be conducted in order to obtain physical data on reactors using TRU fuels, as well as data on physical properties.

Also, work will begin on developing a cost-benefit analysis method for the introduction of TRU extinction treatment systems.

Phase II (1997-2000): This is the phase during which technical feasibility will be verified. This includes preliminary study of single fuel combustion fast reactors for practical use and the preliminary design of experimental reactors. In fast critical assembly, nuclear data verification experiments will be carried out, as well as basic experiments on fuel irradiation in fast breeder reactors. In addition, preliminary engineering tests will be conducted concerning the preparation of fuels with TRU nuclides.

A cost-benefit analysis for the introduction of TRU extinction treatment systems will also be made.

Beginning in 2001 is the stage when system feasibility is to be verified. Following conceptual design of an experimental reactor, detailed designs are to be made, and the experimental reactor is to be built.

To verify the nuclear characteristics of the experimental reactor and other equipment, critical experiments, fuel irradiation engineering experiments, and fuel preparation engineering experiments will be carried out. Based on this research and development, the effects of the introduction of TRU nuclide extinction treatment systems will be evaluated.

Research and Development in Extinction Technology Using Accelerators

An accelerator can control a nuclear reaction more freely and safely than an atomic reactor because an accelerator can vary the energy of the accelerated particles and the intensity of their pencil of lines, and because an accelerator presents no critical problems. In addition, an accelerator can focus a stream of particles more intensely, which promises to provide fast extinction treatment. Moreover, accelerators could further increase the efficiency of extinction treatment by such means as making use of the neutrons which are produced when an accelerator is used for extinction treatment.

Proton Accelerators

When a TRU nuclide is bombarded with high-energy protons, the nucleus undergoes spallation, transforming the TRU nuclide into short-halflife nuclides or non-radioactive nuclides.

With this extinction method it is possible in principle to increase the extent of the transformation, and since no critical reactor is used, there are few safety or other restrictions. Moreover, the electric power needed for accelerating the protons could be self-supplied by a hybrid system in which the neutrons generated when nuclei are split help drive subcritical reactors arranged around the target. Further topics with respect to the efficiency of the nuclear spallation are the strengthening of experiments to achieve a higher likelihood of nuclear spallation, and the development of technology for high-output proton accelerators able to handle waste products in large quantity.

Phase I (until 1992): In this stage, feasibility in principle is to be verified. Code for the computer simulation of nuclear spallation and particle transport will be developed, and a basic study of extinction treatment plants will be carried out.

As research into target systems, medium-scale physical experiments will be conducted using lead and uranium systems in order to examine the general appropriateness of nuclear spallation performance predictions based on these computer simulations.

Meanwhile, a basic study of proton accelerators will be made, and a start will be made on developing technology for accelerators with higher current and higher energy.

Phase II (1993-2000): Proving engineering feasibility will be the goal of this stage. Computer code for nuclear heat and structural design will be prepared, and conceptual design of extinction treatment plants will be done.

In addition, physical experiments will be conducted on large-scale reactors using uranium systems for the purpose of verifying predictive accuracy concerning nuclear spallation characteristics of extinction treatment plants. Also, nuclear data for the nuclear spallation energy range (MeV-GeV) will be collected and acquired.

With regard to accelerators, the above reactor physical experiment and reactor physical data will be obtained, and in order to carry out the experiments scheduled for the subsequent phase a proton accelerator in the 10 mA, 1.5 GeV class will be built.

Also, study will be given to a proton accelerator for practical plants in the 300 mA, 1.5 GeV class.

Beginning in 2001 will be the phase for establishing the feasibility of systems, including their economic feasibility. This will involve the optimal design of extinction treatment plants as well as applications research including the evaluation of nuclear spallation efficiency, energy balance, and other plant performance criteria.

Pilot-scale tests will be conducted with targets consisting mainly of uranium, the nuclear spallation performance of TRU fuels and the radioactive substances which are generated as a by-product will be evaluated, and engineering test data will be collected on heat characteristics and the irradiation characteristics of fuels and materials.

Based on these engineering tests, an evaluation will be made of the technical feasibility of extinction treatment plants of practical size.

In the area of accelerators, technology will be developed for high-output accelerators in the 300 mA, 1.5 GeV class suitable for practical plants.

All this research and development will be the basis for an evaluation of the effects of introducing TRU extinction treatment systems which use accelerators.

Electron Accelerators

The method of extinction treatment by electron accelerator is a technology which makes use of the photonuclear reaction. Since all it does is add high-energy gamma rays to the treatment system, this method generates little secondary radiation. Research concerning this method will include a wide range of nuclides, including TRU nuclides, cesium, and strontium.

The development of technology for the electron accelerators used to generate gamma rays is progressing even for devices on the industrial level, and the groundwork is being laid for the development of accelerators having the required large electrical current.

Ways are to be devised to effectively utilize the neutrons which are released in the photonuclear reaction, and it is expected that the power needed for accelerating the electrons can be self-supplied by driving subcritical reactors positioned around the target.

In order to develop high-current electron accelerators, practical extinction treatment methods using electron accelerators are to be devised through theoretical and experimental research involving beam stabilization.

Phase I (until 1992): This is the stage of comprehensive basic testing and research. It will involve the development of computer code for the transport and heat of electron, gamma, and neutron rays within extinction treatment systems, and basic study of extinction treatment plants.

In target system research, basics tests will be performed using existing accelerators in order to obtain physical data on reactors.

In addition, technology will be developed for beam stabilization and other factors which are most important for looking into the possibility of creating high-current accelerators.

Phase II (1993-2000): In order to verify engineering feasibility, engineering tests will be carried out to prepare computer code for nuclear heat and structural design using research accelerators for the 100 mA, 100 MeV class. In addition, conceptual and detailed designs will be worked out for extinction treatment plants.

Beginning in 2001, pilot-scale extinction treatment tests will be carried out using electron accelerators in the 1 A, 100 MeV class.

Fig. 1   Schedule for Research and Development of Extinction
         Treatment Technology Using Atomic Reactors
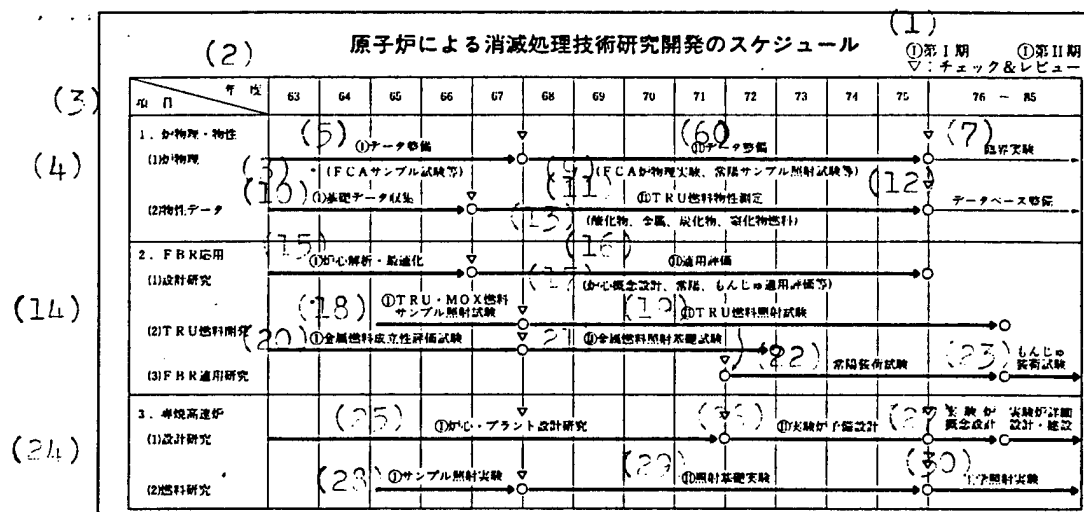
Key to Figure 1:

1. (I) Phase I   (II) Phase II
   <triangle>: Check and Review
2. Year [add 1925 to the number shown]
3. Item
4. 1. Reactor physics, physical properties
   (1) Reactor physics
   (2) Physical properties data
5. (I) Data preparation
6. (II) Data preparation
7. Critical experiments
8. Fast Critical Assembly sample testing, etc.
9. Fast Critical Assembly physical tests,
   Joyo sample irradiation tests, etc.
10. (I) Collection of basic data
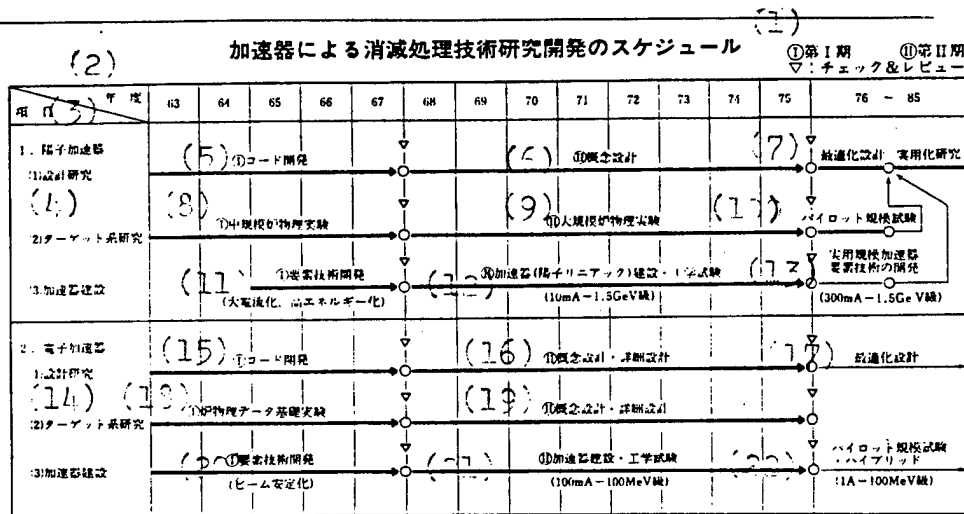11. (II) Measurement of physical properties of TRU fuels
12. Preparation of database
13. (Oxide, metal, carbide, nitride fuels)
14. 2. Fast Breeder Reactor applications
    (1) Design research
    (2) Development of TRU fuels
    (3) Fast Breeder Reactor applications research
15. (I) Reactor core analysis and optimization
16. (II) Applicability evaluation
17. Conceptual design of reactor core,
    evaluation of Joyo, Monju applicability, etc.
18. (I) TRU, MOX fuel sample irradiation tests
19. (II) TRU fuel irradiation tests
20. (I) Tests for evaluating the feasibility of metal fuels
21. (II) Basic tests involving the irradiation of metal fuels
22. Joyo charging tests
23. Monju charging tests
24. 3. Single fuel combustion fast reactors
    (1) Design research
    (2) Fuel research
25. (I) Core reactor and plant design research
26. (II) Preliminary design of experimental reactor
27. Conceptual design of   Detailed design and construction of
    experimental reactor   experimental reactor
28. (I) Sample irradiation experiments
29. (II) Basic irradiation experiments
30. Engineering irradiation experiments

Fig. 2 Schedule for Research and Development of Extinction
Treatment Technology Using Accelerators

Key to Figure 2:

1. (I) Phase I   (II) Phase II
    <triangle>: Check and Review
2. Year [add 1925 to the number shown]
3. Item
4. 1. Proton accelerators
    (1) Design research
    (2) Target system research
    (3) Accelerator construction
5. (I) Development of computer code
6. (II) Conceptual design
7. Optimization design   Applications research
8. (I) Medium-scale reactor physical experiments
9. (II) Large-scale reactor physical experiments
10. Pilot-scale tests
11. (I) Development of constituent technology
    (for higher electrical current, higher energy)
12. (II) Construction of and engineering tests on accelerator
    (proton Lineac) (10 mA, 1.5 GeV class)
13. Development of constituent technology
    for practical-scale accelerators
    (300 mA, 1.5 GeV class)
14. 2. Electron accelerators
    (1) Design research
    (2) Target system research
    (3) Accelerator construction
15. (I) Development of computer code
16. (II) Conceptual design, detailed design
17. Optimization design
18. (I) Reactor physical data basic experiments
19. (II) Conceptual design, detailed design
20. (I) Development of constituent
    technology (beam stabilization^@)
21. (II) Construction of accelerator,
    engineering tests (100 mA, 100MeV
    class)
22. Pilot-scale tests, hybrid
    (1 A, 100 MeV class)

Engineering Safety of Nuclear Power Plants

43062020 Tokyo PUROMETEUSU in Japanese Dec 88 pp 38-46

[Article by Kunihisa Hayata, chief, Process Safety Research Section, Fuel Safety Engineering Division, Tokai Laboratory, Japan Atomic Energy Research Institute: "Engineering Safety Research"]

[Excerpt] 1. Conception of Safety

The power generating atomic reactor generates power using the large amount of heat generated in the fission of nuclear fuel. Heat is converted into electricity in the same manner as at an ordinary thermal power plant, namely, by generating steam from heat and generating electricity via the steam turbine generator. But nuclear power generation differs from thermal power generation using petroleum or coal in that radioactive rays are produced by fission and fission products are radioactive. Therefore, it is essential to design the reactor so that the level of radioactive rays does not exceed the prescribed value so as to prevent them from affecting workers and local inhabitants. Strict radiation control of the atomic power plant is aimed at preventing the effects of radiation on workers and local inhabitants.

Thus, the reactor is provided with some protective barriers lest the radiation effects should reach the environment. Figure 1 shows these protective barriers. In normal operation, the radioactive material in the fuel is enclosed in the fuel pellet and the fuel tube which contain the fuel. This fuel tube forms the first protective barrier. The pressure boundary composed of a pressure vessel and piping so as to prevent fission products (FP) from escaping into the environment in the event of damage to the tube forms the second protective barrier. The radioactive material coming out of the pressure boundary with water in the reactor is kept in the container, which is the third protective barrier. Thus, it is a safety design that should an accident occur, it may be possible to prevent the radioactive material from escaping into the environment by multiple protective barriers and thereby avoid the spread of the accident and contain it safely.

Fuel rod: It is a rod
formed by filling nuclear
fuel pellets in a
tube.

First barrier: nuclear
fuel pellet. Usually
most radioactive material
is kept in pellets.

Third barrier: reactor
pressure vessel

Second barrier:
tube

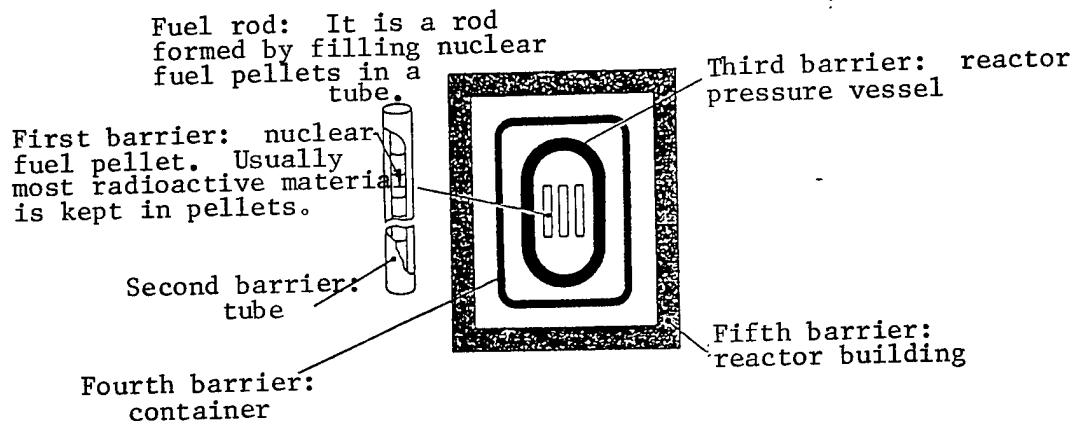Fifth barrier:
reactor building

Fourth barrier:
container

Figure 1. Multiple Protective Barriers of Reactor

In designing a reactor, it is necessary to assume the occurrence of
extraordinary events and accidents and always be able to stop the reactor
safely and keep the impact of radiation below the design level. Accidents
thus assumed are called design basis accidents. These accidents are
assumed in order to maintain the safety of the reactor even if an accident—
most unlikely in the common sense of engineering—should occur. Needless
to say, preventing accidents is most important to assure the safety of
reactors.

Many studies have been done to prove that the function of the "multiple
protective barriers" can be maintained when a design basis accident occurs.
In particular there have been many tests and analyses on LOCA (loss of coolant
accident) in which the reactor's cooling water is lost and RIA (reactivity
initiated accident) in which the control rod suddenly comes out or falls
off by such facilities as the Japan Atomic Energy Research Institute and
the results are reflected in safety reviews. Furthermore, studies on
"severe accidents," worse than design basis accidents, are being conducted
to show the margin of safety of the reactor.

These studies are known by the general name of "engineering safety
research" because they mainly comprise tests to show the effectiveness
of engineering safety facilities of the reactor and are central to the
safety research for Japanese reactors. Here, we shall look at studies on
safety against LOCA, RIA and "severe accidents" included among the
engineering safety research of the past.

2. Research on Safety Against LOCA (Loss of Coolant Accident)

2.1. LOCA and TMI-2 Accident

In assessing the safety of a light water reactor, LOCA by the rupture of
primary coolant system piping is assumed as a design basis accident.
Reactor facilities are provided with various safety devices and, when

assuming accidents, care is exercised to minimize the risk of inflicting radiation on the local general public.

ECCS (emergency core cooling system) is one of these safety devices and is used to make up for the cooling water lost in a LOCA by injecting cooling water into the primary coolant system, minimize melting or damage that may be caused by the overheating of fuel and maintain the fuel in a form that permits cooling. Since ECCS is, indeed, important to maintaining the safety of reactor facilities, it is necessary to grasp its effectiveness and the effects of various factors on it pragmatically and quantitatively, understand clearly what an ECCS accident is like, and conduct a quantitative analysis of the margin of safety.

The importance of more deeply understanding hydrothermal dynamics during not only a major rupture LOCA but also a minor rupture LOCA and clarifying the combination of conditions and the process leading to the deterioration of the core and eventually its damage has now been recognized.

Consequently, studies have expanded to include minor rupture LOCAs in addition to major rupture LOCAs.

2.2 ROSA Plan Research and Results

LOCA studies are also being conducted in the United States, West Germany, France, etc. but the Japan Atomic Energy Research Institute has long conducted tests and research on the effectiveness of ECCS since fiscal 1970 under the name of ROSA (Rig-of-Safety Assessment) Plan and steadily amassed results. In the initial ROSA-I Plan, studies were concerned with the dynamic load exerted against the structural materials when high-pressure, high-temperature water was discharged from a pressure vessel and the amount of discharged water. In the next ROSA-II Plan, the effectiveness of ECCS was proved by investigating the hydrothermal dynamics of the coolant from the beginning of LOCA to its end, using a scale model of PWR (pressurized water reactor). Under the ROSA-III Plan, research to clarify the dynamics of the coolant during a LOCA and test the effectiveness of ECCS was conducted for BWR (boiling water reactor).

From the lesson of the TMI-2 accident, the ROSA-III Plan also incorporated research on subjects expanded from major rupture LOCA to minor rupture LOCA. Then, the ROSA-IV Plan was started from fiscal 1980 for the purpose of studying the minor rupture LOCA of PWR.

Here, we shall see the main results of the ROSA-III Plan and outline the past results of the current ROSA-IV Plan.

(1) Main Results of ROSA-III Plan

A total of 118 tests, shown in Table 1, were conducted in the ROSA-III Plan, using a 1/424 scale model of BWR. Figure 2 shows typical results from these tests. It assumes the failure of the high pressure core spray system in ECCS and shows the relationship between rupture area and

PCT (peak cladding temperature) obtained from an experiment conducted by
variously changing rupture area from 200 percent (equivalent to rupture
at both ends of the recycling piping) to 0 percent. In all tests, the core
was exposed to steam and fuel rod temperature rise as the coolant flowed
out. However, after the operation of ECCS, the core was submerged again
and the fuel rod was quenched. As is clear from the chart, PCT is somewhat
lower than 1,473 K, the safety standard value, and ECCS has a great margin
of safety.

Table 1. ROSA-III General Test Series

(1)	Standard major rupture test series	(13 tests)
(2)	Single failure major rupture test series	(4 tests)
(3)	Minor rupture test series	(17 tests)
(4)	Rupture area parameter test series	(10 tests)
(5)	Both end rupture test series	(15 tests)
(6)	Recycle pump outlet side piping rupture test series	(3 tests)
(7)	Steam system piping rupture test series	(6 tests)
(8)	High pressure core spray system piping rupture simulation test series	(2 tests)
(9)	Minor rupture sensitivity test series	(18 tests)

Total general tests: 88 tests
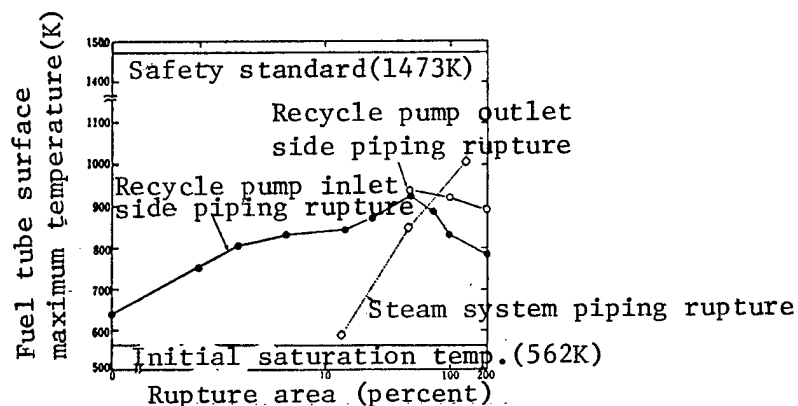Natural cycle tests: 30 tests

Figure 2. Relationship Between Fuel Tube Surface Maximum Temperature and
Rupture Area in ROSA-III Test Assuming Failure of High Pressure
Core Spray System

From these tests, the following became clear:

1) PCT is closely related to the time when core exposure starts and how long the period of exposure lasts. In the event of pipe rupture on the inlet side of the recycle pump, therefore, PCT was not necessarily maximum even if the pipe has maximum rupture area; instead, it was maximum when it has 50 percent rupture area.

2) In the event of pipe rupture on the outlet side of the recycle pump, the actual rupture area is confined because there are contractions of area in the jet pump and the recycle pump (it corresponds to 72 percent of the pipe cross-sectional area). So, in the case of a rupture area exceeding 72 percent, PCT is higher than pipe rupture on the inlet side of a recycle pump with the same bore diameter. In the case of 72 percent or smaller rupture area, it is the same as in the event of pipe rupture on the inlet side of a recycle pump.

3) Where there are pipe rupture in the steam system, the aforementioned ECCS failure, and the failure of ECCS caused by a high container pressure, the infusion of cooling water from ECCS will be delayed because of the slow lowering of the water level of the downcomer which is responsible for triggering the ECCS start signals. In the event of large diameter rupture, PCT is higher than that of rupture in the recycle system.

(2)   Past Results of ROSA-IV Plan

Under the ROSA-IV Plan, we have been conducting minor rupture LOCA tests on PWR since fiscal 1985, using an LSTF device having the same height as PWR and a volume ratio scale reduced to 1/48. So far, a total of 40 tests have been conducted including tests with varied rupture positions and size and core cooling tests by natural environments. Of these, we shall see the characteristic phenomena in the case of cold-leg [phonetic] rupture.

Figure 3 and Figure 4 show the core water level and the fuel rod temperature change in the cold-leg 5 percent rupture test. In Figure 3, the core water level temporarily lowered in spite of the fact that, at about 140 seconds, there was sufficient coolant in the primary system and, as the result, the fuel rod temperature temprarily rose, as indicated in Figure 4. These processes were brought about by the time change of coolant distribution in the primary system, as indicated in Figure 5. Rupture causes coolant outflow but, since the rupture is small, the coolant decreases relatively slowly and the system is filled from top down with steam generated in the core (at about 120 seconds in Figure 5). Later, in the process until water in the loopseal is completely discharged, the water level in the core lowers to the bottom end of the loopseal by the manometric pressure balance between the loopseal and the core. But at this point, steam generated in the core flows into the steam generator, as indicated by the behavior at about 140 seconds in Figure 5; thus, more coolant is kept in the inlet part of the steam generator and on the capillary upflow side than on the downflow side. As a result, this water head and also the core water level are pushed down. Later, when water is discharged from the loopseal part, a

steam discharge route forms from the core to the loopseal part and to the rupture and the core water level returns to its original state. At all rupture bore diameters, core exposure is transient, as indicated in Figure 4, and the rise of fuel rod temperature is about 100 K, at most. The results of computation by the safety assessment analysis code (RELAP5/MOD2) are shown in the chart for reference.
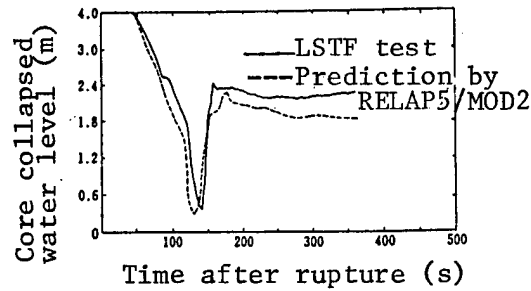

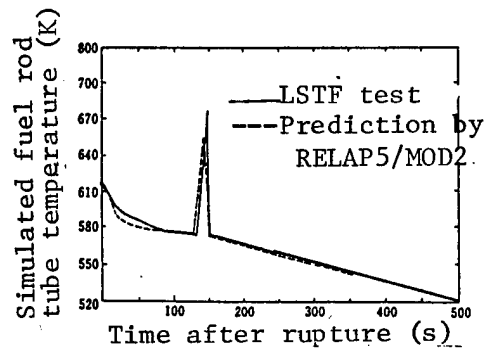Figure 3.   Transient Change of Core Collapsed Water Level

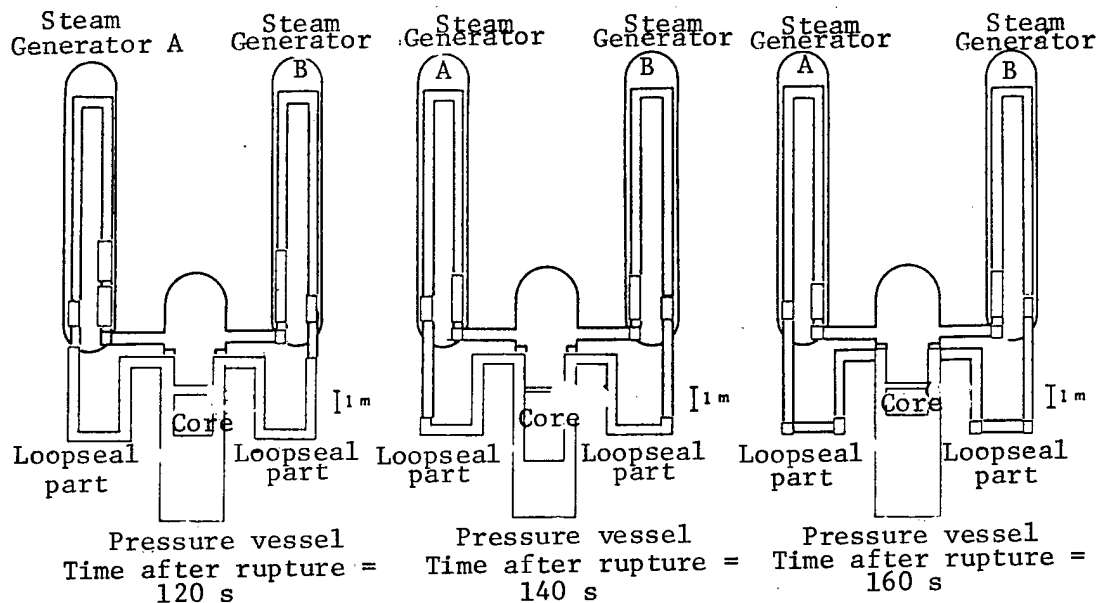Figure 4.   Simulated Fuel Rod Tube Temperature Response

Figure 5. Water Distribution in
Primary System at 5 Percent Cold-leg Rupture

3. Research on Safety Against RIA (Reactivity Initiated Accidents)

3.1 Chernobyl Accident and RIA of Light Water Reactors

A reactor is operated by adjusting reactivity so that fission reaction may
always be kept constantly stabilized. But if a great reactivity is suddenly
exerted against the reactor somehow, its output increases abnormally to
cause a runaway, as it were. This is the accident called RIA (reactivity
initiated accident).

RIA suddenly became known after the unfortunate Chernobyl accident. One
of the major causes of this accident is the characteristic of instability,
namely, in a reactor of this type, output increases more and more as
boiling occurs in the core if it is operated at a low output. The accident
happened because experimental operation was enforced, using low output
in disregard of this characteristic and, moreover, turning off various
safety devices.

The BWR or PWR used for power generation in Japan has the characteristic
of lowering output if boiling starts in the core. Therefore, if boiling
starts or intensifies as reactor output increases somehow, output increase
is automatically suppressed and there can be no reactor runaway as in the
Chernobyl accident.

127

The worst conceivable RIA with light water reactors is an accident in which the control rod draws quickly out of the core. The control rod is an absorber of neutrons. Neutrons are absorbed and fission stops when the rod is inserted into the reactor. Inversely, fission becomes active and output increases when the rod is extracted. Thus, the control rod functions like the brakes and the accelerator of an automobile. The more quickly it comes off, the greater the output that is generated. So, in the safety review of the government, the most severe situation assumed for PWR, for example, is the exceedingly severe accident involving the bolt-out of the control rod from the core by the high pressure of the reactor container due to damage to the control rod drive attachment (this is called control rod escape accident) and a reactor must be designed so that its core may not be damaged in the event of an RIA.

3.2 Research on RIA and Results

Research on RIA was started in the United States toward the end of the 1950's and a series of reactor runaway tests including the BORAX, SPERT and PBF tests was conducted in a desert. In Japan, research on RIA was started by the Japan Atomic Energy Research Institute in 1972 as an NSRR test project and so far, about 870 tests, or much more than the above-mentioned U.S. tests, have been conducted, using real light water reactor fuel as test fuel.

In a reactivity accident, a great runaway-caused output develops within the extremely short period of less than a second. So, in an NSRR test, NSRR, a research reactor capable, though briefly, of generating a very large output about seven times the output of an 11 million-KWe power reactor is used and a runaway output simulating RIA is generated in a test fuel hermitically sealed in a strongly built experimental capsule of stainless steel contained in an experimental hole of this reactor. Photo 1 [not reproduced] shows how the reactor NSRR looks when operating. The periphery of the reactor can be seen through the deep layer of cooling water to shine in beautiful blue as the cooling water becomes luminous due to strong radiation (Cerenkov phenomenon).

Photo 2 compares the after-test external appearance of a test fuel in the case that the amount of heat generating by the fuel is gradually increased. The number of calories generated per gram of fuel (fuel enthalpy...cal/gUO$_2$) is used as the unit of the amount of heat generated. The external appearance of the fuel rod does not change at fuel enthalpies of less than 88 cal/gUO$_2$. But if the fuel enthalpy is 110 cal/gUO$_2$ or over, the maximum temperature of the fuel tube exceeds 800°C and the surface of the tube becomes oxidated. The amount of oxidation of the fuel tube increases with the rise of fuel enthalpy and, when the fuel enthalpy exceeds about 220 cal/gUO$_2$, cracks develop in the fuel tube having been oxidated and become brittle and the fuel is damaged. When the fuel enthalpy exceeds 325 cal/gUO$_2$, the melted fuel is dispersed throughout the coolant in the form of fine particles and rapidly heats the coolant with the result that "steam explosion" occurs. In the Chernobyl accident, the fuel enthalpy reportedly topped

300 cal/gUO$_2$ on the average. It is, therefore, presumed that, in the center of the core where the amount of heat generated is still higher, such atomization of fuel occurred to destroy the core.

cal/g.UO$_2$

350
300
250
200
150
100
50
0

Fuel enthalpy

(325)
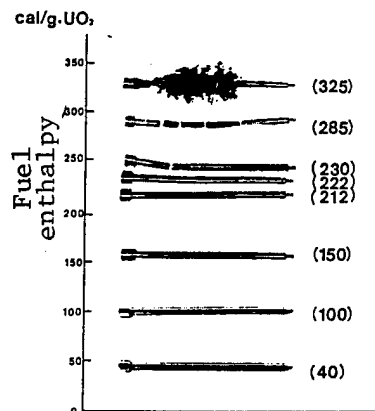(285)
(230)
(222)
(212)
(150)
(100)
(40)

Photo 2.　Results of NSRR Test

In the NSRR experiment, the conditions and mechanism of fuel failure were also studied in detail, changing fuel types and cooling conditions variously, and furthermore, research was made as to how defective fuels, such as fuel rod in water, or fuel infiltrated by coolant, behaved in an accident.

3.3 Safety Measures Against RIA

What must first be done when an abnormal output increase is caused by the exertion of reactivity is to quickly detect the abnormalcy and stop the reactor. Therefore, the reactor is provided with many detectors for output, pressure, temperature, etc. as well as protective equipment designed for an emergency stop upon detection of an abnormalcy. Thus, fuel failure can be prevented by an emergency stop in the event of an abnormalcy caused by the relatively slow exertion of reactivity, e.g., the continuous draw of control rods due to the breakdown of equipment during an output operation. But in the case of extremely severe accidents, such as control rod escape assumed in the safety review, the output of the reactor increases so rapidly that the runaway output cannot be suppressed by inserting control rods. For these severe reactivity accidents, therefore, it is necessary to design the reactor system so as not to incur core destruction, should such an accident occur.

Under these circumstances, standards for assessing safety design against reactivity accidents were set in 1984 as a guideline of the Atomic Energy Safety Committee in accordance with the various findings obtained from the abovementioned NSRR tests. It was about four years before the Chernobyl accident. This guideline requires that no fuel failure be caused by an abnormal phenomenon that may occur from an error in operation or the breakdown of a single piece of equipment and the fuel enthalpy to be used as the allowable design limit for this purpose was set on the basis of NSRR test results as indicated in Figure 6. For control rod escape and other least likely accidents, core damage must be prevented by a design

with a fuel enthalpy not exceeding 230 cal/gUO$_2$. The guideline also
requires assessment for fuel rod in water that may exist in the core by
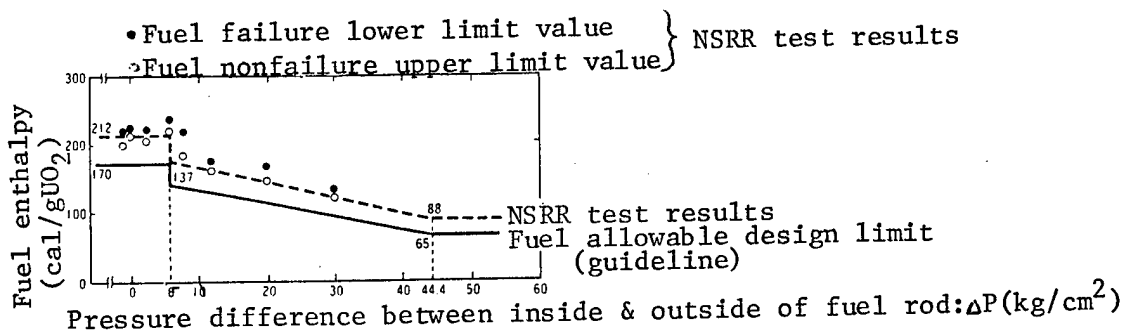a very small proportion.

Figure 6. Fuel Allowable Design Limit and NSRR Test Results

The above safety standards, when first set, were unique in the world and
stricter than the standards in the United States, which was a forerunner
in atomic energy. After the Chernobyl accident, various countries began
to improve their standards against reactivity accidents and the above-
mentioned Japanese standards have been used in many countries as the best
model for this purpose. Moreover, preparations are being made to test
fuels of which the combustion has progressed by the use of NSRR and this
fact is attracting attention. Thus, it can be said that Japan now leads
the world regarding research on safety against reactivity accidents.

4. Research on Safety Against Severe Accidents

4.1 Purpose of Research

As stated, a reactor is designed so that it can be safe even against the
least likely accidents assumed as design basis accidents. At an atomic
power plant, abnormalities in instruments and equipment can be readily
detected and the reactor can be stopped safely. At the same time, efforts
are being made to prevent the occurrence of abnormalities by strict routine
operation control, inspection and maintenance work. It is, therefore,
considered that the probability of occurrence of accidents is extremely low.

But if an accident should occur and the equipment failed to operate
according to design, what would happen? Also, if an instrument is out of
order or if an operator operated it erroneously, what would happen? In
the TMI-2 and Chernobyl accidents, the grave consequences were the results
of accumulation of human errors rather than the breakdown of equipment.
Accidents in which reactors are heavily damaged because instruments or
equipment assumed for design basis accidents do not operate according to
design or are operated erroneously are called severe accidents for the
reason that the cores are exposed to severe conditions as the result of
the accidents.

130

Design basis accidents are, in themselves, selected with sufficient margin of safety to ensure the safety of the reactor and, therefore, even in a state beyond the level of design basis accidents, the core is not immediately reduced to a severe condition. This means that a reactor designed on the assumption of design basis accidents is sufficiently safe against severe accidents. The purpose of research on safety against severe accidents is to clarify this margin of safety of reactors and explain that, even in a state beyond the design criteria, the safety of the reactor is not immediately impaired and thus, the selection of design basis accidents is appropriate.

4.2 Research on Severe Accidents and Results

Research on severe accidents has been conducted in many countries. This research is characterized by the fact that, because of the large scale of many tests involved, there is active international cooperation among the atomic energy developing nations in conducting the research.

The subjects of study concerning severe accidents is diverse, as indicated in Figure 7. The most important of these subjects is the process of fuel damage and a related test is being conducted in the United States, using a research reactor, as an international cooperation study in which 12 nations, including Japan, participated. In a severe accident, the main fuel tube is damaged by the rise of temperature of the fuel because the heat of the fuel cannot be completely eliminated. In the TMI-2 accident, for example, the core was greatly damaged, as in Figure 8, because of the loss of the coolant in the core. But finally, the discharge of radioactive material into the environment was almost negligible because the soundness of the pressure vessel, the second protective barrier, and the soundness of the container, the third protective barrier, were assured. So, fuel damage tests simulating the conditions of the TMI-2 accident were conducted, using such facilities as a U.S. PBF experimental reactor, and research was done on the process of fuel damage and the discharge of FP. It was learned that the damage of fuel progressed slowly and that the rate of discharge of FP was smaller than it had been in past analyses. Also, predicting the complicated dynamics of the time of fuel damage became possible by analytic codes.

Furthermore, experiments to clarify conditions under which to cool a damaged core with a coolant are being conducted by the Japan Atomic Energy Research Institite, using a damaged core cooling capacity testing device shown in Figure 9 and NSRR, and matters including the water pour conditions to make core cooling possible even at a level beyond design basis accidents are becoming clarified.
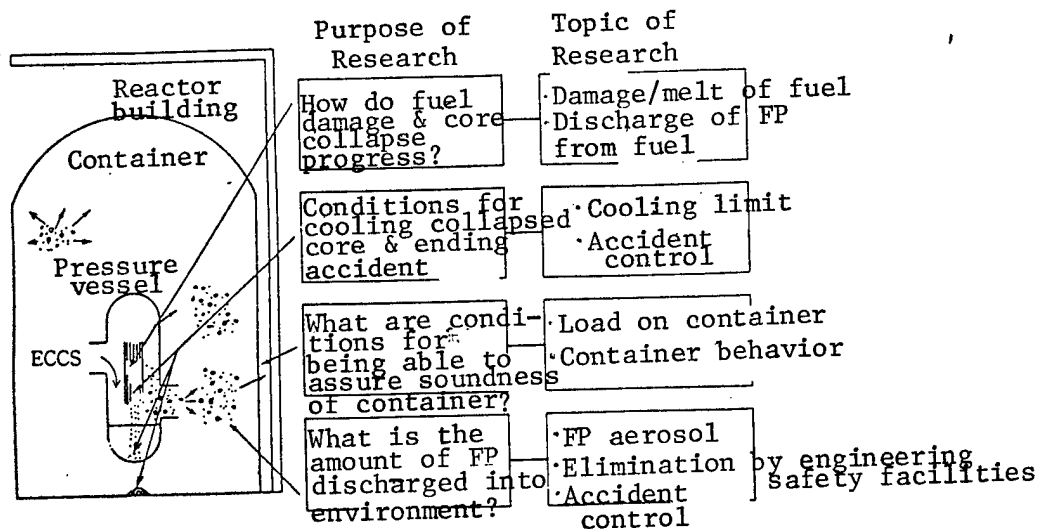
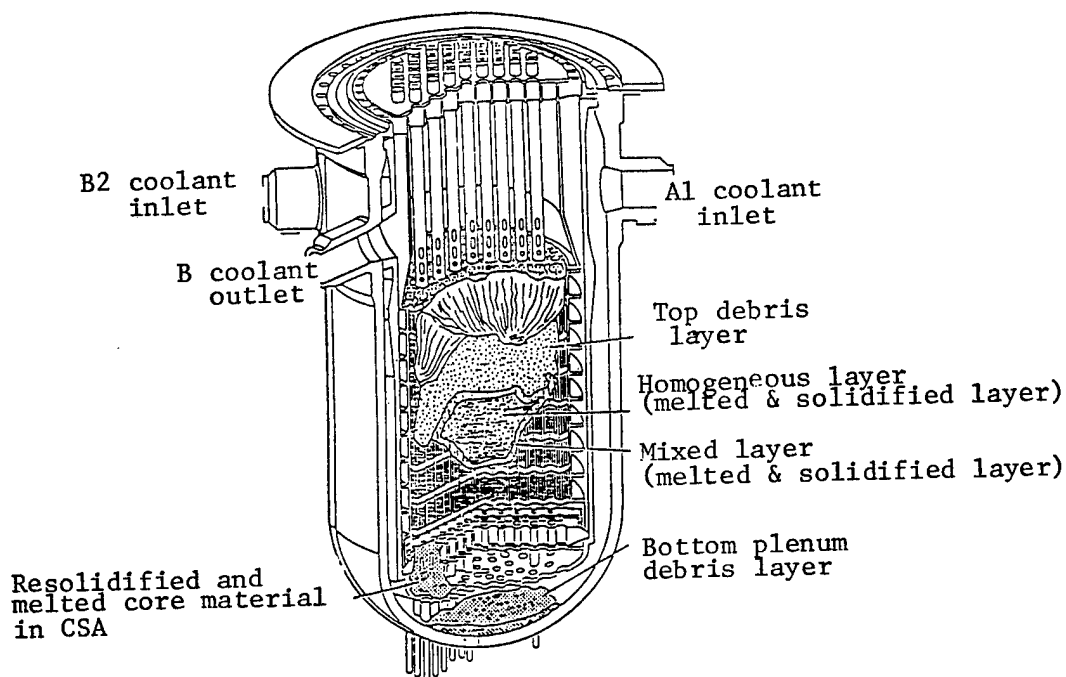Figure 7. Subjects of Research in Severe Accidents

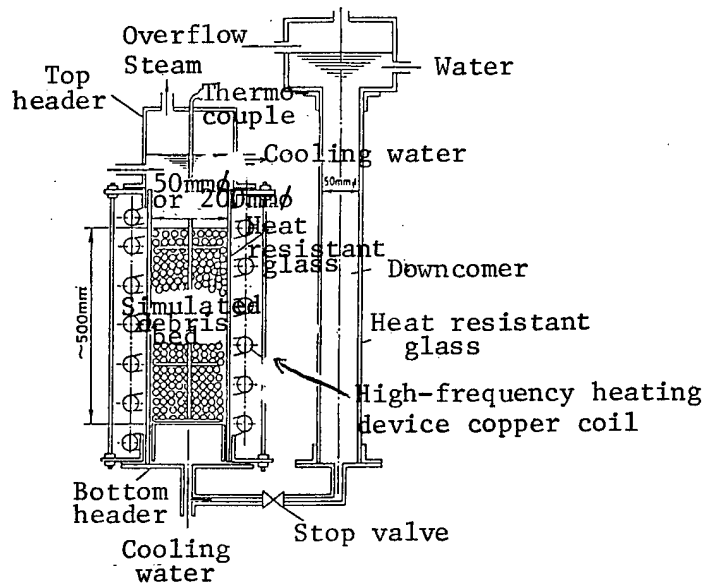Figure 8. Final State of TMI-2 Reactor

Figure 9. Damaged Core Cooling Capacity Testing Device

The Japan Atomic Energy Research Institute makes source term assessment by way of PSA (probabilistic safety assessment) in order to assess the amount of FP discharged into the environment in a severe accident and quantifies the risk of the reactor. It has developed an analytic code for this purpose and carries out assessments for atomic power plants. As a result, problems in assessing have been enumerated and items requiring research have been pointed out.

Above all, the importance of the role of the container, which is the final protective barrier to prevent the discharge of FP into the environment, was mentioned and it was deemed necessary to fully grasp phenomena relative to load exerted against the container as well as the behaviors of the container. Thereupon, the Japan Atomic Energy Research Institute decided to start container soundness assessment from fiscal 1987 and manufacture a test device for container behaviors from fiscal 1988. It is known from past results that the container can maintain its structural strength against a load several times higher than the level for design basis accidents.

The results of research on safety against severe accidents will be used along with the results of PSA to further the safety of atomic power plants.

133

Nuclear Plant Workers Show Chromosome Damage

OW3001041189 Tokyo KYODO in English 0305 GMT 30 Jan 89

/Text/ Fukushima, Jan 30 KYODO -- Male workers at nuclear power plants
have twice as many abnormal chromosomes as their counterparts in the
general population, according to a recent survey by a prefectural govern-
ment-run research institute.

During a five-year period beginning in 1984, the survey analyzed 93,505
lymph cell samples collected from 115 adult male plant workers at the
Tokyo Electric Power Co.'s No 1 and No 2 plants in Okuma, Fukushima and
found that 0.22 percent of the cells contained malformed chromosomes.

The survey compared the samples with those taken from 170 other male
workers of the same age group who were not connected with the plants, and
found that only 0.12 percent of the latter samples showed chromosome
defects.

The authors of the survey said that their studies did not show that the
defects could be passed on genetically.

The results were reported to the Fukushima Prefectural Government upon
completion at the end of last year but the prefectural authorities did
not release the report, saying, "the contents are not such as to be
viewed as problematic."

New Developments in Applied Superconductivity

Josephson Digital Circuits*: Fujitsu

43060705   Osaka OSAKA UNIVERSITY INTERNATIONAL SYMPOSIUM in English 17-19 Oct 88
p 50

[Text]   Performance of integrated circuits with Josephson junctions have been
dramatically improved since niobium junctions were available. We are
challenging to make ultra-fast Josephson computers. At present, we can operate
a few thousands gate level LSIs. Compared with conventional semiconductor
LSIs, the performances of the Josephson LSIs are outstanding in operating speed
and power consumption. This is owing to the development of a reproducible and
controllable Nb/AlOx/Nb junction fabrication process. This paper describes
fabrication technology of niobium based integrated circuits and applications of
the process to high speed digital circuits. Main topics are a high-uniformity
junction process, three-dimensional integration technology, a 4-bit micro-
processor, a 4K-bit memory and a single-chip SQUID magnetometer.

Lastly, the author will make a comment on the expected performance of the
digital circuits with high-T_c materials.

*   The present research effort is part of the National Research and Development
    Program on "Scientific Computing system," conducted under a program set by
    the Agency of Industrial Science and Technology, Ministry of International
    Trade and Industry.

Experimental Ship With Superconducting Electromagnetic Thruster:
  Japan Foundation for Shipbuilding Advancement

43060705   Osaka OSAKA UNIVERSITY INTERNATIONAL SYMPOSIUM in English 17-19 Oct 88
p 61

[Article by Yohei Sasakawa, Kensaku Imaichi, Eiichi Tada, and Setsuo Takezawa]

[Text] A superconducting electromagnetic thruster (EMT) ship is the most
attracting particular interest in the field of large superconducting technology
and shipbuilding world. This technology creates the possibility of making

lightweight superconducting magnets capable of generating a strong magnetic flux density enough to go ahead ships commercially. The Japan Foundation for Shipbuilding Advancement (JAFSA) in Japan intends to operate sailing tests of the world's first prototype EMT experimental ship in 1990. The ship powered by EMT has the following characteristics:

Displacement	150 tonnes,
Engine Unit	100 tonnes,
Hull	50 tonnes,
Propulsive Thrust	8,000 Newtons,
Engine Type	Inner Magnetic EMT,
Propulsive Unit	2 units
Speed	8 knots,
Crew Complement	10 persons.

The superconducting magnet of this ship is made up six dipoles, shown Fig. 1, that are arranged as a round table. Each dipole is 3.2 meters in length, double layer winding with Nb-Ti and PCS mode. This magnet is 5 meters in length, 1.8 meters in diameter, 15 tonnes in weight and the heat loss is about 10 watts at 4 K. Holding the cryostat at liquid helium temperature, we are developing a small on board helium refrigerator with two micro turbo expanders with 6 millimeters in diameter and 600000 rpm.
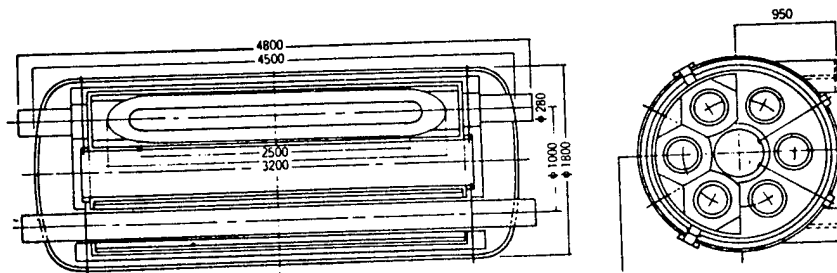
Development of Electrodes for Use in Superconducting Electromagnetic
Propulsion Ship: Osaka Electro-Communication University

[Article by Masa-aki Muroya (Osaka Electro-Communication University); Masao Hiroi (Kobe University of Marcantile Marine); Soichi Ogawa (Osaka Prefectural Industrial Research Institute); Eiichi Tada (Osaka University) and Yasuyuki Takemoto (Kobe University of Marcantile Marine)]

[Text] The superconducting magnet has been used for many fields. The superconducting electromagnetic thrust ship (EMT-ship) is one of its applications. The thrust of the ship is resulted from the interaction

between magnetic field generated by the fixed superconducting magnet on the ship and current which is passed into seawater. The electrode and it the system, which is apart of the thrust devices, are play an important role for the generation of thrust. [as printed]

This paper describes an electrode(anode) for use in the superconducting EMT-ship. The starting points for the development of electrodes were taking in to account: insoluble in seawater and chemically stabilize; invariable of the circulation of current; homogenity of the potential at the electrode/ solution interface; highly catalytic reactivity for oxygen evolution at the anode; surpassable in mechanical strength. In order to realize the creation of these conditions, the electrodes were established by select from among the groups such as electrodes using industrial electrolysis, the surface modified electrodes of these industrial electrodes and the new developed electrodes which were trial manufacture in our laboratory.

The tests of anodic property on developed electrodes in this work were carried out as a function of (1) the electrolysis of 3.5 percent sodium chloride solution with or without flow under ordinary temperature and pressure, (2) the current density at 4000 A/m^2 and below, (3) the electrolysis with or without a magnetic field of 5 tesla and (4) the evaluations of the relative oxygen/ chlorine evolution efficiencies. The platinum-coated titanium cathode is used in this testing electrolysis.

It was found that an anodes selected and prepared in this work will evolve oxygen from the sodium chloride solution at expected efficiency.

Development Considerations on Multifilamentary Superconductors for Super-
conducting Generator: Electrotechnical Lab

43060705 Osaka OSAKA UNIVERSITY INTERNATIONAL SYMPOSIUM in English
17-19 Oct 88 p 64

[Article by Shiro Kurihara (Agency of Industrial Science and Technology, MITI); Yoichi Kimura (Electrotechnical Laboratory, AIST); Shinichiro Meguro, Kiyotaka Uyeda, Takashi Saitoh, Kenichi Takahashi and Hiroshi Kubokawa (Engineering Research Association for Superconductive Generation Equipment and Materials (Super-GM)]

[Text] Feasibility studies on the equipment and materials for superconducting generator were conducted in 1985 and 1986 within the framework of the moon light project sponsored by the Agency of Industrial Science and Technology, Ministry of International Trade and Industry. The Engineering Research Association for Superconductive Generation Equipment and Materials was established on October 1, 1987. In its first year, 1987, the Association conducted researches to identify the research and development tasks over the 8-year national project to be started in 1988 and to establish the research and development plan.

In this paper, the technical points of view in order to develop the most suitable multifilamentary superconductor for the field windings in accordance with the design of superconducting generator are described. The optimum design of reliable superconductor should include the considerations on the items shown below.

Current density
Alternating current loss
Mechanical properties
Thermal and mechanical stability
Procedures to evaluate the properties described above

Developmental items were extracted through the conductor designs which correspond to low response excitation machine, quick response excitation machine and advanced Nb_3Sn machine.

As the results of the study, the necessity of the developmental work was recognized even for MbTi superconductor to realize the practical and reliable machine. And the advantage of Nb_3Sn superconductor when used in the generator was identified for its higher critical current density and higher critical temperature.

Design of Superconducting Power Cable Using High Tc Superconductors: Furukawa Electric

43060705 Osaka OSAKA UNIVERSITY INTERNATIONAL SYMPOSIUM in English 17-19 Oct 88 p 102

[Article by Yoshio Furuto and Naotaka Ichiyanagi, Furukawa Electric]

[Text] When high-Tc superconductors are used as cable material, the cost of power transmission is estimated to be 10 to 30 percent lower than with conventional superconducting cables. High Tc superconducting cables may therefore find commercial use over 66 kV class medium- and large-capacity transmission systems.

The large AC loss obtained by calculation and the degradation of critical current by tensile stress are the important problems when high Tc super-conducting cable are to be put to practical use.

These properties are dependent on the cable structure and critical current of superconducting material. According to the feasibility study, it was found that 5,000 A class superconducting cables will become a reality if a superconducting material fulfills the condition $Jc \gtrsim 10^4$ A/cm^2 and allows of strain about 0.1 percent. Superconducting cables of 10,000 A class will be required to fulfill the condition $Jc \gtrsim 10^5$ A/cm^2.

Preparation of High Tc(100K) Superconducting Bi(Pb)-Sr-Ca-Cu-O Film: Toray Research Center

[Article by Hitoshi Nobumasa, Kazuharu Shimizu, Takahisa Arima, Yukishige Kitano, Toroy Research Center, and Tomoji Kawaii, Osaka University]

[Text]   ABSTRACT

Films of a 100K superconducting Bi(Pb)-Sr-Ca-Cu-O were formed on a MgO (100) single crystal by a spray pyrolysis method. An aqueous solution of Bi, Pb, Sr, Ca and Cu nitrates was prepared to give the atomic ratio of Bi, Pb, Sr, Ca, and Cu to be 0.8:0.2:0.8:1.7:1.6. The aqueous solution was sprayed over a MgO substrate which was kept at 400°C on a hot plate. Fifteen hours heating of the as-sprayed films at 845°C in air was enough to give superconducting films with a Tc_{zero} higher than 100K. An X-ray diffraction pattern (Fig.1) showed that this film mainly consisted of the high-Tc phase with the orientation of the c-axis perpendicular to the surface. Furthermore a microstructure having triple Cu-O layers without an intergrowth was directly proved by a high resolution TEM.
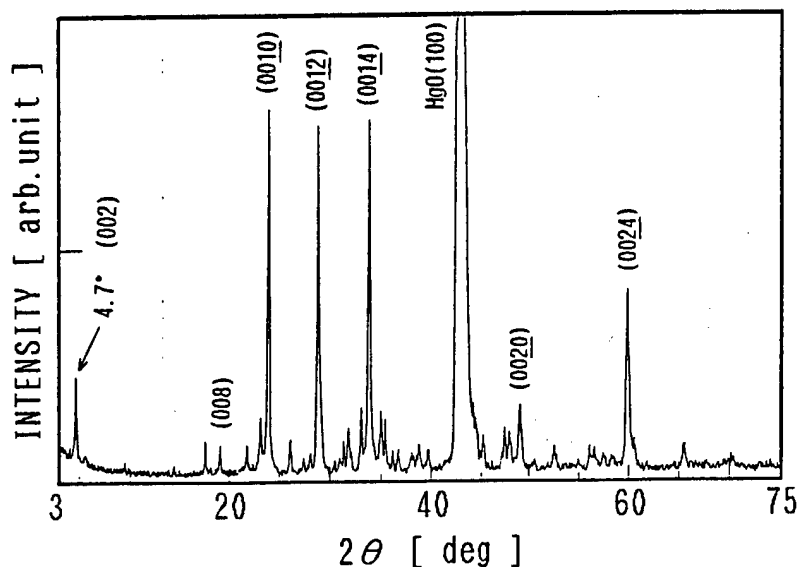
Fig. 1

END